

# Flows of Nanofluids inside Cavities: Finite Element Method



by

**Naeem Ullah**

Department of Mathematics

Quaid-i-Azam University

Islamabad, Pakistan.

2022

# Flows of Nanofluids inside Cavities: Finite Element Method



by

**Naeem Ullah**

Supervised by

**Prof. Dr. Sohail Nadeem**

Department of Mathematics

Quaid-i-Azam University

Islamabad, Pakistan.

2022

# Flows of Nanofluids inside Cavities: Finite Element Method



by

**Naeem Ullah**

Supervised by

**Prof. Dr. Sohail Nadeem**

A thesis presented for the degree of

**Doctor of Philosophy**

Department of Mathematics

Quaid-i-Azam University

Islamabad, Pakistan.

2022

# Author's Declaration

With these words, I proclaim that this dissertation with title “**Flows of Nanofluids inside Cavities: Finite Element Method.**” is the research effort by me at Department of Mathematics, Quaid-i-Azam University, Islamabad, Pakistan. I finalize this report for the degree of Doctor of Philosophy in Mathematics under the kind supervision of **Prof. Dr. Sohail Nadeem**. The detail put forward is based on my own research work, and is not issued anywhere in the book or an article. The present thesis has not been complied anywhere for any other qualification or degree neither in this nor any other university.

Signature: \_\_\_\_\_

Name: **Naeem Ullah**

# Plagiarism Undertaking

I solemnly declare that research work presented in the thesis titled “**Flows of Nanofluids inside Cavities: Finite Element Method.**” is solely my research work with no significant contribution from any other person. Small contribution/help wherever taken has been duly acknowledged and that complete thesis has been written by me. I understand the zero tolerance policy of the HEC and Quaid-i-Azam University towards plagiarism. Therefore, I as an Author of the above titled thesis declare that no portion of my thesis has been plagiarized and any material used as reference is properly referred/cited. I undertake that if I am found guilty of any formal plagiarism in the above titled thesis even afterward of PhD degree, the University reserves the rights to withdraw/revoke my PhD degree and that HEC and the University has the right to publish my name on the HEC/University Website on which names of students are placed who submitted plagiarized thesis.

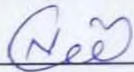
Student/Author Signature: \_\_\_\_\_

Name: **Naeem Ullah**

## Certificate of Approval

This is to certify that the research work presented in this thesis entitled **Flows of Nanofluids inside Cavities: Finite Element Method** was conducted by **Mr. Naeem Ullah** under the kind supervision of **Prof. Dr. Sohail Nadeem**. No part of this thesis has been submitted anywhere else for any other degree. This thesis is submitted to the Department of Mathematics, Quaid-i-Azam University, Islamabad in partial fulfillment of the requirements for the degree of Doctor of Philosophy in field of Mathematics from Department of Mathematics, Quaid-i-Azam University Islamabad, Pakistan.

Student Name: **Naeem Ullah**

Signature: 


External committee:

a) **External Examiner 1:**

Name: **Dr. Rahmat Ellahi**

Designation: Professor

Office Address: Department of Mathematics & Statistics, International Islamic University, Islamabad.

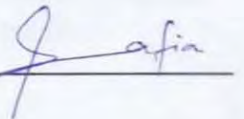
Signature: 

b) **External Examiner 2:**

Name: **Dr. Safia Akram**

Designation: Professor

Office Address: Department of Mathematics, Military College of Signals, NUST, Rawalpindi.

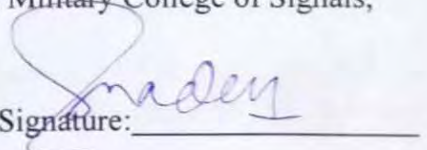
Signature: 

c) **Internal Examiner**

Name: **Dr. Sohail Nadeem**

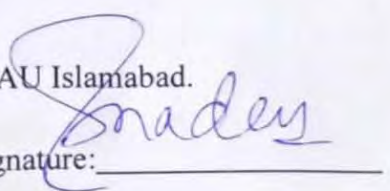
Designation: Professor

Office Address: Department of Mathematics, QAU Islamabad.

Signature: 

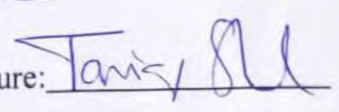
**Supervisor Name:**

**Prof. Dr. Sohail Nadeem**

Signature: 

**Name of Dean/ HOD**

**Prof. Dr. Tariq Shah**

Signature: 

# Flows of Nanofluids inside Cavities: Finite Element Method

By

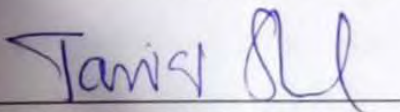
**Naeem Ullah**

CERTIFICATE

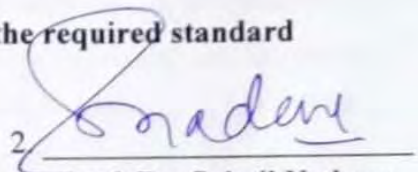
A THESIS SUBMITTED IN THE PARTIAL FULFILLMENT OF THE REQUIREMENTS FOR THE DEGREE OF THE

**DOCTOR OF PHILOSOPHY IN MATHEMATICS**

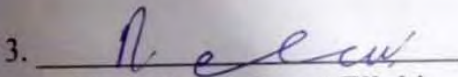
We accept this thesis as conforming to the required standard

1. 

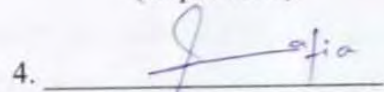
**Prof. Dr. Tariq Shah**  
(Chairman)

2. 

**Prof. Dr. Sohail Nadeem**  
(Supervisor)

3. 

**Prof. Dr. Rahmat Ellahi**  
(External Examiner)

4. 

**Prof. Dr. Safia Akram**  
(External Examiner)

Department of Mathematics & Statistics,  
International Islamic University, Islamabad.

Department of Mathematics, Military  
College of Signals, NUST, Rawalpindi.

**Department of Mathematics**  
**Quaid-I-Azam University**  
**Islamabad, Pakistan**  
**2022**

# Acknowledgment

All praise for “Almighty Allah”, the most Beneficent, the most merciful, who strengthen me to accomplish this thesis.

Words cannot express my gratitude to my professor **Prof. Dr. Sohail Nadeem** for his invaluable supervision, support and tutelage during the course of my PhD degree. His knowledge, accessibility and availability have been a critical impetus in driving this research. This endeavor would not have been possible without his incredible support and encouragement. I am ever indebted and obliged to him.

I would like to convey my heartiest gratitude to my respectable seniors and co-advisors **Dr. Zahid Ahmed, Dr. Noor Muhammad, Dr. Arif Ullah Khan** for their treasured support which was really influential in shaping my experiment methods, critiquing my results given me confidence to complete this task. I have been lucky enough to have good friends in my academic and social life and cannot forget their role in my education and university life. It is a matter of great delight and pleasure for me to thank my truly wonderful friends and colleagues **Dr. Muhammad Ijaz Khan, Dr. Khalil Ur Rehman, Dr. Faisal Shah, Dr. Zahid Nisar, Dr. Shafiq Ahmad, Dr. Nadeem Abbas, Dr. Muhammad Naveed khan, Salman Akhtar, Naseer Muhammad khan, Muhammad Riaz Khan, Muhammad Hasnain, Jameel Abbas, Mirza Naveed, Aqeela Qaiser** for a cherished time spent together in the lab, and in social settings. I am extremely thankful to **Shahid Khan, Arslan Khan, Aizaz Ali, Kalim Ullah** to be always around whenever I need them. I always feel fortunate to be blessed with such friends. I'd also want to thank **Inayat Ullah** and **Raja Saleem** who assisted me and have always been at my side. Additionally, I'd like to thank my fellow graduate students **Amna Yasin, Ayesha Bibi, Bisma Akram, Aqsa Rehaman, Warda Waheed** for their contribution in my research journey.



I would be remiss in not mentioning my family, especially my loving and caring mother **Balbala Begum**, my toughest from outside but coolest from inside father **Sakhi Sultan**, my brothers **Kaleem Ullah, Waseem Ullah, Sami Ullah, Amin Ullah**, my sisters **Shehnaz Sultan, Safia Sultan, Ayesha Sultan** for their endless love, prayers, encouragement, cordial cooperation and continuous support. They selflessly encouraged me to explore new directions in my life and seek my own destiny. I want to convey my deepest thanks and compliment to my uncle **Taj Gul Safi** for motivating me who always interested in my personal development. I know that I can always count on you. Than you for all the encouragement and lighting my mind when it comes to understanding some realities in life. Thank you.

Naeem Ullah

June 19, 2022

# Contents

<b>1</b>	<b>Introduction</b>	<b>1</b>
<b>2</b>	<b>Mathematical investigation and concepts</b>	<b>10</b>
2.1	Physical description and governing equations . . . . .	10
2.2	Thermophysical properties of nanofluid and dimensionless numbers . . . . .	13
2.2.1	Electrical and thermal conductivity . . . . .	13
2.2.2	Viscosity of nanofluids . . . . .	15
2.2.3	Specific heat and density of nanofluid . . . . .	15
2.2.4	Prandtl number . . . . .	15
2.2.5	Grashof number . . . . .	16
2.2.6	Rayleigh number . . . . .	16
2.2.7	Reynolds number . . . . .	17
2.2.8	Richardson number . . . . .	17
2.2.9	Nusselt number . . . . .	18
2.3	Numerical solution with finite element method . . . . .	20
2.3.1	General theory and introduction . . . . .	20
2.3.2	Finite element solution procedure . . . . .	21
2.4	Finite element method implementation . . . . .	23
2.5	Mesh independence and results validation . . . . .	27
2.6	Concluding remarks . . . . .	32

<b>3</b>	<b>Finite Element simulations for natural convective flow of nanofluid in a rectangular cavity having corrugated heated rods</b>	<b>33</b>
3.1	Introduction . . . . .	33
3.2	Mathematical formulation . . . . .	34
3.3	Results and discussion . . . . .	39
3.4	Concluding remarks . . . . .	47
<b>4</b>	<b>Finite element analysis of convective nanofluid equipped in enclosure having both inlet and outlet zones</b>	<b>49</b>
4.1	Introduction . . . . .	49
4.2	Geometrical description and basic equations . . . . .	50
4.3	Results and discussion . . . . .	55
4.4	Concluding remarks . . . . .	69
<b>5</b>	<b>Simulations of micropolar nanofluid-equipped natural convective driven flow in a cavity</b>	<b>70</b>
5.1	Introduction . . . . .	70
5.2	Physical model and basic equations . . . . .	71
5.3	Results and discussion . . . . .	76
5.4	Concluding remarks . . . . .	87
<b>6</b>	<b>Simulation for nanofluid convective flow inside a partially adiabatic enclosure influenced by a sinusoidal oriented heated element</b>	<b>88</b>
6.1	Introduction . . . . .	88
6.2	Model description and governing equations . . . . .	89
6.3	Results and discussion . . . . .	94
6.4	Concluding remarks . . . . .	108
<b>7</b>	<b>Forced convection of rotating cylinder in nanofluid filled vented</b>	

<b>porous parallelogram enclosure</b>	<b>110</b>
7.1 Introduction . . . . .	110
7.2 Physical model and governing equations . . . . .	111
7.3 Results and discussion . . . . .	117
7.4 Concluding remarks . . . . .	132
<b>Bibliography</b> . . . . .	<b>133</b>

# List of Figures

2.1	Physical sketch of the flow problem. . . . .	11
2.2	Discretization of the flow domain . . . . .	22
2.3	Comparison of present work (a) isotherms (c) streamlines with previous experimental (b) and numerical (d) results by Calcagni et al. [68] against $Ra = 1.86 \times 10^5$ , $\phi = 0$ . . . . .	29
2.4	Comparison of present work velocity (a) with reference [70] and Nusselt number (b) with [69]. . . . .	30
2.5	Streamlines comparison with Shahi et al. [71] at $Ri = 0.1$ (a),(c) and $Ri = 10$ (b), (d). . . . .	31
3.1	Geometry of the physical problem . . . . .	35
3.2	Mesh generation at different portion in physical domain. . . . .	35
3.3	Impact of $Ra$ on Nusselt number (a) along the outer heated length (b) along the inner corrugated heated rods and (c) temperature (d) Velocity profile along horizontal mean position. . . . .	42
3.4	Impact of $\phi$ on Nusselt number (a) along the outer heated length (b) along the inner corrugated heated rods and (c) temperature (d) Velocity profile along horizontal mean position. . . . .	43
3.5	Variations in Nusselt number for various $\phi$ at (a) $n_1 = 0$ (b) $n_1 = 10$ (c) $n_1 = 20$ (d) $n_1 = 30$ . . . . .	44

3.6	Isotherms for different $Ra = 10^4$ (left), $Ra = 10^6$ (right) and at various amplitude $A_m = 0.05$ ((a), (b)), $A_m = 0.1$ ((c), (d)) and $A_m = 0.2$ ((e), (f)). . . . .	46
3.7	Streamlines at various amplitude $A_m = 0.05$ ((a), (b)), $A_m = 0.1$ ((c), (d)) and $A_m = 0.2$ ((e), (f)) for different $Ra = 10^4$ (left), $Ra = 10^6$ (right). . . . .	47
4.1	Schematic sketch of physical model . . . . .	51
4.2	Mesh distribution of the computational domain. . . . .	52
4.3	Isotherms for various values of $\phi$ and $Gr$ . from top to bottom $\phi = 0.01$ ((a), (b)), $\phi = 0.02$ ((c), (d)), $\phi = 0.04$ ((e), (f)) and $Gr = 10^3$ (left), $Gr = 10^4$ (right). . . . .	60
4.4	Impact of $\phi$ on Nusselt number in (a) and temperature and velocity in (b), (c) along heated length and horizontal mean position . . . . .	61
4.5	Streamlines and temperature contour for various values of $Gr$ . $Gr = 10^3$ ((a), (b)), $Gr = 10^4$ ((c), (d)) and $Gr = 10^5$ ((e), (f)). . . . .	62
4.6	Impact of $Gr$ on Nusselt number in (a), temperature and velocity in (b), (c) along heated length and horizontal mean position . . . . .	63
4.7	Streamlines and isotherms against various Darcy number. $Da = 10^{-2}$ ((a), (b)), $Da = 10^{-3}$ ((c), (d)) and $Da = 10^{-4}$ ((e), (f)). . . . .	65
4.8	Influence of $Da$ on Nusselt number in (a), velocity and temperature in (b), (c) along heated length and horizontal mean position . . . . .	66
4.9	Isotherms at distinct heated segments $Lt$ . $Lt = 0.25$ (a), $Lt = 0.50$ (b), $Lt = 0.75$ (c), and $Lt = 1.0$ (d). . . . .	67
4.10	Variations in Nusselt number (a) and temperature (b) at various heated portion . . . . .	67
4.11	Streamline and Isotherms at various $Re$ . ((a), (b)) $Re = 1$ $Ri = 10^3$ , ((c), (d)) $Re = 10$ $Ri = 10$ and ((e), (f)) $Re = 100$ $Ri = 0.1$ . . . . .	69

5.1	Physical schematic sketch and mesh distribution of the computational domain. . . . .	73
5.2	Impact of various $Ra$ on: a) Horizontal velocity component, b) Temperature, c) Angular momentum, d) Concentration. . . . .	79
5.3	Variations in streamlines and microinertia vector at $Pr = 2.0, Nr = 0.01, Le = 100, R = 0.5, Nt = 0.5, Nb = 0.5, Lh = 0.4$ : (a, b) $Ra = 100$ , (c, d) $Ra = 500$ , (e, f) $Ra = 1000$ . . . . .	81
5.4	Impact of $R$ on: a) velocity b) microrotation vector, c) concentration, d) temperature. . . . .	82
5.5	Variations in streamlines and microinertia vector at $Pr = 2.0, Nr = 0.01, Le = 100, Ra = 1000, Nt = 0.5, Nb = 0.5, Lh = 0.4$ : (a, b) $R = 1$ , (c, d) $R = 2.0$ . . . . .	83
5.6	Impact of $Lh$ on thermal, concentration and flow profiles. . . . .	84
5.7	Isotherms against various $Lh$ . . . . .	85
5.8	Impact of $Le$ on flow field and thermal distribution. . . . .	86
5.9	Variations in average Nusselt number against (a) $Ra$ and (b) $Lh$ . . .	86
6.1	Physical configuration and (b) Mesh distribution of domain. . . . .	90
6.2	Impact $\phi$ on (a),(b) Nusselt numbers (c) temperature and (d) velocity along the defined paths. . . . .	99
6.3	Variations in Isotherms (left) and Streamlines (right) at various $\phi$ . . .	100
6.4	Influence of element frequency $n$ on (a, b) Nusselt numbers, (c) temperature and (d) velocity at shown paths. . . . .	101
6.5	Streamlines (left) and Isotherms (right) at different heated element frequency $n$ . . . . .	102
6.6	Hartman number impact on (a), (b) heat transfer rate, (c) temperature and (d) $y$ -velocity at indicated paths. . . . .	103

6.7	Streamlines (a-e) and Isotherms (b-f) variations with respect to Hartman number $Ha$ . . . . .	104
6.8	Variation in Streamlines (a-g) and Isotherms (b-h) at different inclination angle $\alpha$ . . . . .	106
6.9	Impact of Raleigh number on (a, b) heat transfer rate, (c) temperature and (d) $y$ -velcoity at indicated paths. . . . .	107
6.10	Influence of $Ra$ on Streamlines (a-e) and Isotherms (b-f). . . . .	108
7.1	Physical model and (b) Mesh distribution of domain. . . . .	112
7.2	Influence of $Ri$ on V, T and $Nu_{av}$ in ((a), (b)) and (c) along horizontal mean position and heated portion. . . . .	123
7.3	Streamlines (left) and Isotherms (right) at various Richardson number $Ri$ . . . . .	124
7.4	Influence of $Da$ on V and T in ((a), (b)) along horizontal mean position and $Nu_{av}$ and $Cf_{av}$ in ((c), (d)) against heated portion. . . . .	125
7.5	Streamlines (left) and Isotherms (right) at various Darcy number $Da$	126
7.6	Influence of $\phi$ on V, T and $Nu_{av}$ in ((a), (b)) and (c) along horizontal mean position and heated portion. . . . .	127
7.7	Streamlines (left) and Isotherms (right) at various volume fractions $\phi$	128
7.8	Influence of $\Omega$ on V, T and $Cf_{av}$ in anticlockwise ((a), (b), (e), (f)) and clockwise directions ((c), (d)). . . . .	130
7.9	Streamlines (left) and isotherms (right) at different rotation speeds and directions $\Omega$ . . . . .	131



# List of Tables

2.1	Thermophysical properties water-based <i>CuO</i> nanoparticles. . . . .	19
2.2	Coefficient values of nanofluid. . . . .	19
2.3	Grid independence test, values of Nusselt number at different mesh size.	28
2.4	Comparison of Nusselt number against <i>Ri</i> with Rahman et al. [72] . .	32

# Chapter 1

## Introduction

Flows confined in cavities and enclosures are induced by buoyancy forces or both buoyancy and solid boundary movement. The two primary mode of buoyancy generated internal flows are natural convection and mixed convection. In such flows three main factors that control natural convection are the fluid volumetric expansion, the body forces (gravitational, electro-magnetic, centrifugal forces) and density differences (due to concentration and thermal effects). Natural convective flows inside different cavities and enclosure finds application in engineering science and technology. This subject got considerable attention due to its importance in various areas of geophysics, meteorology, geophysics, material processing, as a heat exchangers in nuclear reactor system, cooling of electronic equipment, solar energy system, fire control, in chemical processing apparatus, energy storage and conservation, thermal management in food storage stores, and many other fields of fluid and thermal science. A comprehensive review and applications of natural convection in different enclosures were initiated by Ostrach [1–6]. During the past decades literature on this topic includes the finite element solution of natural convection phenomenon in a cavity invokes by heated side wall, has been presented by Ismail and Scalon [7]. The different variations in flow and thermal profile is reported influenced of various considered geometrical shapes.

Sezai and Mohmad [8] investigated the heat transfer characteristics in an enclosure induced by natural convection from heat source at bottom wall. In another study Haghshenas [9] examined natural convective flow and thermal properties in a square cavity having one side open, they found that the heat transfer is greatly influenced by Rayleigh number. Mixed convection flows within cavities and enclosures have especially piqued the interest of many researchers because flow situation in enclosures and cavities have amazing computational and physical features which appear in many scientific and technological applications. Louaraychi et. al. [10] examined the combine free and force convection generated by horizontal boundary movement and heat transfer correlation in a rectangular cavity. Theoretical studies on force flow behavior due to boundary motion and and free convection caused by mounted heated triangular blocks equipped-in an enclosure have been explored by Gangawane et. al. [11]. Salimipour [12] conducted numerical investigations of flow profile and heat transport characteristics owing to horizontal cylinder inducing mixed convective transportation. Gupta and Nayak [13] examined the convective (free and force) flow movement in a vented parallelogram-shaped enclosure, they observed a stronger cold regime established because of force inflow through contaminant source. Abu-Hamdeh et al. [14] analyzed a free convection due to a heated source at bottom and forced convection stems form wall movement of an enclosure. In another study Muhammad et al. [15] examined the mixed convection in ethylene glycol based nanofluid inside an enclosure having a heater in center line. Some other investigations exploring convection phenomenon in various enclosures are considered in [16–20]

Heat transport ability in convection can be triggered by adding of nanoparticles to base fluids. A nanoliquid is categorized as the colloidal suspension of the nanosized (<100nm) metallic particles dispersed into the conventional fluid (water, engine oil, kerosene oil, ethylene glycol, water-glycol, propylene-glycol etc). This insertion of nanosized particles into the orthodox fluid supplements the thermal characteristics

of the ordinary fluid amazingly. The characteristics of heat transmission of nanofluid depend upon thermo-physical behavior of the base fluid, volume fraction and thermo-physical nature of nanoparticles. Nanofluids owing to their amazing contributions in numerous areas i.e., power generation, microelectronics, space, cooling, nuclear reactors, electronic devices, energy production, and biomedical appliances are the fluids of the 21st century. In 1995 Choi [21] was the first who floated the novel idea of nanofluid. A comprehensive detail on the heat transmission phenomenon of nanofluid and key features that leads to an augmentation in heat transportation performance is presented by Buongiorno [22]. Following Choi and Buongiorno, researchers and scientist are encouraged to explore emerging applications of nanofluids in different aspects. To mention some important investigations, Chamkha and Selimefendigil [23] studied the entropy generation in the natural convective flow of nanofluid in an enclosure, they concluded that heat transfer and entropy generation enhances because of increase in Darcy number and solid fraction of nanoparticles. The numerical investigations of rotating flow and variable thermal properties of hybrid nanoparticles with two different types of base fluids (water and ethylene-glycol) is presented by Usman et al. [24]. Haq and Aman [25] studied flow and thermal behavior of nanofluid inside a trapezoidal cavity with heated object and found that nanoparticles volume fraction has a key role in thermal conductivity enhancement. Jiang and Zhou [26] inspected the nanofluid surface driven convection in a rectangular cavity, and found that nanoparticles fraction greatly influenced the surface tension driven convection and intensity of heat transfer characteristics. The thermal properties of nanofluid under the impact of radiation heat source inside a wavy shape cavity is scrutinized by Alkanhal et al. [27]. Their obtained results point out that the Nusselt number enhances due to radiative heat exchange.

Convective heat transport of fluid merged in porous media have been considered a field of great interest. Flow behavior in porous media possesses potential applica-

tions in industrial and chemical engineering process. Examples of such mechanism include thermo-insulation configuration, solar pond design, heating of rooms, drying of grains in storage installations, petroleum reservoirs, underground disposal of chemical and nuclear wastes, groundwater pollutant transport etc. In view of the stated applications over the past few years, the flow behavior in porous media occurs in various situation has been examined by several investigators. Previous such literature contains the forced convection of nanofluid in U-shaped enclosure containing porous medium is conducted by Selimefendigil and Öztop [28]. Nguyen et al. [29] analyzed the Ferro-nanofluid in a curved enclosure having porous medium, their analysis depict that convective transport augments by applying higher voltage in large porous regime. Pandit and Chattopadhyay [30] probed the natural convection subject to rectangular shaped cavity having different aspect ratios. The porous medium was entertained in this study along with unsteady effect. Mondal and Sibanda [31] investigated the natural convection with unsteady double diffusion direction subject to porous cavity. In this study they considered both non-uniform and uniform boundary conditions. Sheremet et al. [32] discussed the magnetized natural convection aspects of nanofluid towards wavy porous cavity. The entropy generation study for dual convection flow towards porous cavity along with channel domain equipped with nanofluid was reported by Hussain et al. [33]. Chen et al. [34] adopted finite volume method to examine free convective flow within porous wavy enclosure. Free convection of Nanofluid in a cavity filled with porous matrix is explored by Bourantas et al. [35], they exhibited the dependence of heated source length on flow fields. The influence of wavy walls on free convection in a porous enclosure is explored by Sompong and Witayangkurn [36]. Cheong et al. [37] applied finite difference method to examined the impact of the wall inclination on flow dynamics in trapezoidal cavity filled with permeable medium.

Magneto-fluids are important class of fluids and have numerous applications in

engineering and industrial aspects. The study of such fluids is known as magnetohydrodynamic which is characterized as the interaction of moving electrically conducting fluid with electromagnetic field. It was initiated by Hannes Alfvén and is considered as by coupling the Maxwell's electro-magnetic equations with the flow and heat dynamic equations. The presence of magnetic field generates Lorentz force. In natural convection fluid movement is caused by buoyancy force. When magnetic field is applied on fluid these two body forces (Lorentz force and buoyancy force) interact with each other and influence the flow fields and thermal distribution. Magnetic field suppresses convection due to reduction in velocities. Mahmoudi et al. [38] analyzed free convection in square enclosure. It was found that Lorentz forces applied in various directions effect the thermal profile and controls the flow of nanoparticles. Magnetic effect at different inclinations on free convective flow in trapezoidal cavity is presented by Miroshnichenko et al. [39]. They reported that heat flux is enhanced with nanoparticles addition and decrease with Hartmann number. The Magneto hydrodynamic natural convective flow in a wavy inclined enclosure containing Nano fluid is studied by Sheremet et al. [32] and it was observed that inclination of cavity and magnetic effects enhances the convective heat transfer rate. Magnetic field influence on free convection in prismatic cavity is indicated by Parvin and Akter [40]. Results depicted that heat transfer is altered by Hartman number. In a T-shaped enclosure the free convective flow is explored by Sahi et al. [41]. They concluded that stronger magnetic effect decline the average heat transfer rate and the convection transport switches toward conduction dominant regime. Haq et al. [42] investigated the free convective flow of MHD fluid in corrugated enclosure.

Micropolar fluid is a new class of non-Newtonian fluids, the model for such fluids is derived from microphorpnic theory. Eringen [43–45] initially suggested microfluidics theory in order to delineate the micro-motions of fluid particles that could not be described by the classical models. The beauty of this model is that it can charac-

terizes various complex rheological fluids like, animal blood, polymers, lubricants, suspension and paints etc. For detail analysis about this model one can assessed [46–49]. Due to its vast implementations in various industrial products, material processing, biomechanics, slurry technology low-concentration suspensions, turbulent shear flows, colloidal suspensions etc, numerous researcher have adopted micropolar fluid basic equations to narrate flow problem in various enclosure and cavities. likewise, in Saleem et al. [50] have numerically studied the two-dimensional natural convection micropolar fluid flow inside a rectangular cavity warmed with cold side-walls form below. Sheremet et al. [51] conducted the transient flow characteristics of micropolar fluid in triangular enclosure having one wavy side induced by free convection. Nazeer et al. [52] investigated the effect of moving wall on the mixed convection boundary layer flow in a triangular right-angle cavity equipped with a micropolar liquid. Abidi et al. [53] presented three-dimensional numerical evaluation of convective heat transfer and fluid motion in a cavity filled under a uniform magnetic field in the existence of micropolar liquid. They recorded that mass and heat transfer rates are rising and decreasing due to an increment in the amount of Rayleigh and Hartmann, respectively. The electrodynamic induced free convective flow field in a rectangular enclosure filled with micropolar fluid is considered by Samaei et al. [54]. Yan et al.[55] carried out buoyancy driven micropolar-fluid flow in an enclosure having elliptic shaped heat source. They report the important solutions subject to applied inclined magnetic effect and thermal radiation.

The present thesis includes seven chapters in which the introductory part is presented in first chapter, the second chapter is about the general mathematical formulation of flow situation involve in an enclosure and it's solution methodology is explained in details. While the other chapters in which free and forced convection flows are considered in various enclosures examined under different boundary and fluid constraints. These chapters are carried out in the following way

In **chapter 3** the natural convection in a partially heated rectangular cavity containing water-based copper oxide nanofluid ( $CuO$ -water) is the topic of our investigation. The flow field and heat transfer inside the cavity are influenced by two corrugated heated rods. For the thermophysical properties of nanofluid Koo and Kleinstreuer-Li (KKL) model is implemented in the governing equations. Numerical solution of the resulting system of equation is obtained utilizing Finite Element Method. A validation study with existing literature is also made and it was found that our obtained results are in excellent agreement existing literature. This investigation is published in the “**Journal of Thermal Analysis and Calorimetry**” **143:(2021);4169–4181**.

The study in **chapter 4** contains the mathematical and computational analysis of the forced and free convection in a square shape enclosure with inlet/outlet opening. The flow field is manifested with  $CuO$  nanoparticles along with the porous media assumption. The left boundary is uniformly heated while the right wall is taken cold. The force flow constraint is implemented on the openings ports and the remaining portions are kept adiabatic. To be more specific the mixed convection transportation in the regime persists because of thermal difference in-between the heated source and cold inflow of fluid. To report solution the finite element method has been adopted. The mesh independence test and validation of our results in comparison with previous published literature is also performed. Both the graphical and numerical compared results are in good agreement with existing study. The simulation in this chapter is published in the “**Journal of the Taiwan Institute of Chemical Engineers**” **113:(2020);428-441**.

**Chapter 5** focuses on the natural convective flow analysis of micropolar nanofluid fluid in a rectangular vertical container. A heated source is placed in the lower wall to generate the internal flow. In further assumptions the left/right wall are kept cool, while the upper and lower remaining portions are insulated. Free convection prevails



in the regime because of thermal difference in-between the lower warmer and upper colder region. Such physical setup owns mathematical framework in-terms of non-linear partial differential equations. The interesting features of the flow along with thermal transportation involve both translational and rotational movement of fluid particles. Performing the simulations towards flow controlling variables the outputs are put together in contour maps and line graphs. The exploration in this chapter is published in the “**International Journal of Numerical Methods for Heat and Fluid Flow**” **31(8):(2021);2640-2659**.

The topic in **chapter 6** is the research exploration for free convection in a squared shaped enclosure which contains a heated element placed at core region. The Copper Oxide nanoparticles are taken as solid part of water based nanofluid in the cavity. The flow configuration is subject to magnetic field applied in an inclined manner. Further, assumption includes the influence of left and right wall of cavity considered cooled, the lower boundary is heated partially, and the remaining boundaries are taken adiabatic. Finite element analysis offered the solutions for the obtained differential equation of the physical problem. Specifically, the flow dynamics and thermal transmission are the quantities of physical interest. The computational scheme presents the outcomes toward various emerging parameters in both line-graphs and isolines. The results in this chapter are submitted in “**International Journal for Numerical Methods in Fluids**”.

Mixed convection flow of nanofluid in porous parallelogram cavity having corrugated upper and lower walls is analyzed in **chapter 7**. The Forced convection in the enclosure is developed by external cold fluid inflow and rotating cylinder placed in the core of cavity. while heated corrugated lower wall maintain free convection in the regime. Moreover, upper corrugated wall is cold, while the remaining portions of the enclosure are taken to be insulated. This physical model is converted into partial differential equations and solution of these equations are attained through finite ele-

ment method. The outcomes are presented in terms of Nusselt number, line graphs and contour maps. An acceptable comparison of our simulation is also made for the reduced case with previous published article. The content of this chapter is submitted for publication in “**Physica Scripta**”.

# Chapter 2

## Mathematical investigation and concepts

This chapter focuses on the mathematical analysis and the solution technique adopted in this thesis. A Natural convection problem is considered in first section, it's mathematical translation in term of partial differential equations is derived. The dimensionless parameters involve in the formulation which signify the physical situation of the flow profiles are defined in the second section. Also, various model for thermophysical properties of nanofluid are presented. Then in the next section Finite Element Analysis is formulated for the solution purpose of the reduced governing equations. Followed by the comparison and code validation of our computed results with the existing numerical and experimental literature in the last part.

### 2.1 Physical description and governing equations

Here we have addressed the two dimensional steady flow and thermal distribution in an enclosure which is generated by free convection. A partially heated square cavity of length  $l$  filled with water based  $CuO$  nanofluid as illustrated in figure 2.1. The bottom

wall is taken thermally active with temperature  $T_h$ , vertical walls are assumed at lower temperature  $T_c$  such that  $T_h > T_c$ . While, the upper wall is maintained insulated. Physical properties of the fluid are supposed to be constant excluding the density variation that give rise to buoyancy forces, which is approximated by Boussinesq approximation.

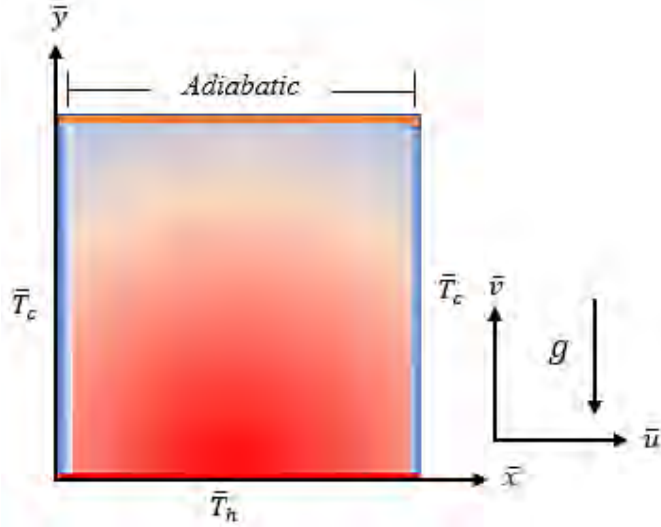


Figure 2.1: Physical sketch of the flow problem.

In view of the above assumptions the following conservation equations are acceptable to narrate the said physical configuration.

$$\frac{\partial \bar{u}}{\partial \bar{x}} + \frac{\partial \bar{v}}{\partial \bar{y}} = 0, \quad (2.1.1)$$

$$\bar{u} \frac{\partial \bar{u}}{\partial \bar{x}} + \bar{v} \frac{\partial \bar{u}}{\partial \bar{y}} = -\frac{1}{\rho_{nf}} \frac{\partial \bar{p}}{\partial \bar{x}} + \nu_{nf} \left( \frac{\partial^2 \bar{u}}{\partial \bar{x}^2} + \frac{\partial^2 \bar{u}}{\partial \bar{y}^2} \right), \quad (2.1.2)$$

$$\bar{u} \frac{\partial \bar{v}}{\partial \bar{x}} + \bar{v} \frac{\partial \bar{v}}{\partial \bar{y}} = -\frac{1}{\rho_{nf}} \frac{\partial \bar{p}}{\partial \bar{y}} + \nu_{nf} \left( \frac{\partial^2 \bar{v}}{\partial \bar{x}^2} + \frac{\partial^2 \bar{v}}{\partial \bar{y}^2} \right) + \frac{(\rho\beta)_{nf}}{\rho_{nf}} g (\bar{T} - T_c), \quad (2.1.3)$$

$$\bar{u} \frac{\partial \bar{T}}{\partial \bar{x}} + \bar{v} \frac{\partial \bar{T}}{\partial \bar{y}} = \frac{k_{nf}}{(\rho C_p)_{nf}} \left( \frac{\partial^2 \bar{T}}{\partial \bar{x}^2} + \frac{\partial^2 \bar{T}}{\partial \bar{y}^2} \right). \quad (2.1.4)$$

With the associated boundary conditions can be expressed as

temperature at lower and upper walls

$$\begin{cases} \bar{T} = T_h, & \text{at } 0.0 \leq \bar{x} \leq l, \bar{y}=0.0. \\ \frac{\partial \bar{T}}{\partial n} = 0, & \text{at } 0.0 \leq \bar{x} \leq l, \bar{y} = l. \end{cases} \quad (2.1.5)$$

Temperature on vertical walls

$$\bar{T} = T_C. \quad (2.1.6)$$

Velocity condition on all boundaries

$$\bar{u} = \bar{v} = 0. \quad (2.1.7)$$

Here  $(\bar{u}, \bar{v})$  are  $x$  and  $y$  components of velocity of the fluid,  $\bar{T}$  denotes the temperature.  $\rho_{nf}$  is the effective density of nanofluid.  $\nu_{nf}$  is the kinematic viscosities of nanofluid.  $((\rho\beta)_{nf}, (\rho C_p)_{nf})$  represents thermal expansion coefficient and heat capacitance of nanofluid, Whereas, the Thermal conductivity of nanofluid is given by  $k_{nf}$ , while,  $T_h$  and  $T_C$  stand for temperature at heated and cold boundaries.

Introducing the following dimensionless variables

$$\begin{aligned} X &= \frac{\bar{x}}{l}, & Y &= \frac{\bar{y}}{l}, & U &= \frac{\bar{u}l}{\alpha_f}, & V &= \frac{\bar{v}l}{\alpha_f}, & T &= \frac{\bar{T} - T_c}{T_h - T_C} \\ P &= \frac{\bar{P}l^2}{\rho_f \alpha_f^2}, & \text{Pr} &= \frac{\nu_f}{\alpha_f}, & Ra &= \frac{\beta_f(T_h - T_C)l^3}{\nu_f \alpha_f}. \end{aligned} \quad (2.1.8)$$

Here,  $\text{Pr}$  and  $Ra$  define the Prandtl and Rayleigh number. Implementing these variables the governing equations (2.1.1)-(2.1.4) and the boundary conditions (2.1.5) to (2.1.7) reduce to the following dimensionless equations

$$\frac{\partial U}{\partial X} + \frac{\partial V}{\partial Y} = 0, \quad (2.1.9)$$

$$U \frac{\partial U}{\partial X} + V \frac{\partial U}{\partial Y} = - \frac{\rho_f}{\rho_{nf}} \frac{\partial P}{\partial X} + \frac{\mu_{nf}}{\mu_f} \frac{\rho_f}{\rho_{nf}} \text{Pr} \left( \frac{\partial^2 U}{\partial X^2} + \frac{\partial^2 U}{\partial Y^2} \right), \quad (2.1.10)$$

$$\begin{aligned} U \frac{\partial V}{\partial X} + V \frac{\partial V}{\partial Y} &= - \frac{\rho_f}{\rho_{nf}} \frac{\partial P}{\partial Y} + \frac{\mu_{nf}}{\mu_f} \frac{\rho_f}{\rho_{nf}} \text{Pr} \left( \frac{\partial^2 V}{\partial X^2} + \frac{\partial^2 V}{\partial Y^2} \right) + \\ &\quad \frac{(\rho\beta)_{nf}}{(\rho\beta)_f} \frac{\rho_f}{\rho_{nf}} Ra \text{Pr} T, \end{aligned} \quad (2.1.11)$$

$$U \frac{\partial T}{\partial X} + V \frac{\partial T}{\partial Y} = \frac{\alpha_{nf}}{\alpha_f} \left( \frac{\partial^2 T}{\partial X^2} + \frac{\partial^2 T}{\partial Y^2} \right). \quad (2.1.12)$$

The boundary conditions reduces to the following dimensionless form

$$0.0 \leq X \leq 1, \quad Y = 0.0 \left. \vphantom{0.0 \leq X \leq 1} \right\} T = 1, \quad \text{heated wall} \quad (2.1.13)$$

$$0.0 \leq X \leq 1, \quad Y = 1.0 \left. \vphantom{0.0 \leq X \leq 1} \right\} \frac{\partial T}{\partial n} = 0, \quad \text{adiabatic portion} \quad (2.1.14)$$

$$\left. \begin{array}{l} 0.0 \leq Y \leq 1.0, \quad X = 0.0 \\ 0.0 \leq Y \leq 1.0, \quad X = 1.0 \end{array} \right\} T = 0 \quad \text{cooled wall.} \quad (2.1.15)$$

$$U = V = 0. \quad (2.1.16)$$

The heat transfer rate from the heated source to the flow regime is measured by Nusselt number, which is an important physical quantity of interest in the flow configuration. It is computed as local and mean Nusselt number (when heat flow is consider global) along the heated portion and can be expressed as

$$Nu_{loc} = -\frac{k_{nf}}{k_f} \frac{\partial T}{\partial Y} \Big|_{Y=0}, \quad Nu_m = \int_s -\frac{k_{nf}}{k_f} \frac{\partial T}{\partial n} dX. \quad (2.1.17)$$

Where  $s$  is the heated source length and  $n$  is the normal direction to that length.

## 2.2 Thermophysical properties of nanofluid and dimensionless numbers

The flow dynamic and heat transfer properties which are required in the various considered problems in this thesis are described as follows.

### 2.2.1 Electrical and thermal conductivity

Thermal conductivity is the heat conduction capacity of a substance, since metals are the good conductors of heat, using this feature, the nano-metallic particles are added to thermo-fluid in order enhance its thermal conductivity. Maxwell [56] model for

electrical conductivity of nanofluid depicts that it is function of base fluid  $\sigma_f$ , particle conductivity  $\sigma_s$  and volume fraction  $\phi$ , represented as.

$$\sigma_{nf} = \sigma_f \left( 1 + \frac{3 \left( \frac{\sigma_s}{\sigma_f} - 1 \right) \phi}{\left( \frac{\sigma_s}{\sigma_f} + 2 \right) - \left( \frac{\sigma_s}{\sigma_f} - 1 \right) \phi} \right). \quad (2.2.1)$$

In this thesis we have followed the combined model for thermal conductivity of nanofluid presented by Koo and Kleinstreuer [57], Li [58], Maxwell [56] formulated as

$$k_{nf} = k_{static} + k_{Brownian}, \quad (2.2.2)$$

$k_{static}$  is defined by Maxwell [56] as

$$k_{static} = k_f \left( 1 + \frac{3 \left( \frac{k_s}{k_f} - 1 \right) \phi}{\left( \frac{k_s}{k_f} + 2 \right) - \left( \frac{k_s}{k_f} - 1 \right) \phi} \right), \quad (2.2.3)$$

where the dynamic part is given by [57]

$$k_{Brownian} = 5 \times 10^4 \phi (\rho C_p)_f \sqrt{\frac{K_b T_0}{\rho_s D_s}} f(T_0, \phi). \quad (2.2.4)$$

Here, ( $K_b = 1.38 \times 10^{-23}$ ,  $T_0 = 0.5(T_h - T_C)$ ) specify the Boltzmann constant and average temperature while  $D_s$  is the diameter of nanoparticles.

The function  $f(T_0, \phi)$  in equation (2.2.4) is modified by Li [58] and presented a new function  $\zeta$  thus the relation reduces as

$$k_{Brownian} = 5 \times 10^4 \phi (\rho C_p)_f \sqrt{\frac{k_b T_0}{\rho_s D_s}} \zeta(T_0, \phi, D_s), \quad (2.2.5)$$

the modified function  $\zeta$  is given by:

$$\begin{aligned} \zeta(T_0, \phi, D_s) = & (a_1 + a_2 \ln D_s + a_3 \ln \phi + a_4 \ln D_s \ln \phi + a_5 \ln D_s^2) \ln T_0 + \\ & a_6 + a_7 \ln D_s + a_8 \ln \phi + a_9 \ln D_s \ln \phi + a_{10} \ln D_s^2. \end{aligned} \quad (2.2.6)$$

In above equation (2.2.6) the coefficients  $a_1 - a_{10}$  and numerical values of thermo-physical properties for *CuO*-water are shown in table 2.1 and 2.2.

## 2.2.2 Viscosity of nanofluids

Viscosity is the resistance of a fluid to flow, in the case of nanofluid, it is very important in its applications. Here for considered the effective viscosity (for *CuO* nanoparticles) in-terms of static and Brownian motion described in Koo and Kleinstreuer [59] can be expressed as

$$\mu_{nf} = \mu_{static} + \mu_{Brownian} = \frac{\mu_f}{(1 - \phi)^{2.5}} + \frac{k_{Brownian} \mu_f}{k_f Pr}, \quad (2.2.7)$$

where the static part in (2.2.7) is contributed by Brinkman [60] model for the viscosity of nanofluid, given by

$$\mu_{static} = \frac{\mu_f}{(1 - \phi)^{2.5}}. \quad (2.2.8)$$

## 2.2.3 Specific heat and density of nanofluid

Volumetric specific heat capacity of a substance is the amount of heat per unit volume its temperature by one Kelvin. For nanofluid considered in this work we have used the analysis and formulation by Zhou et al. [61] and Pak-cho [62] for specific volumetric heat capacity at a constant atmospheric pressure and is defined as

$$(\rho C_p)_{nf} = (1 - \phi)(\rho C_p)_f + \phi(\rho C_p)_s, \quad (2.2.9)$$

where the density for nanofluid is given by Xaun and Roetzel [63]

$$\rho_{nf} = (1 - \phi)\rho_f + \phi\rho_s. \quad (2.2.10)$$

## 2.2.4 Prandtl number

Prandtl number determine the heat flux between a solid body and moving fluid. It specifies the ratio of momentum diffusivity (or kinematic viscosity which posses the



resistance to shear flow) to thermal diffusivity. It can be written as

$$\begin{aligned} Pr &= \frac{\text{momentum diffusivity}}{\text{thermal diffusivity}} \\ &= \frac{\nu_f}{\alpha_f} = \frac{\mu_f C_p}{k_f}. \end{aligned} \quad (2.2.11)$$

$\mu_f$  is the dynamic viscosity,  $C_p$  shows the specific heat,  $k_f$  is the thermal conductivity. Moreover, Conduction (thermal diffusivity) dominates convection (momentum diffusivity) for a small value of Prandtl number ( $Pr \ll 1$ ). While for larger values ( $Pr \gg 1$ ), convection process occurs, which is more effective than conduction in transferring energy.

### 2.2.5 Grashof number

It is the dimensionless parameter which signifies the free (natural) convection. Grashof number is identified as the ratio of buoyancy (arises due to density differences) to viscous forces (resistive forces which arise with in fluid flow) acting on a fluid. It is also the natural convection analogue of Reynolds number in the forced convection. Since, free convection is initiated by density variation, which occurs due to temperature difference in the fluid. With the increase in temperature, density decreases which causes the fluid to rise, this phenomenon is caused by buoyancy forces. The resistance to such motion is controlled by Grashof number. It can be expressed as

$$Gr = \frac{g\beta_f(T_h - T_c)l^3}{\nu_f^2} = \frac{\text{buoyancy forces}}{\text{viscous forces}}, \quad (2.2.12)$$

$\beta_f$  (=thermal expansion coefficient),  $\nu_f$  (=kinematic viscosity of fluid),  $l$  (=characteristic length of domain).

### 2.2.6 Rayleigh number

Rayleigh ( $Ra$ ) and Grashof ( $Gr$ ) numbers are closely related and both depict the natural (free) convection ( $Gr$ ) and heat transfer ( $Ra$ ). It can also be interpreted

as the dimensionless number which control the destabilizing effects of buoyancy and stabilizing effect of viscosity. Rayleigh parameter is mathematically represent as the product of Grashof and Prandtl number, and can be written as

$$Ra = \text{Pr} \times Gr = \frac{\beta_f(T_h - T_c)l^3}{\nu_f\alpha_f}. \quad (2.2.13)$$

### 2.2.7 Reynolds number

The concept of Reynolds number ( $Re$ ) was introduced by Stokes [64], it describes the flow behavior of the different fluids. Reynolds number describe the relationship between inertial and viscous forces. It illustrates whether the flow is laminar or turbulent. Larger Reynolds number implies higher inertial forces which means that density and velocity of the fluid is maximum enough as compared to viscous forces. Which leads to a turbulent flow in the regime as viscous forces cannot prevent the rapid fluctuation of fluid in that case.

$$Re = \frac{\text{inertial forces}}{\text{viscous forces}} = \frac{\rho_f V_0 l}{\mu_f} = \frac{V_0 l}{\nu_f}, \quad (2.2.14)$$

$V_0$  is the maximum velocity of the fluid,  $l$  identify the characteristic length,  $\rho_f, \nu_f$  denote the density and kinematic viscosity of acting fluid.

### 2.2.8 Richarson number

Richardson number ( $Ri$ ) is another important dimensionless parameter which correlate the forced convection and natural convection. Mathematically it is the ratio of Grashof number ( $Gr$ ) to the square of Reynolds number ( $Re$ ), i.e.,

$$Ri = \frac{Gr}{Re^2} = \frac{\text{buoyancy forces}}{\text{inertial forces}}. \quad (2.2.15)$$

When  $Ri < 1$  the basic mode of flow is force convection while for  $Ri > 1$  the flow is maintained by natural convection. Thus, smaller  $Re$  implies higher  $Ri$  which signifies the buoyancy driven flow dominated the forced convection.

### 2.2.9 Nusselt number

Nusselt number is the dimensionless quantity that associates heat transfer rate in the fluid, i.e. The convection to conduction heat transfer. In convective heat transportation thermal energy propagate from the source to the flowing fluid and is directly proportional to the temperature differences among them. This relationship between heat flux and temperature difference is quantified by convective heat transfer coefficient  $h_{\text{conv}}$ .

$$q_{\text{conv}} = h_f (T_h - T_C). \quad (2.2.16)$$

Heat transport is also characterized by the direct thermal conduction due to the existence of no slip boundary condition in the flow configuration. Hence, in this case Fourier's law describe such heat transfer, i.e.,

$$q_{\text{cond}} = -k_f \nabla \bar{T}. \quad (2.2.17)$$

Since, the fact that heat flux from the source boundary must be identical thus, (2.2.16) and (2.2.17) reduces to:

$$\begin{aligned} q_{\text{conv}} &= q_{\text{cond}}, \\ h_f (T_h - T_C) &= k_f \nabla \bar{T}, \\ \frac{h_f}{k_f} &= \frac{-\nabla \bar{T}}{(T_h - T_C)}. \end{aligned} \quad (2.2.18)$$

This ratio is determined by Nusselt number can be written as:

$$\begin{aligned} Nu &= \frac{\text{coefficient of convection}}{\text{coefficient of conduction}} = \frac{h_f l}{k_f} \\ &= \frac{q_{\text{cond}} l}{(T_h - T_C)}. \end{aligned} \quad (2.2.19)$$

In this study it reduces to, i.e., Nusselt number can be computed along the heated boundary locally as;  $q_{\text{cond}} = -k_{nf} \frac{\partial \bar{T}}{\partial x}$  and by use of (2.1.8) it becomes

$$Nu = = -\frac{k_{nf}}{k_f} \frac{\partial T}{\partial Y} \Big|_{Y=0}, \quad (2.2.20)$$

While, assuming heat transfer rate globally along the heated surface it can be written as

$$Nu_m = \int_s -\frac{k_{nf}}{k_f} \frac{\partial T}{\partial n} dX. \quad (2.2.21)$$

Moreover, Nusselt number can also be represented as:

$$\begin{aligned} Nu &= f(Ra, Pr) && \text{(natural convection),} \\ Nu &= f(Re, Pr) && \text{(forced convection).} \end{aligned} \quad (2.2.22)$$

Table 2.1: Thermophysical properties water-based *CuO* nanoparticles.

Physical properties	Water	Nanoparticles ( <i>CuO</i> )
$\rho(\text{kg/m}^3)$	997.1	6500
$C_p(\text{J/kg K})$	4179	540
$k_f(\text{W/mK})$	0.613	18
$\beta \times 10^5(\text{K}^{-1})$	21	29
$D_s(\text{nm})$	-	45

Table 2.2: Coefficient values of nanofluid.

Parameter	<i>CuO</i> -water	Parameter	<i>CuO</i> -water
$a_1$	-26.593310846	$a_6$	48.40336955
$a_2$	-0.403818333	$a_7$	-9.787756683
$a_3$	-33.3516805	$a_8$	190.245610009
$a_4$	-1.915825591	$a_9$	10.9285386565
$a_5$	6.42185846658E-02	$a_{10}$	-0.72009983664

## 2.3 Numerical solution with finite element method

### 2.3.1 General theory and introduction

In many biological, economic and physical phenomena involve partial differential equations in its mathematical modeling, such as pattern formation (spatial tissue structure in morphogenesis), blood flow, chemotaxis, derivative valuation, elasticity, fluid dynamics etc. The mathematical treatment of these partial differential equation based models is crucial and challenging for the adequate solution of practical problems. The analytical or closed-form solution of these equations (PDE's) is not possible because such problems involve different kind of complexity, like, inequality constraint, interfaces, singularities etc. The approximate methods of analysis are the possible and alternative approach to evaluate the mathematical system of the physical processes. Following that, the partial differential equations governing the physical situation are transformed into the discrete algebraic system of that problem. In the numerical methods analysis variational techniques (Least square, Rayleigh-Ritz and Galerkin methods) have been adopted to find the approximate solutions over a domain. In this method the governing equations system is formulated in equivalent weighted integral form. The approximated solution be considered as linear combination of unknown constant coefficients and appropriate base functions. In the variational techniques it is difficult to construct approximated solution over arbitrary domain. To overcome this disadvantage finite element analysis make use of variational method and provide a systematic procedure to approximate solution over sub-regions of the domain. Finite element method is a computational technique that can solve complicated mathematical model (in-terms of PDE's) developed in arbitrary complex domain. This method is well studied for the physical problem of science and engineering such as, elasticity, diffusion, fluid dynamics, solid mechanics,

thermodynamics, electromigration etc. The superiority of this method over other competing technique is owing to its three distinctive aspects, i.e., the complicated domain of interest is represented in equally (mostly) divided subdomains known as finite elements. Then, over each of these elements the approximation functions are assigned which can be described by combination of algebraic polynomials. Third, the of nodal values (undetermined coefficients) can be obtained by use of these algebraic expression to satisfy the governing equations (weighted-integral form) over each element. The approximated algebraic functions are obtained utilizing the concepts of interpolation theory and are hence named interpolation functions. These approximation polynomials depend on the order of governing equation and number of nodes in each element.

## **2.3.2 Finite element solution procedure**

The principle of finite element analysis involve the following steps

### **2.3.2.1 Domain discretization**

The solution domain is divided into finite number of sub-domains, each of them is known as element. These finite elements formed finite element mesh. Here we have discretized the domain into triangular element mesh connected to each other at points called nodes as in figure 2.2.

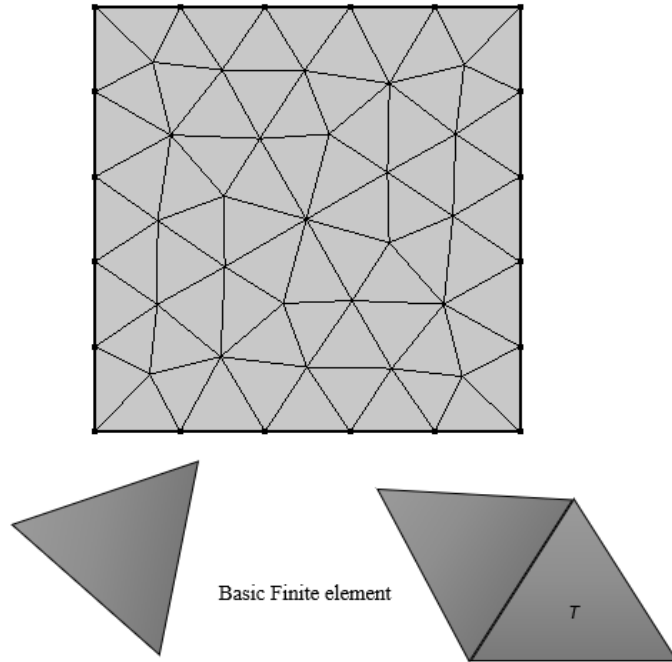


Figure 2.2: Discretization of the flow domain

### 2.3.2.2 Element equations

The local element equations are formed by assuming the a set appropriate functions to each element that will describe the solution, most often, polynomials are chosen as basis or shape functions. Which require  $n$  nodes of elements if there is  $n$  unknown coefficients of trail functions. The Galerkin approach is adopted to form the matrix equation in each finite element of the domain.

### 2.3.2.3 Global equations

The global equation system for the whole domain under investigation is formed by combining all the local element equations. The boundary conditions should be applied to before the solutions of combined local element equations.

### 2.3.2.4 Solution of global equations

To obtain the continuous solution the global equation system can be solved by iterative techniques, the nodal values (unknowns) of the required functions are obtained after solution procedure.

## 2.4 Finite element method implementation

Following the above steps and implementing on the considered problem in this chapter and same for the other chapters as well in the thesis, we have the domain of interest as shown in figure 2.1 is divided into collection of sub-regions, here triangular element, known as finite element mesh (shown in figure 2.2). In discretization, the solution in the form of continuous function is computed at the nodes of each triangular element. Since the discretization is done the next is to formulate the weak form of the mathematical system (2.1.9)-(2.1.12). We multiply equations (2.1.9)-(2.1.12) by weighted functions  $W_i = (W_1, W_2, W_3, W_4)$  which are later on in the formulation, be replaced by the  $i$ th approximated interpolation functions for  $(P, U, V, T)$  and integrated over the domain of investigation  $(\Omega^d)$ . Hence, the weak-formulation over discretized region  $\Omega^d$  reduces as:

$$\int_{\Omega^d} \left\{ \frac{\partial U}{\partial X} + \frac{\partial V}{\partial Y} \right\} W_1 dX dY = 0, \quad (2.4.1)$$

$$\int_{\Omega^d} \left\{ U \frac{\partial U}{\partial X} + V \frac{\partial U}{\partial Y} + \frac{\rho_f}{\rho_{nf}} \frac{\partial P}{\partial X} - \frac{\mu_{nf}}{\mu_f} \frac{\rho_f}{\rho_{nf}} \text{Pr} \left( \frac{\partial^2 U}{\partial X^2} + \frac{\partial^2 U}{\partial Y^2} \right) - F_X \right\} W_2 dX dY = 0, \quad (2.4.2)$$

$$\int_{\Omega^d} \left\{ U \frac{\partial V}{\partial X} + V \frac{\partial V}{\partial Y} + \frac{\rho_f}{\rho_{nf}} \frac{\partial P}{\partial Y} - \frac{\mu_{nf}}{\mu_f} \frac{\rho_f}{\rho_{nf}} \text{Pr} \left( \frac{\partial^2 V}{\partial X^2} + \frac{\partial^2 V}{\partial Y^2} \right) - F_Y \right\} W_3 dX dY = 0, \quad (2.4.3)$$

$$\int_{\Omega^d} \left\{ U \frac{\partial T}{\partial X} + V \frac{\partial T}{\partial Y} - \frac{\alpha_{nf}}{\alpha_f} \left( \frac{\partial^2 T}{\partial X^2} + \frac{\partial^2 T}{\partial Y^2} \right) \right\} W_4 dX dY = 0, \quad (2.4.4)$$

where  $F_X = 0$  and  $F_Y = \frac{(\rho\beta)_{nf}}{(\rho\beta)_f} \frac{\rho_f}{\rho_{nf}} Ra \text{Pr} T$  are the body forces in  $x, y$  equation components. Now the second step weak-formulation is integration by parts and in which the differentiation is evaluated equally among both the conservation equations and



test functions. The integration by parts is implemented over each term of momentum and energy equations except the body forces, the reduced system is as follow

$$\int_{\Omega^d} \left\{ \frac{\partial U}{\partial X} + \frac{\partial V}{\partial Y} \right\} W_1 dXdY = 0, \quad (2.4.5)$$

$$\int_{\Omega^d} \left\{ \left( U \frac{\partial U}{\partial X} + V \frac{\partial U}{\partial Y} + F_X \right) W_2 - \frac{\rho_f}{\rho_{nf}} P \frac{\partial W_2}{\partial X} + \frac{\mu_{nf}}{\mu_f} \frac{\rho_f}{\rho_{nf}} \text{Pr} \frac{\partial U}{\partial X} \frac{\partial W_2}{\partial X} + \frac{\mu_{nf}}{\mu_f} \frac{\rho_f}{\rho_{nf}} \text{Pr} \frac{\partial U}{\partial Y} \frac{\partial W_2}{\partial Y} \right\} dXdY - \int_{\Gamma^d} W_2 n_X dS = 0, \quad (2.4.6)$$

$$\int_{\Omega^d} \left\{ \left( U \frac{\partial V}{\partial X} + V \frac{\partial V}{\partial Y} + F_Y \right) W_3 - \frac{\rho_f}{\rho_{nf}} P \frac{\partial W_3}{\partial Y} + \frac{\mu_{nf}}{\mu_f} \frac{\rho_f}{\rho_{nf}} \text{Pr} \frac{\partial V}{\partial X} \frac{\partial W_3}{\partial X} + \frac{\mu_{nf}}{\mu_f} \frac{\rho_f}{\rho_{nf}} \text{Pr} \frac{\partial V}{\partial Y} \frac{\partial W_3}{\partial Y} \right\} dXdY - \int_{\Gamma^d} W_3 n_Y dS = 0, \quad (2.4.7)$$

$$\int_{\Omega^d} \left\{ \left( U \frac{\partial T}{\partial X} + V \frac{\partial T}{\partial Y} \right) W_4 - \frac{\alpha_{nf}}{\alpha_f} \left( \frac{\partial T}{\partial X} \frac{\partial W_4}{\partial X} + \frac{\partial T}{\partial Y} \frac{\partial W_4}{\partial Y} \right) \right\} dXdY - \int_{\Gamma^d} W_4 Q_n dS = 0. \quad (2.4.8)$$

With outward unit-normal  $(n_X, n_Y)$  components and normal heat flux  $Q_n$  to the boundary  $S$ . Note that, continuity equation (2.4.5) corresponds to the volume change due to external force,  $W_1$  must be similar to that force. Since, Pressure is responsible for the volume change so  $W_1 \sim P$ . In view of that pressure is assume to be secondary quantity so following (2.4.5) there is no evaluation of boundary integral with respect to  $W_1$ . The main difficulty usually faced in the solution of Navier Stokes equation is the incompressibility condition appearing in the configuration. Thus, in the above system (2.4.5)-(2.4.8) all functions  $(P, U, V, T)$  are all counted as un-knowns, this implies that numerical computation become difficult in higher dimensional problem. To beat this challenge the penalty finite element approach [65–67] is utilized here which relax incompressibility condition. The principle of penalty formulation is to perturbate continuity equation (2.4.5) by a small number containing pressure. Thus, equation (2.4.5) can be represented as:

$$\int_{\Omega^d} \left\{ \frac{\partial U}{\partial X} + \frac{\partial V}{\partial Y} \right\} W_i dXdY = \int_{\Omega^d} \frac{-P}{\lambda} W_i dXdY, \quad (2.4.9)$$

since  $P$  is assume to be finite and choosing  $\lambda$  sufficiently large then the above equation (2.4.9) so far so good approximation to equation (2.4.5). The Now substituting (2.4.9)

in (2.4.6) and (2.4.7) the weak formulation reduces as

$$\int_{\Omega^d} \left\{ \left( U \frac{\partial U}{\partial X} + V \frac{\partial U}{\partial Y} + F_X \right) W_2 + \frac{\rho_f}{\rho_{nf}} \lambda \left( \frac{\partial U}{\partial X} + \frac{\partial V}{\partial Y} \right) \frac{\partial W_2}{\partial X} + \frac{\mu_{nf}}{\mu_f} \frac{\rho_f}{\rho_{nf}} \text{Pr} \frac{\partial U}{\partial X} \frac{\partial W_2}{\partial X} + \frac{\mu_{nf}}{\mu_f} \frac{\rho_f}{\rho_{nf}} \text{Pr} \frac{\partial U}{\partial Y} \frac{\partial W_2}{\partial Y} \right\} dX dY - \int_{\Gamma^d} W_2 n_X dS = 0, \quad (2.4.10)$$

$$\int_{\Omega^d} \left\{ \left( U \frac{\partial V}{\partial X} + V \frac{\partial V}{\partial Y} + F_Y \right) W_3 + \frac{\rho_f}{\rho_{nf}} \lambda \left( \frac{\partial U}{\partial X} + \frac{\partial V}{\partial Y} \right) \frac{\partial W_3}{\partial Y} + \frac{\mu_{nf}}{\mu_f} \frac{\rho_f}{\rho_{nf}} \text{Pr} \frac{\partial V}{\partial X} \frac{\partial W_3}{\partial X} + \frac{\mu_{nf}}{\mu_f} \frac{\rho_f}{\rho_{nf}} \text{Pr} \frac{\partial V}{\partial Y} \frac{\partial W_3}{\partial Y} \right\} dX dY - \int_{\Gamma^d} W_3 n_Y dS = 0. \quad (2.4.11)$$

This provide the elimination of pressure and fulfill the incompressibility condition. The only un-knowns left in the conservation equations are velocity and temperature profile. The discrete domain is interpolated by assuming test and trail functions for velocity components and temperature profile. The approximated solution is obtain by expanding the dependent variable in the form

$$U \approx \sum_{j=1}^n U_j \Phi_j^h, \quad V \approx \sum_{j=1}^n V_j \Phi_j^h, \quad T \approx \sum_{j=1}^n T_j \Psi_j^h. \quad (2.4.12)$$

Here,  $U_j, V_j, T_j$  (unknowns) depict the values of functions ( $U, V, T$ ) at associated node  $j$ ,  $h$  represent element,  $\Phi_j^h$  are the interpolated basis function assumed at each node  $j$  of element  $h$  and  $n$  describe the total number of nodes in a element. Make use of (2.4.12) in (2.4.8), (2.4.10) and (2.4.11) the resulting finite element model in-term of algebraic equations reduces as

$$\begin{aligned} & \sum_{j=1}^n U_j \int_{\Omega^d} \left( \sum_{i,j=1}^n U_j \Phi_j^h \frac{\partial \Phi_j^h}{\partial X} \Phi_i^h + \sum_{i,j=1}^n V_j \Phi_j^h \frac{\partial \Phi_j^h}{\partial Y} \Phi_i^h \right) dX dY + \frac{\rho_f}{\rho_{nf}} \lambda \int_{\Omega^d} \left( \sum_{i,j=1}^n U_j \frac{\partial \Phi_j^h}{\partial X} \frac{\partial \Phi_i^h}{\partial X} + \right. \\ & \left. \sum_{i,j=1}^n V_j \frac{\partial \Phi_j^h}{\partial X} \frac{\partial \Phi_i^h}{\partial Y} \right) dX dY + \frac{\mu_{nf}}{\mu_f} \frac{\rho_f}{\rho_{nf}} \text{Pr} \int_{\Omega^d} \left( \sum_{i,j=1}^n U_j \frac{\partial \Phi_j^h}{\partial X} \frac{\partial \Phi_i^h}{\partial X} \right) dX dY + \\ & \frac{\mu_{nf}}{\mu_f} \frac{\rho_f}{\rho_{nf}} \text{Pr} \int_{\Omega^d} \left( \sum_{i,j=1}^n U_j \frac{\partial \Phi_j^h}{\partial Y} \frac{\partial \Phi_i^h}{\partial Y} \right) dX dY + \int_{\Omega^d} F_X \Phi_i^h dX dY - \int_{\Gamma^d} \Phi_i^h n_X dS = 0, \quad (2.4.13) \end{aligned}$$

$$\begin{aligned}
& \sum_{j=1}^n V_j \int_{\Omega^d} \left( \sum_{i,j=1}^n U_j \Phi_j^h \frac{\partial \Phi_j^h}{\partial X} \Phi_i^h + \sum_{i,j=1}^n V_j \Phi_j^h \frac{\partial \Phi_j^h}{\partial Y} \Phi_i^h \right) dXdY + \frac{\rho_f}{\rho_{nf}} \lambda \int_{\Omega^d} \left( \sum_{i,j=1}^n U_j \frac{\partial \Phi_i^h}{\partial Y} \frac{\partial \Phi_j^h}{\partial X} + \right. \\
& \left. \sum_{i,j=1}^n V_j \frac{\partial \Phi_j^h}{\partial Y} \frac{\partial \Phi_i^h}{\partial Y} \right) dXdY + \frac{\mu_{nf}}{\mu_f} \frac{\rho_f}{\rho_{nf}} \text{Pr} \int_{\Omega^d} \left( \sum_{i,j=1}^n V_j \frac{\partial \Phi_j^h}{\partial X} \frac{\partial \Phi_i^h}{\partial X} \right) dXdY + \\
& \frac{\mu_{nf}}{\mu_f} \frac{\rho_f}{\rho_{nf}} \text{Pr} \int_{\Omega^d} \left( \sum_{i,j=1}^n V_j \frac{\partial \Phi_j^h}{\partial Y} \frac{\partial \Phi_i^h}{\partial Y} \right) dXdY + \int_{\Omega^d} F_Y \Phi_i^h dXdY - \int_{\Gamma^d} \Phi_i^h n_Y dS = 0, \quad (2.4.14)
\end{aligned}$$

$$\begin{aligned}
& \sum_{j=1}^n T_j \int_{\Omega^d} \left( \sum_{i,j=1}^n U_j \Phi_j^h \frac{\partial \Psi_j^h}{\partial X} \Psi_i^h + \sum_{i,j=1}^n V_j \Phi_j^h \frac{\partial \Psi_j^h}{\partial Y} \Psi_i^h \right) dXdY - \frac{\alpha_{nf}}{\alpha_f} \int_{\Omega^d} \left( \sum_{i,j=1}^n T_j \frac{\partial \Psi_j^h}{\partial X} \frac{\partial \Psi_i^h}{\partial X} + \right. \\
& \left. \sum_{i,j=1}^n T_j \frac{\partial \Psi_j^h}{\partial Y} \frac{\partial \Psi_i^h}{\partial Y} \right) dXdY - \int_{\Gamma^d} \Psi_i^h Q_n dS = 0. \quad (2.4.15)
\end{aligned}$$

In matrix notation it can be written as

$$\left( \begin{bmatrix} G^{11} & G^{12} \\ G^{21} & G^{22} \end{bmatrix} + \begin{bmatrix} H^C & 0 \\ 0 & H^C \end{bmatrix} + \begin{bmatrix} K^D & 0 \\ 0 & K^D \end{bmatrix} \right) \begin{Bmatrix} U \\ V \end{Bmatrix} = \begin{Bmatrix} S^1 \\ S^2 \end{Bmatrix} \quad (2.4.16)$$

Here the coefficient matrix are represented as

$$\begin{aligned}
G_{ij}^{11} &= \frac{\rho_f}{\rho_{nf}} \lambda \int_{\Omega^d} \frac{\partial \Phi_j^h}{\partial X} \frac{\partial \Phi_i^h}{\partial X} dXdY, \quad G^{12} = \frac{\rho_f}{\rho_{nf}} \lambda \int_{\Omega^d} \frac{\partial \Phi_i^h}{\partial X} \frac{\partial \Phi_j^h}{\partial Y} dXdY, \quad G^{21} = (G^{12})^T, \\
G^{22} &= \frac{\rho_f}{\rho_{nf}} \lambda \int_{\Omega^d} \frac{\partial \Phi_j^h}{\partial Y} \frac{\partial \Phi_i^h}{\partial Y} dXdY, \quad H_{ij}^C = \int_{\Omega^d} \left( U \frac{\partial \Phi_j^h}{\partial X} + V \frac{\partial \Phi_j^h}{\partial Y} \right) \Phi_i^h dXdY, \quad (2.4.17)
\end{aligned}$$

$$K^D = M_{ij}^{11} + M_{ij}^{22} = \frac{\mu_{nf}}{\mu_f} \frac{\rho_f}{\rho_{nf}} \text{Pr} \int_{\Omega^d} \frac{\partial \Phi_j^h}{\partial X} \frac{\partial \Phi_i^h}{\partial X} dXdY + \frac{\mu_{nf}}{\mu_f} \frac{\rho_f}{\rho_{nf}} \text{Pr} \int_{\Omega^d} \frac{\partial \Phi_j^h}{\partial Y} \frac{\partial \Phi_i^h}{\partial Y} dXdY, \quad (2.4.18)$$

$$S_i^1 = \int_{\Omega^d} F_X \Phi_i^h dXdY - \int_{\Gamma^d} \Phi_i^h n_X dS = 0, \quad S_i^2 = \int_{\Omega^d} F_Y \Phi_i^h dXdY - \int_{\Gamma^d} \Phi_i^h n_Y dS = 0. \quad (2.4.19)$$

The thermal profile (2.4.15) takes the form

$$[E^C] \{T\} = \{Q^s\}, \quad (2.4.20)$$

where

$$\begin{aligned}
E_{ij}^C &= \int_{\Omega^d} \left( U \frac{\partial \Psi_j^h}{\partial X} + V \frac{\partial \Psi_j^h}{\partial Y} \right) \Psi_i^h dXdY - \frac{\alpha_{nf}}{\alpha_f} \int_{\Omega^d} \left( \frac{\partial \Psi_j^h}{\partial X} \frac{\partial \Psi_i^h}{\partial X} + \frac{\partial \Psi_j^h}{\partial Y} \frac{\partial \Psi_i^h}{\partial Y} \right) dXdY, \\
Q^s &= \int_{\Gamma^d} \Psi_i^h Q_n dS. \quad (2.4.21)
\end{aligned}$$

The reduced finite element model (2.4.16) and (2.4.20) is then solved iteratively after imposing the corresponding boundary condition. Here, implementing the conditions

the boundary integrals in momentum source (2.4.19) and energy source (2.4.21) vanish because the considered test functions are assumed to be zero on boundaries.

## 2.5 Mesh independence and results validation

The finite element simulations demand its accuracy and convergence to be checked. For this purpose, in the first step we have performed mesh independence test and in the next step the simulations are validated by comparing it with existing publish results. To attain that objectives we have calculated results for Nusselt number along heated wall at various mesh having non uniform triangular elements. we started with the initial coarse mesh containing 462 elements and 3984 degree of freedom (DOFs) which was refined up-to four levels with 39056 elements and 315144 DOFs shown in Table 2.3. And from this numerical experiment it is concluded that at one stage the variation in the results for Nusselt number does not changes when the grid size is increased further. It was observed that error tends to zero thus it shows that the results is no more dependent on mesh size. Hence the claims comes true that the numerical experiment is grid independent. This test concluded that less than 1 % error is obtained for the results computed between 10618 and 39056 mesh elements. In view of this we have simulated our results against the non-uniform mesh having 10618 triangular elements.

Table 2.3: Grid independence test, values of Nusselt number at different mesh size.

DOFs	Triangular Elements	Nusselt	Error
3984	462	4.722171	1.3e-4
13592	1632	4.654755	8.8e-5
19712	2382	4.643975	3.9e-5
86344	10618	4.616778	1.4e-5
315144	39056	4.616701	1.0e-5

After confirming the grid in-dependency test proceeding to code validation. A comparison with previously publish experimental and numerical explorations by Calcagni et al. [68] is presented in figure 2.3. It can be seen from figure that our results (streamlines and isotherms) computed for Rayleigh number shows strong resemblance with the experimental and numerical outcomes for isotherms and streamlines. Further, in term of line graphs it observed that velocity profile in figure 2.4(a) computed against various  $Ra$  depict good agreement with the existing published results of Aminossadati and Ghasemi [69]. The Nusselt number result is also validated with the results of Reddy and Sreedevi [70]. The graph 2.4(b) reveals excellent resemblance with published results.

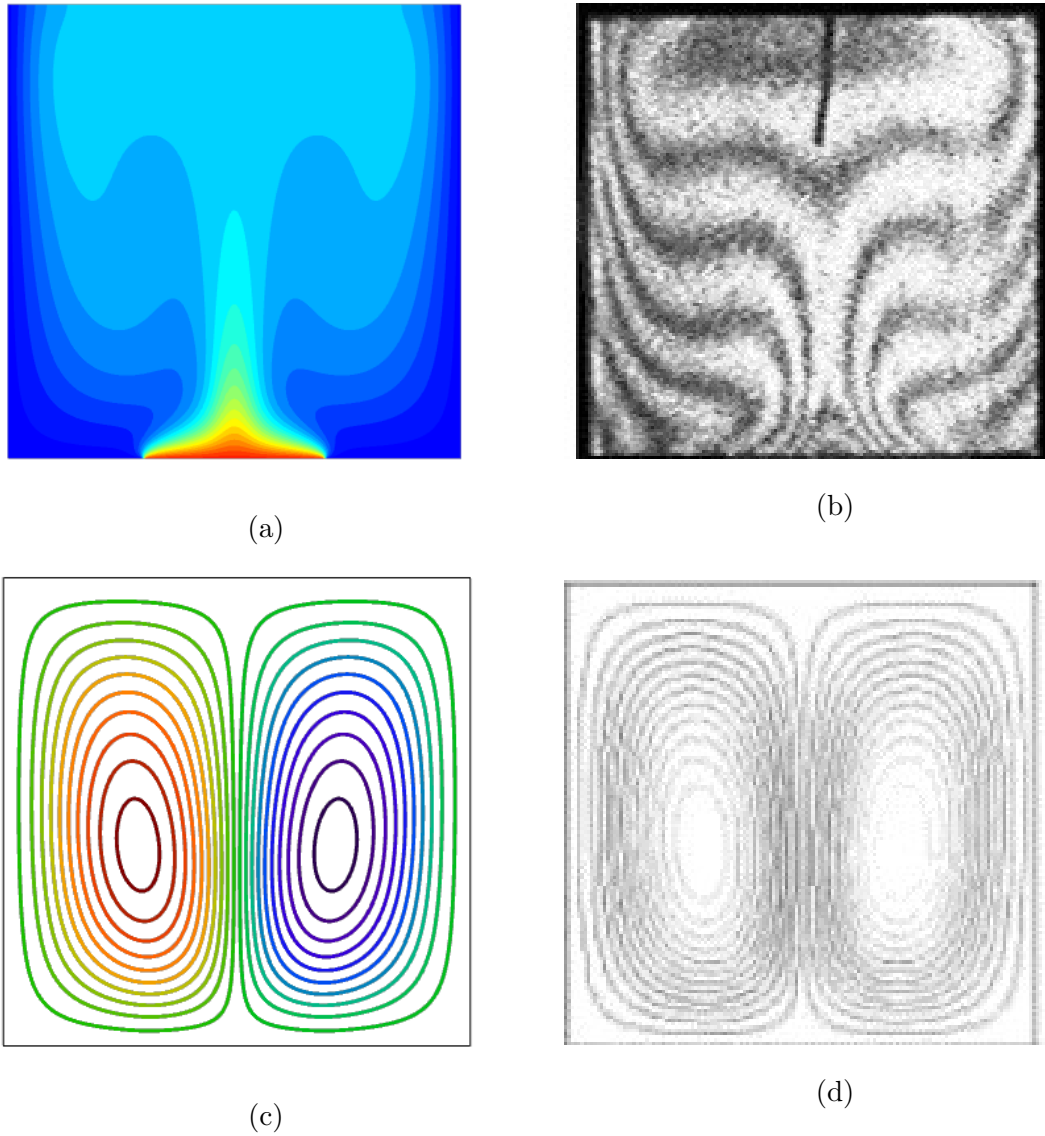


Figure 2.3: Comparison of present work (a) isotherms (c) streamlines with previous experimental (b) and numerical (d) results by Calcagni et al. [68] against  $Ra = 1.86 \times 10^5$ ,  $\phi = 0$ .

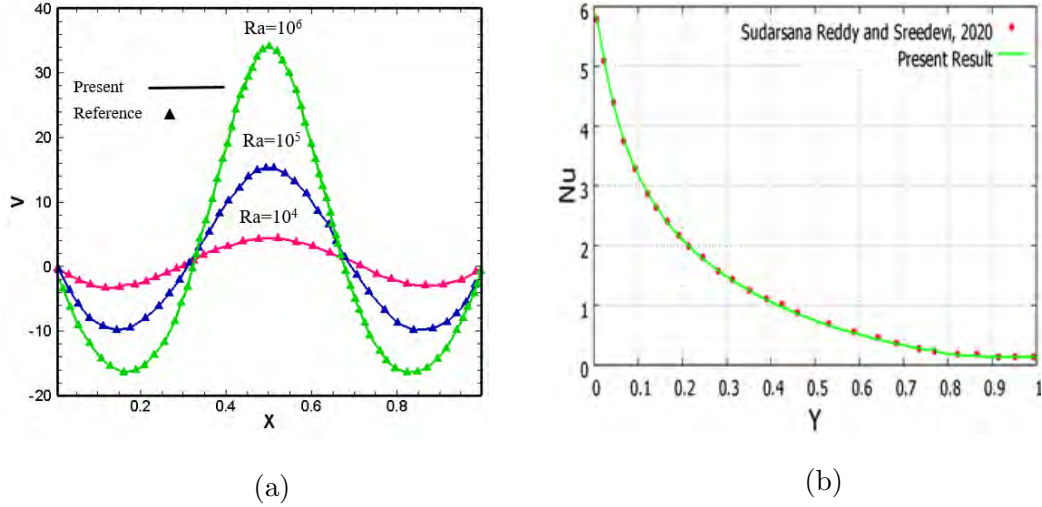
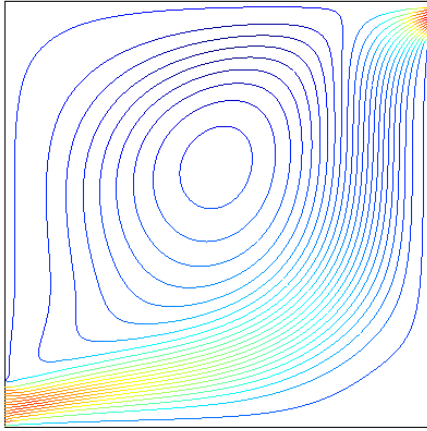
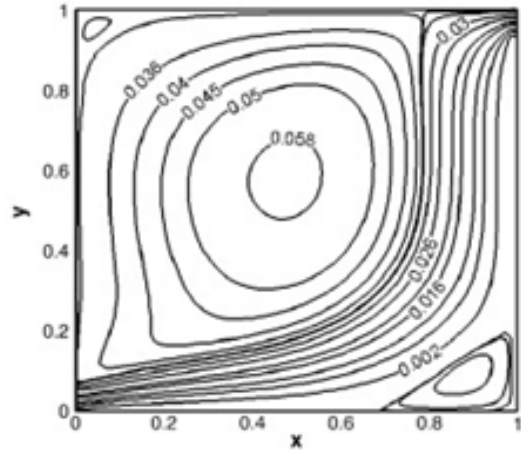


Figure 2.4: Comparison of present work velocity (a) with reference [70] and Nusselt number (b) with [69].

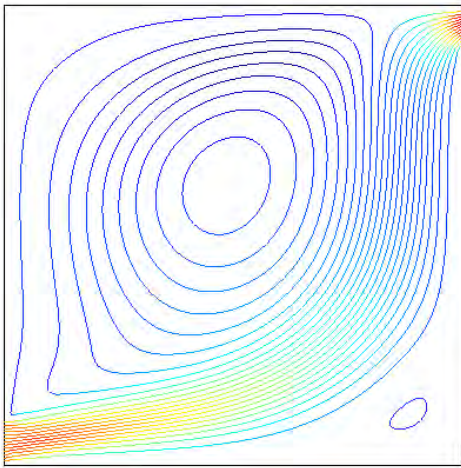
The simulation carried out against Richardson number is also validated with the existing literature. To perform this task we have compared our results with published articles by Shahi et al. [71] Rahman et al. [72]. Streamlines drawn against  $Ri = 0.1$  and  $Ri = 10$  are compared with results of Shahi et al. [71] shown in figures. 2.5(a–d). Further, numerical values of Nusselt number are also validated with results of Rahman et al. [72] presented in Table 2.4. Both the graphical and numerical compared results are in good agreement with existing literature. Hence, these experiments conclude that our results are accurate and the code is suitable for the simulation.



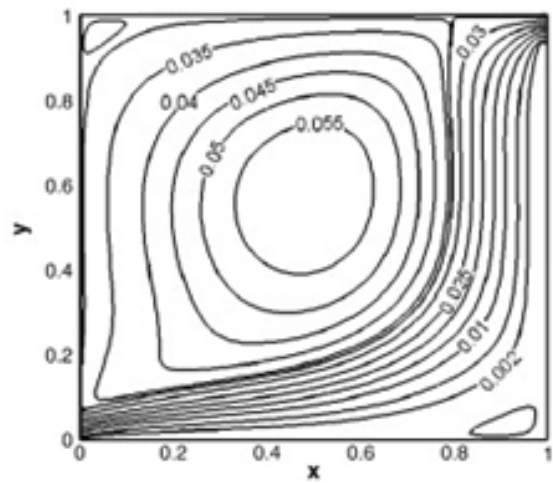
(a)



(b)



(c)



(d)

Figure 2.5: Streamlines comparison with Shahi et al. [71] at  $Ri = 0.1$  (a),(c) and  $Ri = 10$  (b), (d).



Table 2.4: Comparison of Nusselt number against  $Ri$  with Rahman et al. [72]

$Ri$	$Nu$ [72]	$Nu$ present	error
0.0	4.060	4.06315	0.07%
0.5	4.145	4.14032	0.11%
1.0	4.222	4.21842	0.08%
5.0	4.659	4.66475	0.12%
10	5.016	5.03118	0.30%

## 2.6 Concluding remarks

Form the validation study it is deduce that both the graphical and numerical compared results are in good agreement with existing literature. Hence, these experiments conclude that our results are accurate. Hence the code is suitable for the simulation.

# Chapter 3

## Finite Element simulations for natural convective flow of nanofluid in a rectangular cavity having corrugated heated rods

### 3.1 Introduction

In various geometrical shapes, investigations of natural convection have significant importance to technological and industrial development. Particularly, in chemical and nuclear reactors, energy conversion, metallurgical process, cooling of electronic devices, solar energy collector, lakes and reservoir, building insulation materials, food processing, etc. Nanofluids have considerably revolutionized the modern technological world and are found the best coolant in the various engineering applications. Such as in cooling of nuclear reactors, automotive, electronic cooling, refrigerators, solar collectors and various heat exchangers. Since, nanofluid with astonishing heat transit characteristics is the most discoursed topic of the time. The impact of nanoparticles

volume fraction is found to be useful in intensifying the heat transfer rate because of dominant convection involving complex system flow problems. Owing to such importance this chapter aims to investigation natural convection in a partially heated rectangular cavity containing water-based copper oxide nanofluid ( $CuO$ -water). The flow field and heat transfer inside the cavity are influenced by two corrugated heated rods. The mathematical translation of this physical configuration involve non-linear partial differential equations. Numerical solutions of the resulting differential system are obtained utilizing Finite Element Method. The results are executed for various controlling parameter and the simulations for flow field and thermal distribution are portrayed in terms of line graphs, streamlines and isotherms.

## 3.2 Mathematical formulation

Consider the steady two dimensional flow of  $Cu$ -water nanofluid in a partially heated rectangular cavity. The enclosure contains two heated corrugated rods with constant temperature  $T_h$ . The vertical walls of cavity are kept cold at constant temperature  $T_C$ . The outer heated boundaries of the cavity has a constant temperature  $T_h$ , while the remaining portions of the upper and lower wall are adiabatic. Figure 3.1 illustrates the geometry of the problem. The mesh generation for the numerical procedure is given in figure 3.2. Triangular mesh are considered in the domain, and for better results and accuracy we have generated maximum mesh at the inner heated rods.

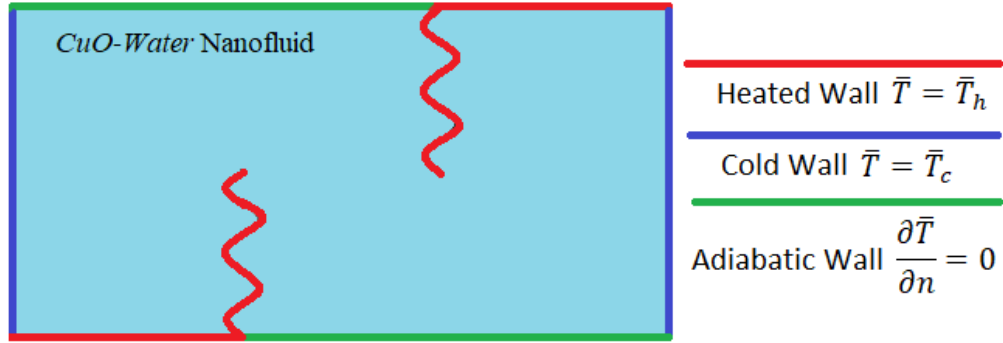


Figure 3.1: Geometry of the physical problem

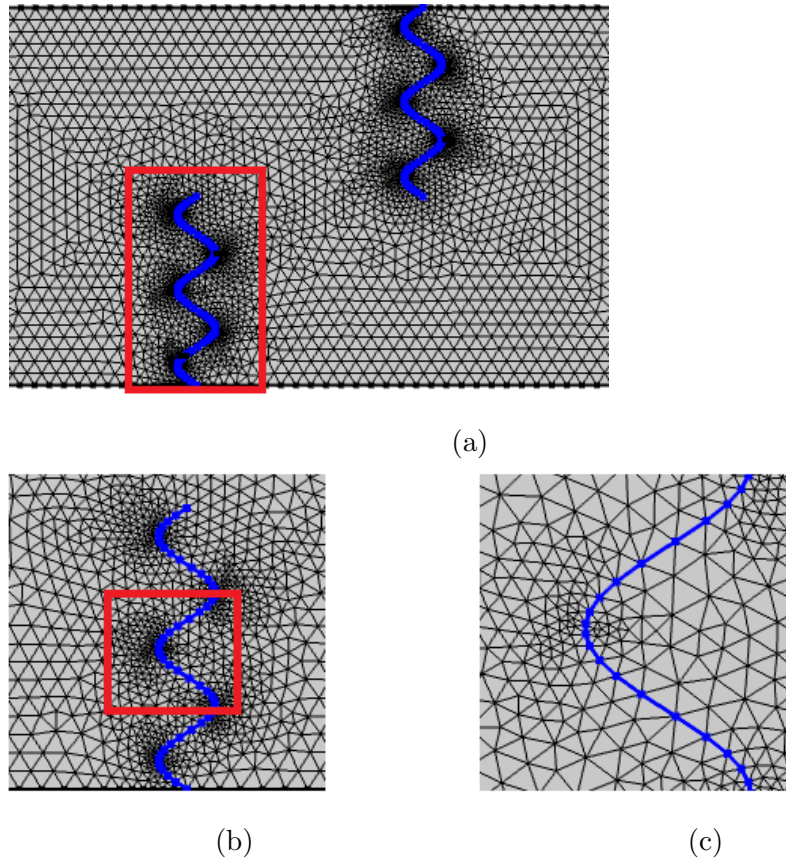


Figure 3.2: Mesh generation at different portion in physical domain.

The flow field is control by external pressure gradient and buoyancy force. Also considering the natural convection here and applying the Oberbeck-Boussinesq ap-

proximation the buoyancy term. Under these assumptions the governing problem obeys law of conservation of mass, momentum and energy as follow

$$\frac{\partial \bar{u}}{\partial \bar{x}} + \frac{\partial \bar{v}}{\partial \bar{y}} = 0, \quad (3.2.1)$$

$$\bar{u} \frac{\partial \bar{u}}{\partial \bar{x}} + \bar{v} \frac{\partial \bar{u}}{\partial \bar{y}} = -\frac{1}{\rho_{nf}} \frac{\partial \bar{p}}{\partial \bar{x}} + \nu_{nf} \left( \frac{\partial^2 \bar{u}}{\partial \bar{x}^2} + \frac{\partial^2 \bar{u}}{\partial \bar{y}^2} \right), \quad (3.2.2)$$

$$\bar{u} \frac{\partial \bar{v}}{\partial \bar{x}} + \bar{v} \frac{\partial \bar{v}}{\partial \bar{y}} = -\frac{1}{\rho_{nf}} \frac{\partial \bar{p}}{\partial \bar{y}} + \nu_{nf} \left( \frac{\partial^2 \bar{v}}{\partial \bar{x}^2} + \frac{\partial^2 \bar{v}}{\partial \bar{y}^2} \right) + \frac{(\rho\beta)_{nf}}{\rho_{nf}} g(\bar{T} - T_C), \quad (3.2.3)$$

$$\bar{u} \frac{\partial \bar{T}}{\partial \bar{x}} + \bar{v} \frac{\partial \bar{T}}{\partial \bar{y}} = \frac{k_{nf}}{(\rho C_p)_{nf}} \left( \frac{\partial^2 \bar{T}}{\partial \bar{x}^2} + \frac{\partial^2 \bar{T}}{\partial \bar{y}^2} \right). \quad (3.2.4)$$

With the associated boundary conditions for rectangular cavity are stated as,

Temperature at lower and upper walls

$$\begin{cases} \bar{T} = T_h, & \text{at } 0.0 \leq \bar{x} \leq \frac{7l}{10}, \bar{y}=0.0. \\ \bar{T} = T_h, & \text{at } \frac{13l}{10} \leq \bar{x} \leq \frac{20l}{10}, \bar{y} = l. \end{cases} \quad (3.2.5)$$

$$\begin{cases} \frac{\partial \bar{T}}{\partial n} = 0, & \text{at } \frac{7l}{10} \leq \bar{x} \leq \frac{20l}{10}, \bar{y}=0.0. \\ \frac{\partial \bar{T}}{\partial n} = 0, & \text{at } 0.0 \leq \bar{x} \leq \frac{13l}{10}, \bar{y} = l. \end{cases} \quad (3.2.6)$$

Temperature at left and right walls

$$\bar{T} = T_C. \quad (3.2.7)$$

Temperature at the inner rods

$$\begin{cases} \bar{T} = T_h, & \text{at } \bar{x} = \frac{7l}{10} + \lambda \sin\left(\frac{\omega\pi\bar{y}}{l}\right), 0.0 \leq \bar{y} \leq \frac{5l}{10}. \\ \bar{T} = T_h, & \text{at } \bar{x} = \frac{13l}{10} + \lambda \sin\left(\frac{\omega\pi\bar{y}}{l}\right), \frac{5l}{10} \leq \bar{y} \leq l. \end{cases} \quad (3.2.8)$$

Velocity at all boundaries

$$\bar{u} = \bar{v} = 0. \quad (3.2.9)$$

Here  $(\bar{u}, \bar{v})$  are  $x$  and  $y$  components of velocity of the fluid,  $\bar{T}$  denotes the temperature,  $\rho_{nf}$  is the effective density of nanofluid,  $\nu_{nf}$  is the kinematic viscosities of

nanofluid,  $\left( (\rho\beta)_{nf}, (\rho C_p)_{nf} \right)$  represents thermal expansion coefficient and heat capacitance of nanofluid, whereas, the thermal conductivity of nanofluid is given by  $k_{nf}$ , while,  $T_h$  and  $T_C$  stand for temperature at heated and cold boundaries,  $\lambda$  and  $\omega$  denote the amplitude and wavelength of the inner wavy heated rods. According to Koo–Kleinstreuer-Li [56,57] and Maxwell [56] the thermal conductivity and dynamic viscosity are given as.

$$k_{nf} = k_{static} + k_{Brownian},$$

$k_{static}$  was defined by Maxwell which is stated as

$$k_{static} = k_f \left( 1 + \frac{3 \left( \frac{k_s}{k_f} - 1 \right) \phi}{\left( \frac{k_s}{k_f} + 2 \right) - \left( \frac{k_s}{k_f} - 1 \right) \phi} \right),$$

where the dynamic part is given by

$$k_{Brownian} = 5 \times 10^4 \phi (\rho C_p)_f \sqrt{\frac{K_b T_0}{\rho_s D_s}} f(T_0, \phi).$$

Here,  $K_b (= 1.38 \times 10^{-23})$ ,  $T_0 (= \frac{1}{2}(T_h - T_C))$ ,  $D_s$  symbolize Boltzmann constant, the average temperature and diameter of nanoparticles. The viscosity due to Brownian motion is defined as

$$\mu_{nf} = \mu_{static} + \mu_{Brownian} = \frac{\mu_f}{(1 - \phi)^{2.5}} + \frac{k_{Brownian} \mu_f}{k_f \text{Pr}}.$$

The other thermodynamic properties are given by [73]

$$\begin{aligned} \rho_{nf} &= (1 - \phi)\rho_f + \phi\rho_s, \\ (\rho C_p)_{nf} &= (1 - \phi)(\rho C_p)_f + \phi(\rho C_p)_s, \\ (\rho\beta)_{nf} &= (1 - \phi)(\rho\beta)_f + \phi(\rho\beta)_s. \end{aligned} \tag{3.2.10}$$

Introducing the following dimensional variables [74, 75].

$$\begin{aligned} X &= \frac{\bar{x}}{l}, \quad Y = \frac{\bar{y}}{l}, \quad U = \frac{\bar{u}l}{\alpha_f}, \quad V = \frac{\bar{v}l}{\alpha_f}, \quad T = \frac{\bar{T} - T_c}{T_h - T_C} \\ P &= \frac{\bar{P}l^2}{\rho_f \alpha_f^2}, \quad \text{Pr} = \frac{\nu_f}{\alpha_f}, \quad Ra = \frac{\beta_f (T_h - T_C) l^3}{\nu_f \alpha_f}. \end{aligned} \tag{3.2.11}$$

Here,  $Pr$  and  $Ra$  define the Prandtl and Rayleigh number. Implementing these variables the governing equations (3.2.2)-(3.2.4) and the boundary conditions (3.2.5) to (3.2.9) reduce to the following dimensionless equations

$$U \frac{\partial U}{\partial X} + V \frac{\partial U}{\partial Y} = -A \frac{\partial P}{\partial X} + B Pr \left( \frac{\partial^2 U}{\partial X^2} + \frac{\partial^2 U}{\partial Y^2} \right), \quad (3.2.12)$$

$$U \frac{\partial V}{\partial X} + V \frac{\partial V}{\partial Y} = -A \frac{\partial P}{\partial Y} + B Pr \left( \frac{\partial^2 V}{\partial X^2} + \frac{\partial^2 V}{\partial Y^2} \right) + C Ra Pr T, \quad (3.2.13)$$

$$U \frac{\partial T}{\partial X} + V \frac{\partial T}{\partial Y} = D \left( \frac{\partial^2 T}{\partial X^2} + \frac{\partial^2 T}{\partial Y^2} \right). \quad (3.2.14)$$

The boundary conditions take the form

$$\left. \begin{array}{l} 0.0 \leq X \leq 0.7, \quad Y = 0.0 \\ 1.3 \leq X \leq 2.0, \quad Y = 1.0 \end{array} \right\} T = 1, \quad (3.2.15)$$

$$\left. \begin{array}{l} 0.7 \leq X \leq 2.0, \quad Y = 0.0 \\ 0.0 \leq X \leq 1.3, \quad Y = 1.0 \end{array} \right\} \frac{\partial T}{\partial n} = 0. \quad (3.2.16)$$

Temperature at left and right walls

$$\left. \begin{array}{l} 0.0 \leq Y \leq 1.0, \quad X = 0.0 \\ 0.0 \leq Y \leq 1.0, \quad X = 2.0 \end{array} \right\} T = 0. \quad (3.2.17)$$

Temperature at the inner rods

$$\left. \begin{array}{l} X = 0.7 + A_m \sin(n_1 \pi Y), \quad 0.0 \leq Y \leq 0.5 \\ X = 1.3 + A_m \sin(n_1 \pi Y), \quad 0.5 \leq Y \leq 1.0 \end{array} \right\} T = 1. \quad (3.2.18)$$

Velocity at all boundaries

$$U = V = 0. \quad (3.2.19)$$

In the above equation the dimensionless physical parameters are defined as

$$A = \frac{\rho_f}{\rho_{nf}}, \quad B = \frac{A}{(1-\phi)^{2.5}} + \frac{A \times k_{Brownian}}{Pr k_f} \quad (3.2.20)$$

$$D = \frac{(\rho C_p)_f}{(\rho C_p)_{nf}} + \frac{(\rho C_p)_f}{(\rho C_p)_{nf}} \left( \frac{k_{static}}{k_f} - 1 \right) + \frac{(\rho C_p)_f}{(\rho C_p)_{nf}} \frac{k_{Brownian}}{k_f} \quad (3.2.21)$$

$$C = A \left( 1 - \phi + \phi \frac{(\rho\beta)_s}{(\rho\beta)_f} \right), \quad A_m = \frac{\lambda}{l}. \quad (3.2.22)$$

In which  $A, B, C, D$  dimensionless thermophysical parameters where  $A_m$  and  $n_1$  are the amplitude ratio and dimensionless wavelength number.

The quantity of physical interest i.e., the heat transfer coefficient in term of local and mean Nusselt number along the heated portions of the cavity are defined as

$$Nu = -\frac{k_{nf}}{k_f} \frac{\partial T}{\partial n} \Big|_{wall} \quad Nu_m = \int_s Nu ds. \quad (3.2.23)$$

Here  $n$  is the normal direction to the heated surface.  $s$  denotes the thermal active boundary and for inner rods  $s$  is length along the wavy rods.

### 3.3 Results and discussion

The natural convection heat transfer inside a rectangular cavity filled with CuO-water nanofluid is analyzed here. The cavity is partially heated at lower left (0.0-0.7) and upper right (1.3 – 2.0). The flow and heat transfer characteristics are affected by two wavy rods at position (0.7, 0.0) on the lower wall and at position (1.3, 1.0) on the upper wall. The simulation is carried out for the influences of emerging physical parameters on the heat transfer rate, temperature, and velocity distribution. The flow field results for different ranges of  $Ra$  ( $10^4 - 10^6$ ),  $\phi$  (0.0 – 0.2),  $A_m$  (0.05 – 0.2) and  $n$  (0 – 20) are reported as:

The influences of Rayleigh number on the flow field and heat transfer rate along the outer heated length and inner wavy rods are portrayed in figures 3.3(a – d). Figure 3.3(a) depicts the variations in heat transfer rate with respect to horizontal mean position along the outer heated surface (upper and lower) of the cavity. It is noticed that local Nusselt number posses maximum values for increasing  $Ra$ . Moreover, figure 3.3(a) illustrates that at lower heated length, the behavior of the heat transfer rate is increasing for  $Ra = 10^4$  to  $10^6$  while, along the upper length it depicts lower values. The Nusselt number at the inner wavy heated rods for various  $Ra$  is presented in figure



3.3(b). A wavy behavior of the heat transfer rate can be observed from line graphs. Enhancement of heat transfer rate in a wavy pattern for higher Ra is evident from the figure. Since augmenting Rayleigh number the buoyancy force becomes stronger and heat transfer takes place through convection. The alterations in temperature distribution along the horizontal mean position are presented in figure 3.3(c). This figure depicts that along the mean position from cold toward the lower heated rods the temperature has maximum values and start declines from the upper heated rod to the right cold surface. Further, from the figure, it can be noticed that the thermal boundary condition satisfies, i.e., the temperature is approaching 1. The vertical velocity along the horizontal mean position enhances from (0.0 – 0.7) and tends to decrease from (0.7 – 2.0) as evident from figure 3.3(d). Moreover, the figure clarifies that velocity converges to zero at all solid boundaries. The variations in heat transfer rate, temperature and velocity profile at different nanoparticles volume fraction are presented in figures 3.4(a–d). The Nusselt number at outer heated length is exhibited in figure 3.4(a). It is observed heat transfer rate along the horizontal central line from (0.0-0.7) rises with respect to the addition of nanoparticles. On the other hand, from (1.3-2.0) Nusselt number gives minimum values as the volume fraction of nanoparticles augments. Figure 3.4(b) depicts the heat transfer rate at the inner wavy heated rods. Clearly, the figure illustrates that heat transfer propagates in a wavy pattern. Also, it can be noted that Nusselt number maximize by adding nanoparticles. Since the presence of nanoparticles provokes the effective viscosity and thermal conductivity of nanoparticles. Higher thermal conductivity corresponds to the maximum heat transfer rate while higher viscosity implies minimum heat transfer. Hence, we have from figure 3.4(a), 3.4(b) the effect of thermal conductivity is dominant over dynamic viscosity thus the net heat transfer rate escalates by the addition of nanoparticles. Figure 3.4(c) demonstrate the changes in temperature profile along the horizontal mean position. It is evident from the figure that between the mean position (0.0–0.7)

temperature decline while it rises between (1.3 – 2.0) as  $\phi$  augments. The variations in velocity distribution with  $\phi$  are presented in figure 3.4(d). The velocity field along the horizontal mean position gives maximum values from 0.0 to 0.7 and least values between 0.7 to 2.0. Figures 3.5(a – d) are considered for the combined effects of wavelength number  $n$  and nanoparticles volume fraction  $\phi$  on heat transfer rate at inner heated rods. It is observed from figure 3.5(a) that for  $n = 0$  (flat rods) the heat transfer rate enhances as the volume fraction of nanoparticles increase. The heat transfer rate along the heated rods at  $n$  ( $= 5, 10, 20$ ) is presented in figure 3.5(b) to 3.5(d), overall, at various corrugation, the Nusselt number escalates in a wavy manner for different  $\phi$ . As the corrugation of the heated rods increases the flow and thermal distribution adjacent to the rods varies. This gives rise in heat transfer rate through convection in the cavity. Thus, as the nanoparticles volume fraction increases the effect of corrugation on heat transfer is more prominent. The effects of varying amplitude  $A_m$  of the inner wavy rods on the flow and thermal fields at distinct Rayleigh number  $Ra$  are illustrated in figures 3.6 and 3.7. The isotherms are presented in figures 3.6 (a – f) for  $0.05 \leq A_m \leq 0.2$  at  $Ra = 10^4$  and  $10^6$ . Figure 3.6 reveals that as the amplitude of the inner wavy rods maximizes the thermal contours intensify. This impact is more stronger for larger Rayleigh number  $Ra$  i.e., at  $Ra = 10^6$ . Since, as  $A_m$  increases the space near the heated rods reduces for the circulations adjacent to the rods. Thus, the temperature contours are pushed towards the cold and adiabatic boundaries. This predicts that the temperature of the cavity overall rises. which is evident from the figures 3.6(a – f) as the anticlockwise orientations getting stronger as both the amplitude and Rayleigh number vary. This confirms that heat transfer in the cavity is controlled by convection. On the other hand, the influences of different amplitude and Rayleigh number on streamlines pattern are depicted in figure 3.7(a – f). The flow pattern in symmetric clockwise and anticlockwise can be observed. As the amplitude  $A_m$  increases the anticlockwise circulation getting

stronger while the clockwise orientations tend to decrease. Moreover, at smaller values of  $Ra$ , the streamline contours are weaker and its value is up to  $(-60)$ . While at  $Ra = 10^6$  the contours are stronger having values up to  $(100)$ .

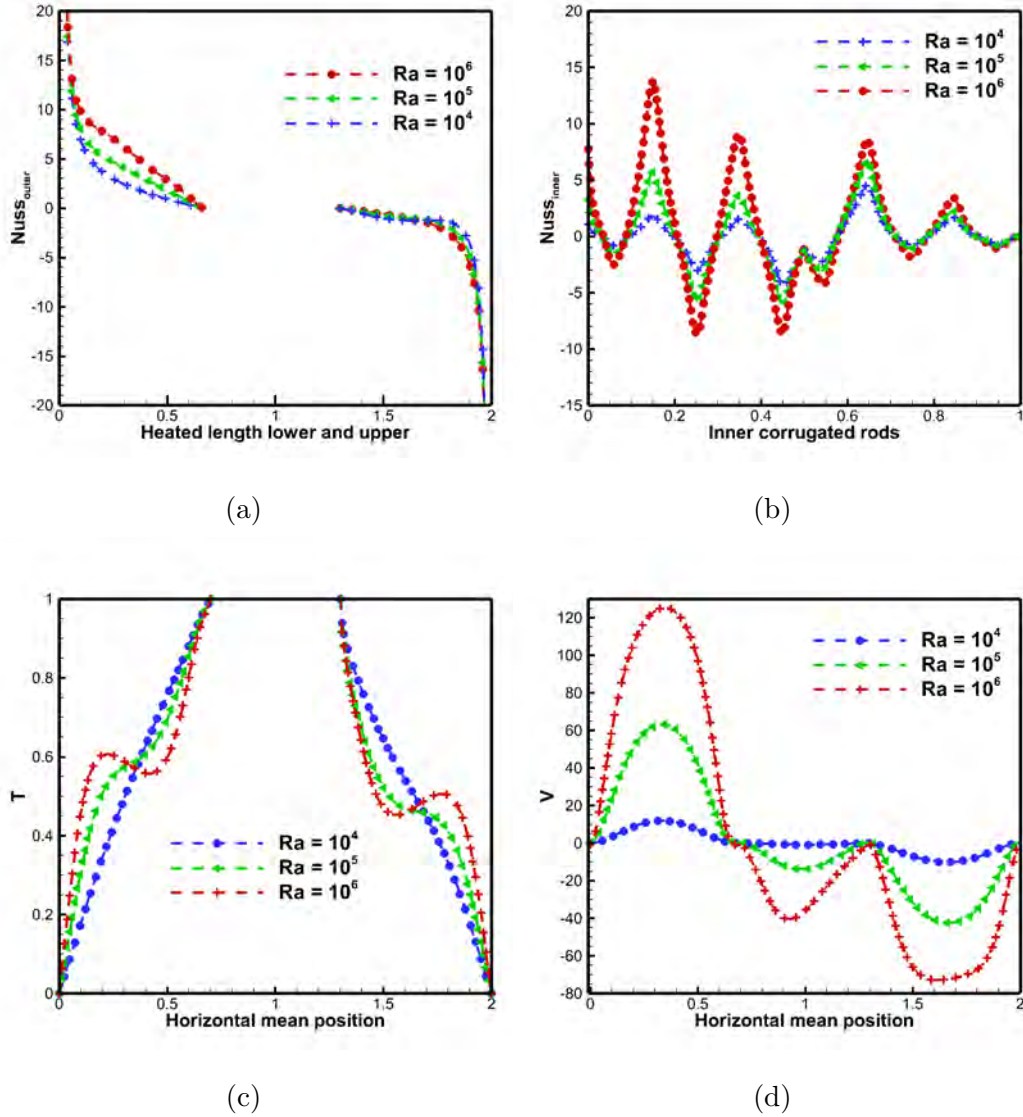
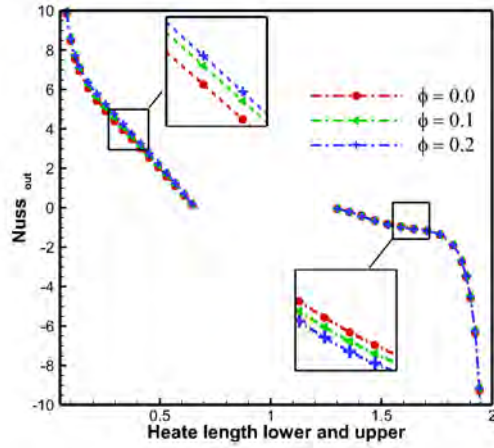
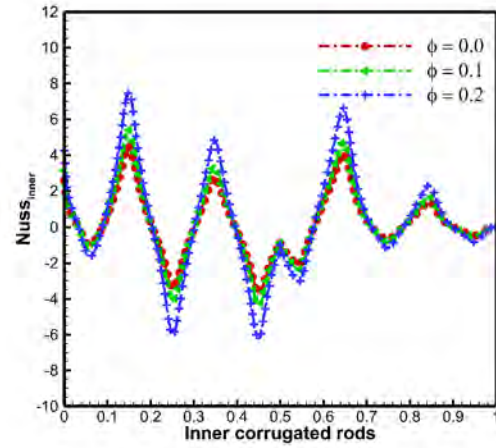


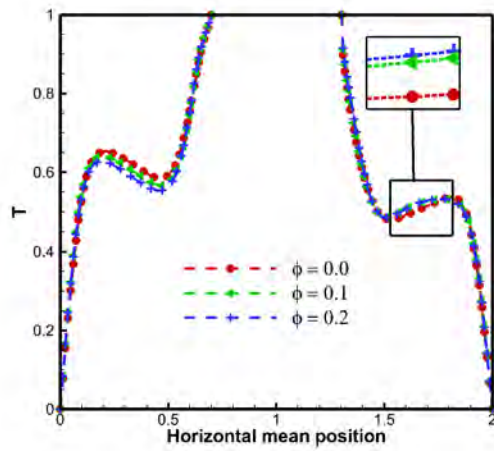
Figure 3.3: Impact of  $Ra$  on Nusselt number (a) along the outer heated length (b) along the inner corrugated heated rods and (c) temperature (d) Velocity profile along horizontal mean position.



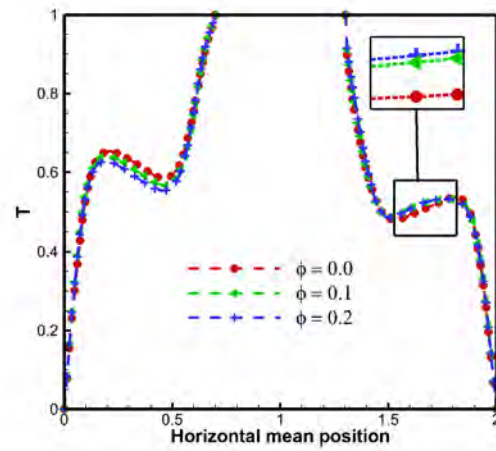
(a)



(b)

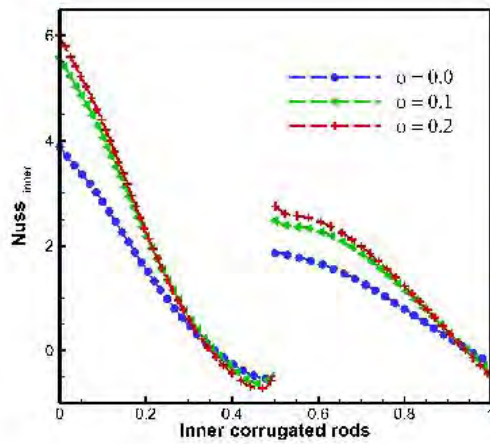


(c)

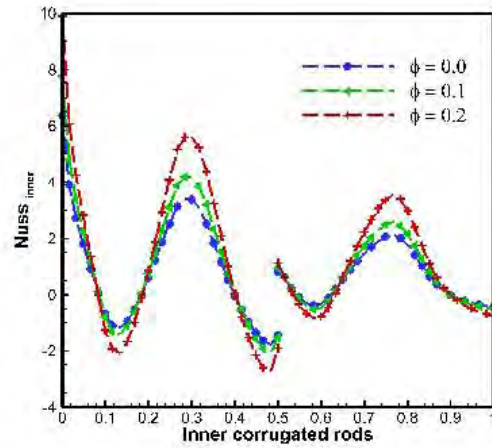


(d)

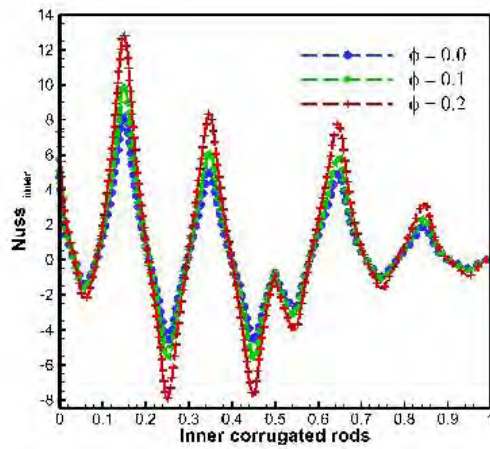
Figure 3.4: Impact of  $\phi$  on Nusselt number (a) along the outer heated length (b) along the inner corrugated heated rods and (c) temperature (d) Velocity profile along horizontal mean position.



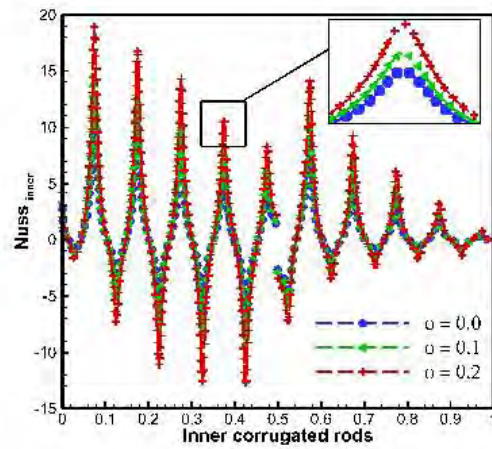
(a)



(b)

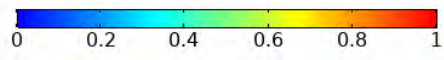
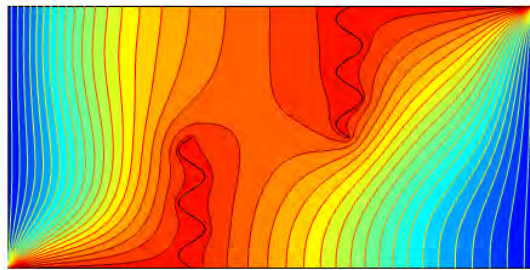


(c)

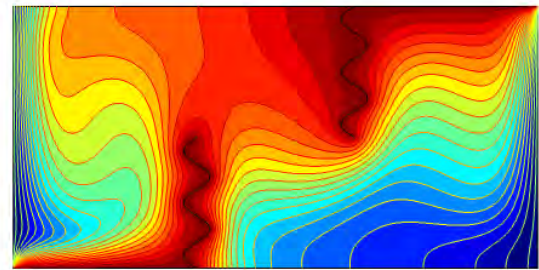


(d)

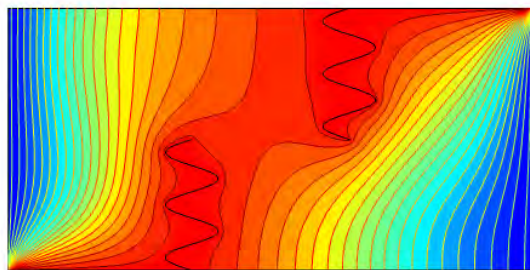
Figure 3.5: Variations in Nusselt number for various  $\phi$  at (a)  $n_1 = 0$  (b)  $n_1 = 10$  (c)  $n_1 = 20$  (d)  $n_1 = 30$ .



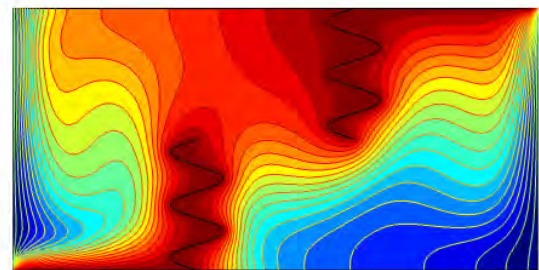
(a)



(b)



(c)



(d)

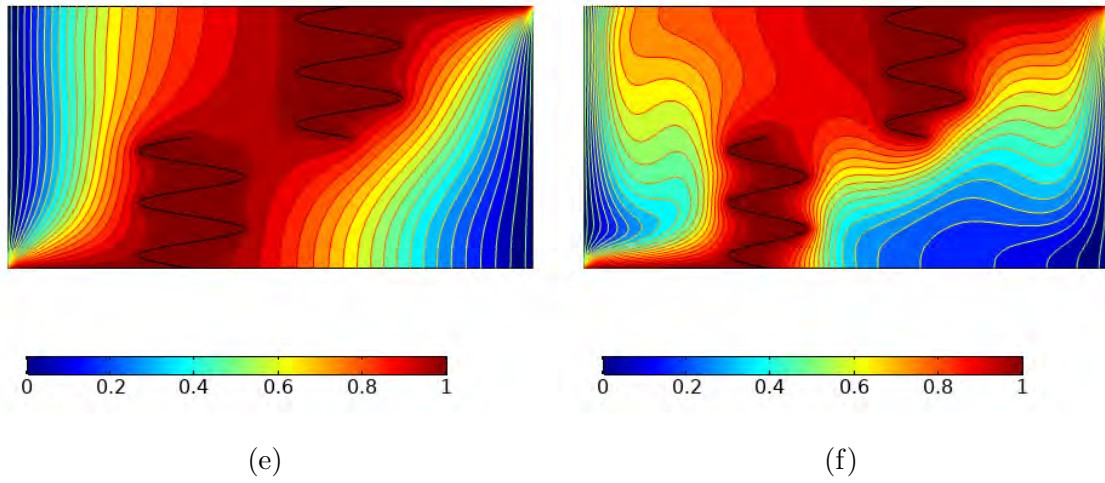
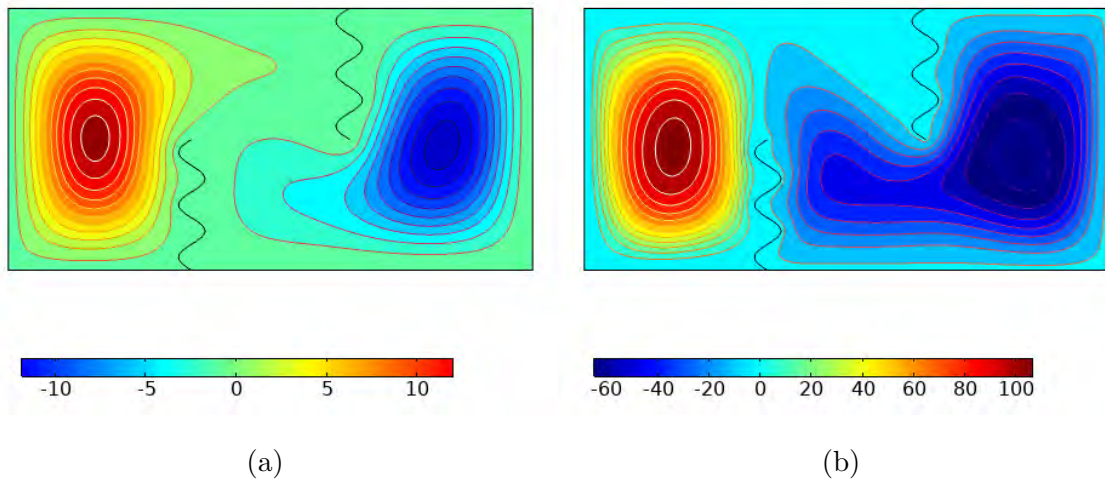


Figure 3.6: Isotherms for different  $Ra = 10^4$  (left),  $Ra = 10^6$  (right) and at various amplitude  $A_m = 0.05$  ((a), (b)),  $A_m = 0.1$  ((c), (d)) and  $A_m = 0.2$  ((e), (f)).



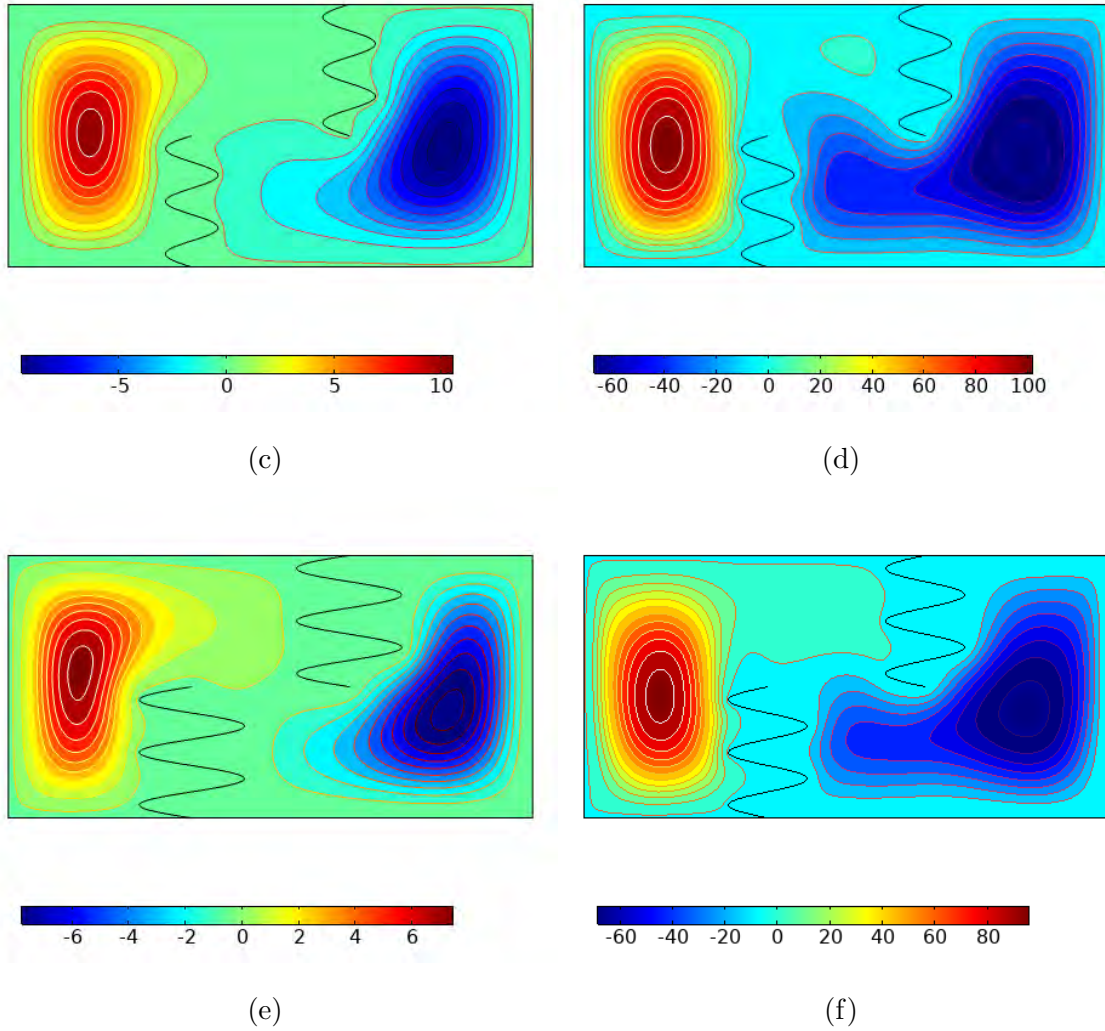


Figure 3.7: Streamlines at various amplitude  $A_m = 0.05$  ((a), (b)),  $A_m = 0.1$  ((c), (d)) and  $A_m = 0.2$  ((e), (f)) for different  $Ra = 10^4$  (left),  $Ra = 10^6$  (right).

### 3.4 Concluding remarks

In this article, we have studied three specific nanoparticles (alumina ( $Al_2O_3$ ), titania ( $TiO_2$ ) and copper ( $Cu$ )) with base fluid taken to be water. We have got the following remarks from our study.



- ✠ For nanofluid with copper nanoparticles the velocity components show increasing behavior as the volume fraction of nanoparticles (copper) rises along both the saddle and nodal points.
- ✠ The temperature also improves for the CU-water nanofluid with the enhancement in volume fraction ( $\phi$ ) of nanoparticles along stagnation points
- ✠ It is noted that for all three nanoparticles, alumina and copper have the smaller and higher velocities components.
- ✠ The effect of a magnetic parameter ( $\beta$ ) on skin friction coefficients has been examined, and it is noted that shear stresses at the surface reduce as ( $\beta$ ) rise.
- ✠ We have observed that for considered nanoparticles the skin friction coefficients, and local Nusselt number expand for the increasing values of  $\phi$ .
- ✠ We have remarked that there is fall in wall shear stresses and rate of heat transfer when velocity and thermal slip parameters raise.
- ✠ The surface shear stresses and heat transfer rate have higher values for copper-water nanofluid as compared to Titania and alumina-water nanofluids.

# Chapter 4

## Finite element analysis of convective nanofluid equipped in enclosure having both inlet and outlet zones

### 4.1 Introduction

The scientific investigations relevant to convection in porous media have considerably increased due to its demand for energy, the requirement to establish efficient for waste management in nuclear technologies, in chemical industries separation process, transpiration cooling, housing insulation, in catalytic reactors, winding technology in high power density machine and various other sectors demands the interest in porous media convective heat transport. In the fast decades researchers acquire different approaches to control (enhance) the convective heat transportation. Thus, in that important direction the investigation in this chapter is to discuss the thermal convective transport propagation in porous medium with nanoparticles. The simulation

owns the mathematical and computational analysis of the forced and free convection in a square shape enclosure with inlet/outlet opening. The left boundary is uniformly heated while the right wall is taken cold. The force flow constraint is implemented on the openings ports and the remaining portions are kept adiabatic. To be more specific the mixed convection transportation in the regime persists because of thermal difference in-between the heated source and cold inflow of fluid. For possible insight, the physical model is translated in terms of the differential systems. To report solution the finite element method has been adopted. The quantities of interest include the flow and heat transportation individualities. The output of computational scheme towards various controlling parameters are offered by means of both the contour maps and line graphs.

## 4.2 Geometrical description and basic equations

The physical model contains a partially open and heated square cavity having sides length  $L$  filled with  $CuO$ -water nanofluid saturated in porous medium. The lower left and upper right walls of the cavity possess an inlet and outlet portions with length  $d$ , whereas, the other portions are insulated. The left wall of the cavity is uniformly heated with temperature  $T_h$  and the right wall is kept at constant low temperature  $T_C$ . Figure 4.1 illustrates the geometry of physical setup while figure 4.2 presents the triangular mesh distribution for the computational domain.

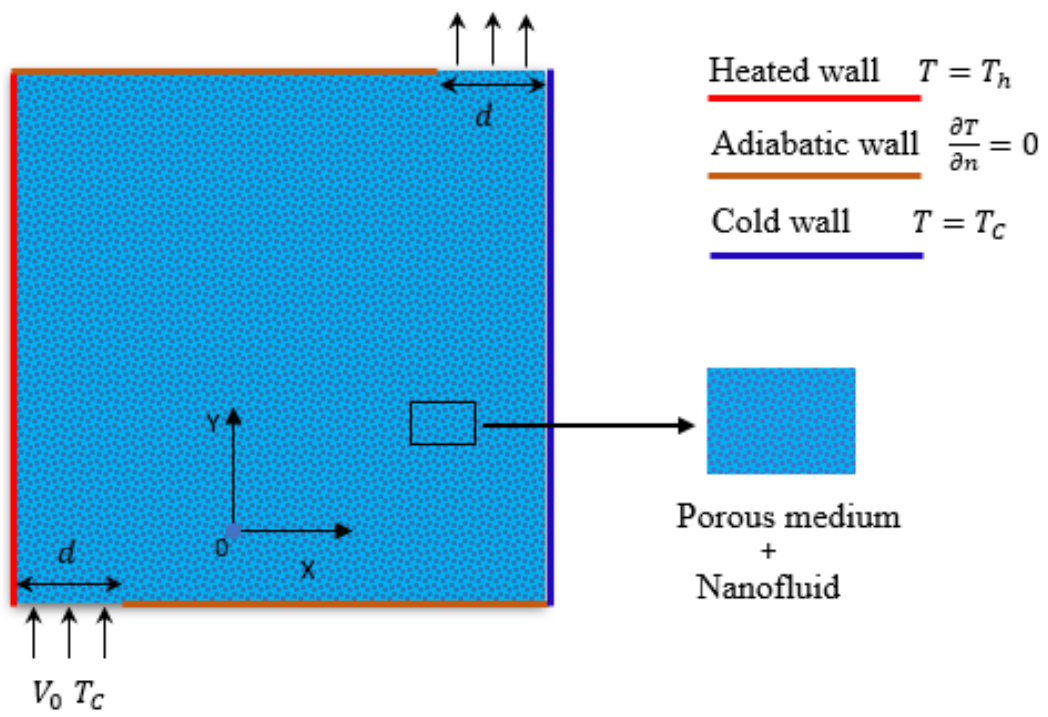


Figure 4.1: Schematic sketch of physical model

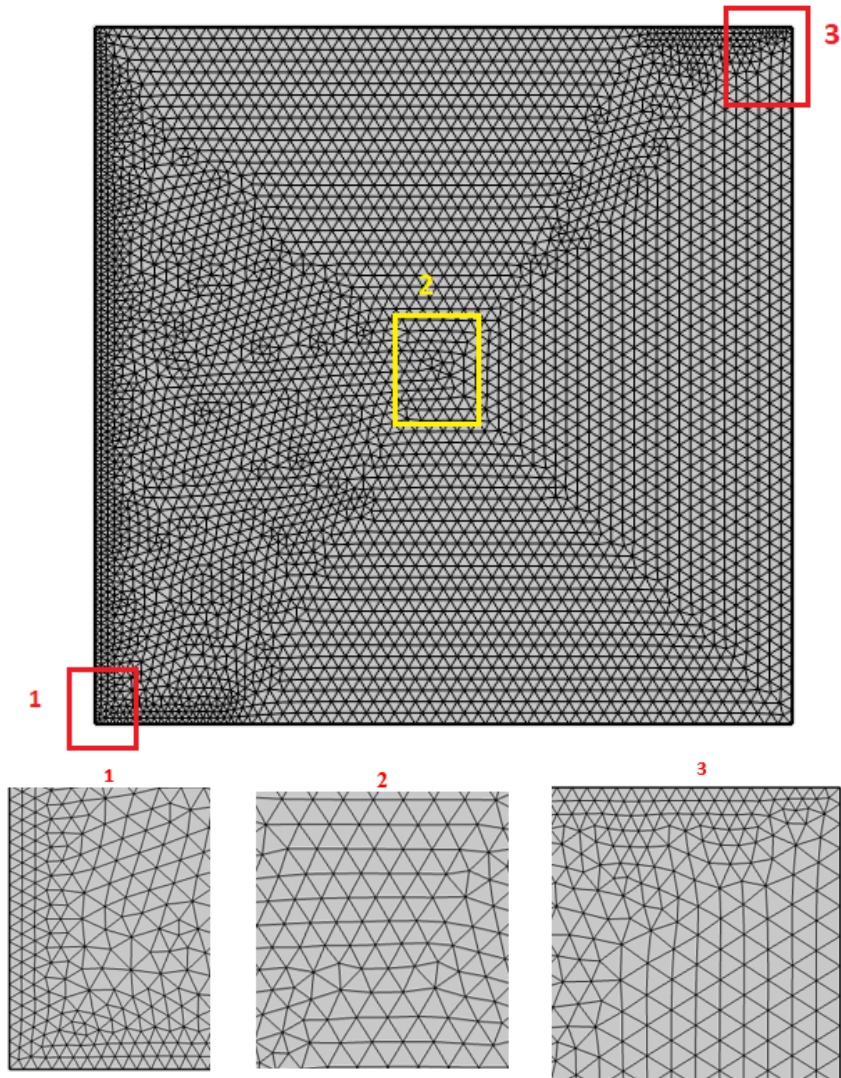


Figure 4.2: Mesh distribution of the computational domain.

A force flow constraints are considered on the top and bottom wall opening applying the suction and injection phenomena. Buoyancy effect is maintained because of temperature difference between a laminar vertical cold stream of inflow with constant velocity  $V_0$  and wall temperature  $T_h$ . The thermo-physical properties for acting nanofluid are presented in table 2.1. Isotropic porosity is assumed with permeability  $K_p$  and under the Boussinesq approximation the conservation equations can be expressed as

$$\frac{\partial v}{\partial y} + \frac{\partial u}{\partial x} = 0, \quad (4.2.1)$$

$$v \frac{\partial u}{\partial y} + u \frac{\partial u}{\partial x} = -\frac{1}{\rho_{nf}} \frac{\partial p}{\partial x} + \nu_{nf} \left( \frac{\partial^2 u}{\partial y^2} + \frac{\partial^2 u}{\partial x^2} \right) - \frac{\nu_{nf}}{K_p} u, \quad (4.2.2)$$

$$v \frac{\partial v}{\partial y} + u \frac{\partial v}{\partial x} = -\frac{1}{\rho_{nf}} \frac{\partial p}{\partial y} + \nu_{nf} \left( \frac{\partial^2 v}{\partial y^2} + \frac{\partial^2 v}{\partial x^2} \right) + g(T - T_C) \frac{(\rho\beta)_{nf}}{\rho_{nf}} - \frac{\nu_{nf}}{K_p} v, \quad (4.2.3)$$

$$v \frac{\partial T}{\partial y} + u \frac{\partial T}{\partial x} = \frac{k_{nf}}{(\rho C_p)_{nf}} \left( \frac{\partial^2 T}{\partial y^2} + \frac{\partial^2 T}{\partial x^2} \right). \quad (4.2.4)$$

Here  $(u, v)$  are the velocity profiles along  $(x, y)$  directions,  $T$  denotes the temperature, and  $(\rho_{nf}, \nu_{nf})$  indicate effective density and kinematic viscosity of nanofluid. The thermal expansion coefficient and heat capacitance of nanofluid are denoted by  $(\rho\beta)_{nf}$ , and  $(\rho C_p)_{nf}$ . Whereas, the nanofluid thermal conductivity is given by  $k_{nf}$ , while,  $(T_h, T_C)$  signify the temperature distribution at heated and cold wall.

For the thermo-physical properties the Koo–Kleinstreuer–Li model [57,58] is followed as

$$k_{nf} = k_{static} + k_{Brownian}, \quad (4.2.5)$$

$k_{static}$  is defined by Maxwell [56] as

$$k_{static} = k_f \left( 1 + \frac{3 \left( \frac{k_s}{k_f} - 1 \right) \phi}{\left( \frac{k_s}{k_f} + 2 \right) - \left( \frac{k_s}{k_f} - 1 \right) \phi} \right), \quad (4.2.6)$$

where the dynamic part is given by

$$k_{Brownian} = 5 \times 10^4 \phi (\rho C_p)_f \sqrt{\frac{K_b T_0}{\rho_s D_s}} f(T_0, \phi). \quad (4.2.7)$$

Here, ( $K_b = 1.38 \times 10^{-23}$  ,  $T_0 = 0.5(T_h - T_C)$ ) specify the Boltzmann constant and average temperature while  $D_s$  is the diameter of nanoparticles.

Whereas, the viscosity in terms of static and Brownian motion is expressed as

$$\mu_{nf} = \mu_{static} + \mu_{Brownian} = \frac{\mu_f}{(1 - \phi)^{2.5}} + \frac{k_{Brownian} \mu_f}{k_f \text{Pr}}.$$

To obtain dimensionless system one can use the following variables [76, 77].

$$\begin{aligned} X &= \frac{x}{L}, & Y &= \frac{y}{L}, & U &= \frac{u}{V_0}, & V &= \frac{v}{V_0}, \\ P &= \frac{P}{\rho_f V_0^2}, & \theta &= \frac{T - T_c}{T_h - T_C}. \end{aligned} \quad (4.2.8)$$

By use of above dimensionless variables (4.2.8) the conservation equations (4.2.1)-(4.2.4) in reduced non-dimensional take the form

$$\frac{\partial V}{\partial Y} + \frac{\partial U}{\partial X} = 0, \quad (4.2.9)$$

$$V \frac{\partial U}{\partial Y} + U \frac{\partial U}{\partial X} = -A(\phi) \frac{\partial P}{\partial X} + \left( \frac{\partial^2 U}{\partial Y^2} + \frac{\partial^2 U}{\partial X^2} \right) \frac{B(\phi)}{Re} - U \frac{B(\phi)}{Re Da}, \quad (4.2.10)$$

$$\begin{aligned} V \frac{\partial V}{\partial Y} + U \frac{\partial V}{\partial X} &= -A(\phi) \frac{\partial P}{\partial Y} + \left( \frac{\partial^2 V}{\partial Y^2} + \frac{\partial^2 V}{\partial X^2} \right) \frac{B(\phi)}{Re} + \\ &\theta C(\phi) \frac{Gr}{Re^2} - V \frac{B(\phi)}{Re Da}, \end{aligned} \quad (4.2.11)$$

$$V \frac{\partial \theta}{\partial Y} + U \frac{\partial \theta}{\partial X} = \frac{D(\phi)}{\text{Pr} Re} \left( \frac{\partial^2 \theta}{\partial Y^2} + \frac{\partial^2 \theta}{\partial X^2} \right). \quad (4.2.12)$$

with the related dimensionless boundary conditions as follow

$$\begin{aligned} \theta &= 0, \\ U &= 0, \quad V = 1 \end{aligned} \quad \text{at } Y = 0, \quad 0 \leq X \leq b, \quad (4.2.13)$$

$$\begin{aligned} \theta_Y &= 0, \\ U &= 0, \quad V_Y = 0 \end{aligned} \quad \text{at } Y = 1, \quad 1 - b \leq X \leq 1, \quad (4.2.14)$$

$$\begin{aligned} \theta_Y &= 0 \text{ at } Y = 1, \quad 0 \leq X \leq 1 - b, \\ \theta_Y &= 0 \text{ at } Y = 0, \quad b \leq X \leq 1, \end{aligned} \quad (4.2.15)$$

$$\begin{aligned}
\theta &= 1 \text{ at } 0 \leq Y \leq 1, \quad X = 0, \\
\theta &= 0 \text{ at } 0 \leq Y \leq 1, \quad X = 1, \\
U &= V = 0. \quad \text{for all boundaries}
\end{aligned} \tag{4.2.16}$$

In which the subscript  $Y$  denotes the partial derivative and the other non-dimensional variables are given by

$$\begin{aligned}
A(\phi) &= \frac{\rho_f}{\rho_{nf}}, \quad B(\phi) = \frac{A(\phi)}{(1-\phi)^{2.5}} + \frac{A(\phi) \times k_{Brownian}}{Pr k_f} \\
D(\phi) &= \frac{(\rho C_p)_f}{(\rho C_p)_{nf}} + \frac{(\rho C_p)_f}{(\rho C_p)_{nf}} \left( \frac{k_{static}}{k_f} - 1 \right) + \frac{(\rho C_p)_f}{(\rho C_p)_{nf}} \frac{k_{Brownian}}{k_f} \\
C(\phi) &= A(\phi) \left( 1 - \phi + \phi \frac{(\rho\beta)_s}{(\rho\beta)_f} \right).
\end{aligned} \tag{4.2.17}$$

The heat transfer at the heated portion can be expressed as

$$Nu = -\frac{k_{nf}}{k_f} \frac{\partial \theta}{\partial X} \Big|_{X=0} \quad Nu_m = \int_0^1 Nu dY. \tag{4.2.18}$$

### 4.3 Results and discussion

In this chapter, the simulation is performed for mixed convection of copper-oxide ( $CuO$ ) water nanofluid equipped in a partially opened and heated enclosure. Finite element analysis has been carried out for the simulations of governing equations against different physical parameters. Considering the following range of parameters: Nanoparticles concentration ( $\phi = 0.0 - 0.05$ ), Grashof number ( $Gr = 10^3 - 10^5$ ), Reynolds Number ( $Re = 1 - 10^2$ ), Darcy number ( $Da = 10^{-4} - 10^{-2}$ ) and Prandtl number ( $Pr = 6.8$ ). Particular efforts were focused on the influence of emerging parameters on flow field (Streamlines and velocity profiles) and thermal distributions (Isotherms, temperature field and Nusselt number) presented in figures 4.3-4.11. The contour maps for isotherms of  $CuO$ -water nanoliquid at various  $Gr$  (Grashof number) and different  $\phi$  (Solid volume fraction) are shown in figures 4.3(a - f). Figure

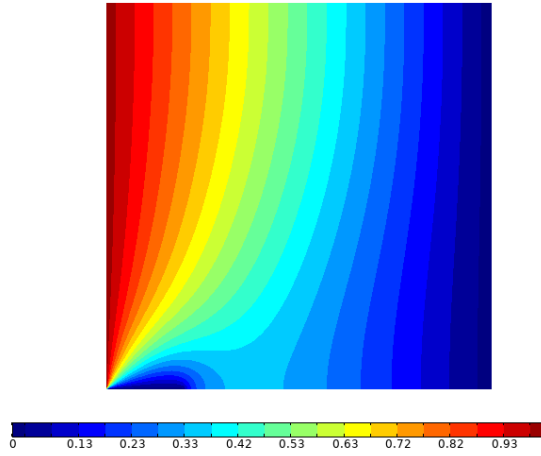


4.3 depicts that at low volume fraction  $\phi$  the convective mode of heat transfer is dominant and the thermal contours are spread uniformly in the cavity. As  $\phi$  enhances fluid become more concentrated and the convection effect switches to conduction heat transfer. It is clear from the isotherms which are crowded close to the left heated wall and equally dispersed in the core of enclosure, as evident in figures 4.3( $a - f$ ) at  $Gr = 10^3$  (on the left side) and  $Gr = 10^4$  (on the right side). On the other hand, the addition of nanopowder leads to the base fluid more viscous. Thus, the flow motion inside the cavity reduces. Likewise, the higher solid volume fraction corresponds to maximum thermal conductivity of nanofluid owing to this reason the convection effect reduces resulting maximum thermal distribution in cavity. Figures 4.4( $a - c$ ) clarifies this explanation. The Nusselt number along the heated vertical portion and temperature profile along horizontal mean position shown in line graphs figures 4.4( $a - b$ ) are enhanced. Similarly, the velocity profile along the horizontal mean position of denser nanofluid decreases at various increasing values of  $\phi$  as given in figure 4.4( $c$ ). The flow inside the enclosure is induced by both the buoyancy effect and inertial forces. The buoyancy forces characterizes by the Grashof number  $Gr$  while the Reynolds number control the force flow condition. The impact of distinct values of  $Gr$  on the thermal distribution and flow field is portrays in contour maps figures 4.5( $a - f$ ) and line graphs figures 4.5( $a - c$ ). In figures 4.5( $a, b$ ) at low Grashof number the force flow through the inlet predominant the natural convection. Thus, the stream function flow pattern depict clearly that a stream of cold fluid enters the cavity and move toward the outlet. The buoyancy effect is weaker in this case due to the strong inertial forces as revealed in figure 4.5( $a$ ). Due to weak buoyancy forces the conductive heat transfer take place and the isotherms contour spread uniformly in the cavity for heated wall toward the cooled wall as illustrated in figure 4.5( $b$ ). At higher  $Gr$  the buoyancy effect gets stronger which leads to maximum free convective transportation from left heated toward right cooled wall. It is worth mentioning that

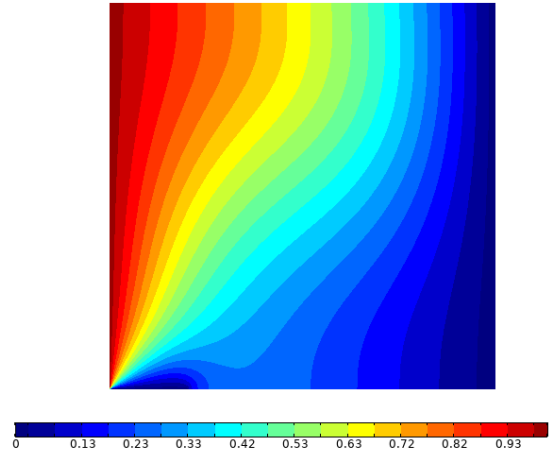
the strength of streamlines and isotherms curves is increased in the middle of the cavity, see figures 4.5(*c – f*) for reference. Impact of Grashof number on Nusselt number along the vertical heat length is presented in figure 4.6(*a*). Higher  $Gr$  implies greater buoyancy forces which suppress the force cold inflow resulting stronger free-convective heat transportation. Thus heat transfer rate has higher values at maximum  $Gr$ . Furthermore, the thermal boundary increases as  $y$  approaches 1 the Nusselt number reduces in that case, as illustrated in figure 4.6(*a*). As the higher values of  $Gr$  possess weaker thermal boundary layer thickness effect, thus, along the horizontal mean position the temperature perturbation near the heated wall diminish as demonstrated in figure 4.6(*b*). The fluid velocity field at  $y = 0.5$  it is observed that the vertical velocity profile is maximum near the heated source wall whereas, it tends to decrease in the middle and in the vicinity of cooler left wall as shown in figure 4.6(*c*). Influence of Darcy number on thermal distribution (isotherms, Nusselt number and temperature profile) and on flow field (streamlines and velocity distribution) is presented in figures 4.7(*a – f*) and figures 4.8(*a – c*). From figures 4.7(*a – f*) it is exhibited that porous medium permeability decrease for smaller  $Da$ . Thus, in the case  $Da = 10^{-2}$  (figures 4.7(*a, b*)) the solid matrix resistance is minimum as a result the fluid motion and the the effect of heated wall is dominant inside the entire enclosure. Further decrease of  $Da$  to  $10^{-3}$ ,  $10^{-4}$  the resistance of solid matrix to the flowing particles getting stronger. Consequently, the resistance to flow field enhances resulting decrease in the streamline distributions and isotherm in the entire cavity, as presented in figures 4.7(*c – f*). likewise, in figures 4.8(*a – c*) it is obvious that the behavior of Nusselt number (figure 4.7(*a*)) is maximum at  $Da = 10^{-2}$  and minimum at  $Da = 10^{-4}$ . figures 4.8(*b, c*) also depict that at lower  $Da$  the velocity and temperature profiles at  $y = 0.5$  (horizontal mean position) have lesser values. The effect of heated wall length on isotherms is demonstrated in figures 4.9(*a – d*) and on Nusselt number and thermal profile is illustrated in figures 4.10(*a, b*). The

isotherms contour show that at smaller heated source length i.e., at  $Lt = 0.25$  the convective heat transfer is less and the penetration of cold nanofluid throughout the cavity is stronger due to dominant inertial forces. As,  $Lt$  increases up to 1 the buoyancy effects control the inertial forces and suppress the cold passage of nanofluid, strengthening the convective heat transfer across the enclosure, see figures 4.9(*a – d*). Impact of different heated source vertical length on Nusselt number and temperature profile is depicted in figures 4.10(*a, b*). Line graph reveals that smaller heated length ( $Lt = 0.25$ ) possess minimum heat flux in the cavity for instant increase in the heated source length the strength of Nusselt number augments as sketched in figure 4.10(*a*). Likewise, the temperature perturbation also have lesser values at smaller  $Lt$  and maximum magnitude at higher  $Lt$  (See figure 4.10(*b*)). Figures 4.11(*a – f*) depict the influence of Reynolds number on streamlines and isotherms. In this study the Reynolds number characterizes the force flow condition i.e., the strength of inflow of cold nanofluid at injection zone. Another important parameter  $Ri$  (Richardson number) which correlate the forced convection and natural convection. When  $Ri < 1$  the basic mode of flow is force convection while for  $Ri > 1$  the flow is maintained by natural convection. Thus, smaller  $Re$  implies higher  $Ri$  which signifies the buoyancy driven flow dominated the forced inflow convection. From the streamlines distribution it is clear that inside the cavity clockwise and anticlockwise circulations are formed and are almost same, while the isotherm contour maps are mostly parallel indicates that the thermal distribution here resembles conduction heat transfer. It should be noted that a decrease of  $Re$  the force inflow becomes weaker as a result the isotherms in flat near the vertical heated wall (See figures 4.11(*a, b*)). As  $Re$  augments the intensity of injected cold nanofluid enhances which predominate the buoyancy effect. In figure 4.11(*e*) the streamlines distribution inside the cavity shows the stronger force inflow which moves toward the outlet zone and almost occupy the whole cavity. In this force convection dominated mode (i.e.,  $Re = 10^2$  and  $Ri < 1$ ), the isotherms

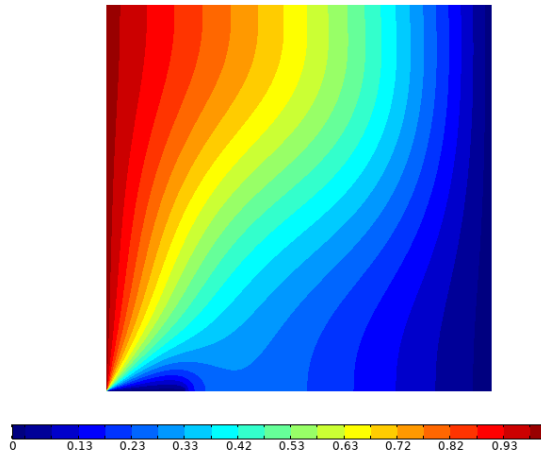
shown in figure 4.11(*f*) are clustered toward the heated vertical wall which depicts a sharp temperature gradient from left towards the right cooler wall. While in the remaining regime of cavity the temperature gradient is minimum because of stronger force inflow.



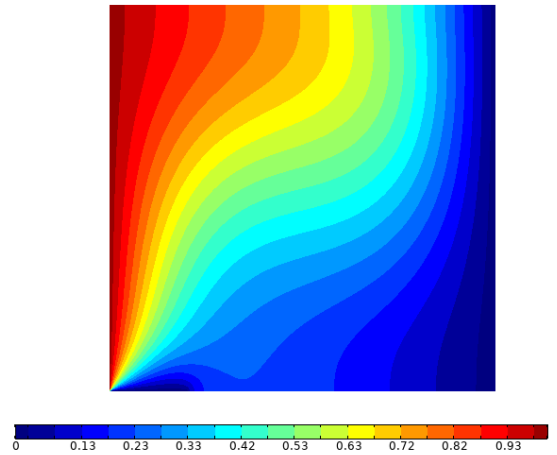
(a)



(b)



(c)



(d)

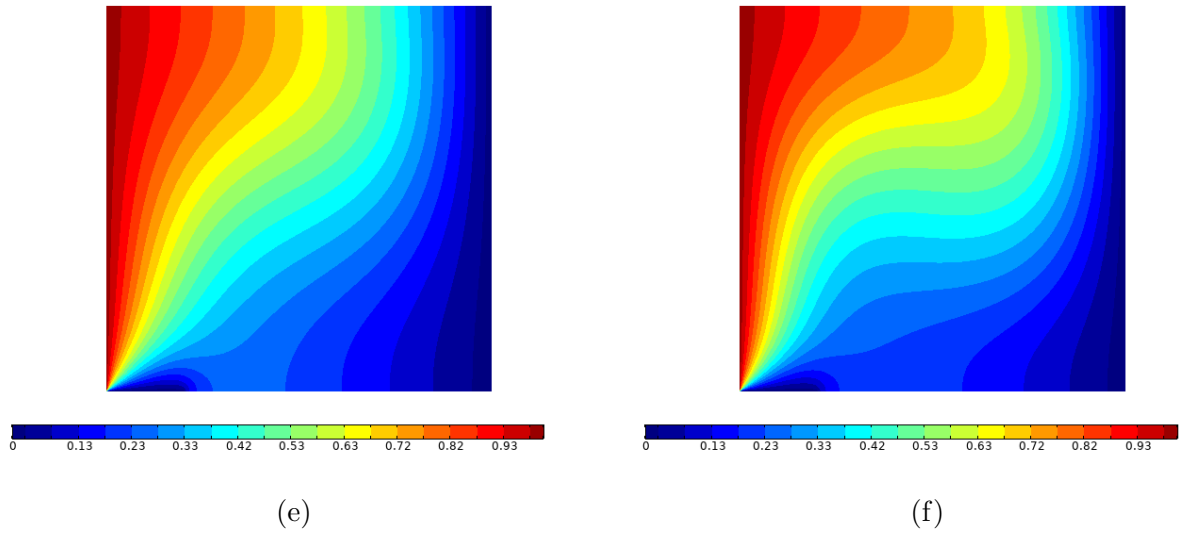
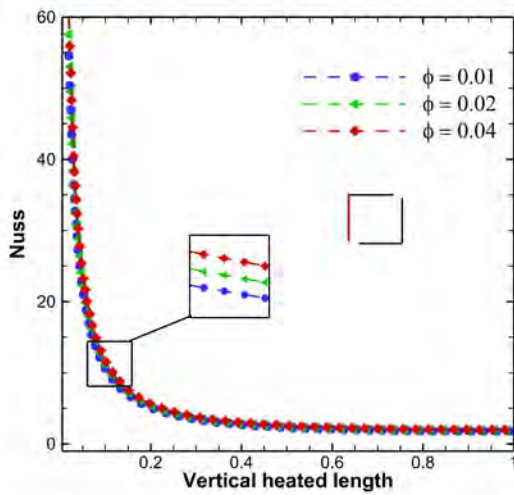
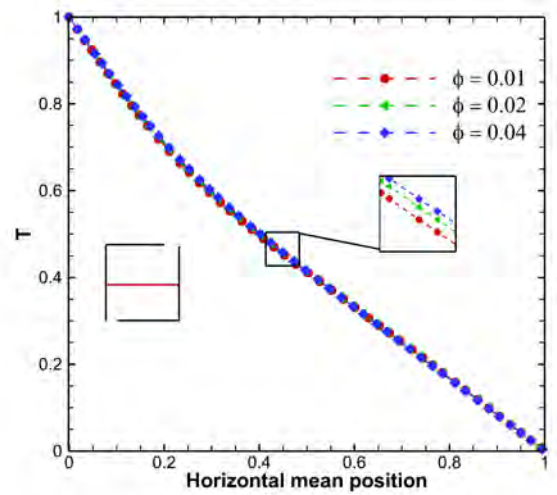


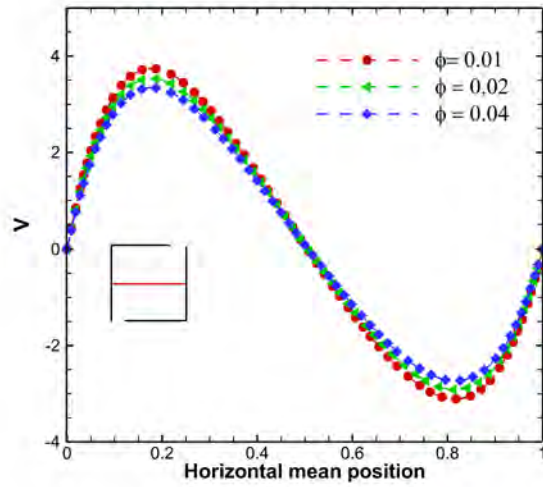
Figure 4.3: Isotherms for various values of  $\phi$  and  $Gr$ . from top to bottom  $\phi = 0.01$  ((a), (b)),  $\phi = 0.02$  ((c), (d)),  $\phi = 0.04$  ((e), (f)) and  $Gr = 10^3$  (left),  $Gr = 10^4$  (right).



(a)

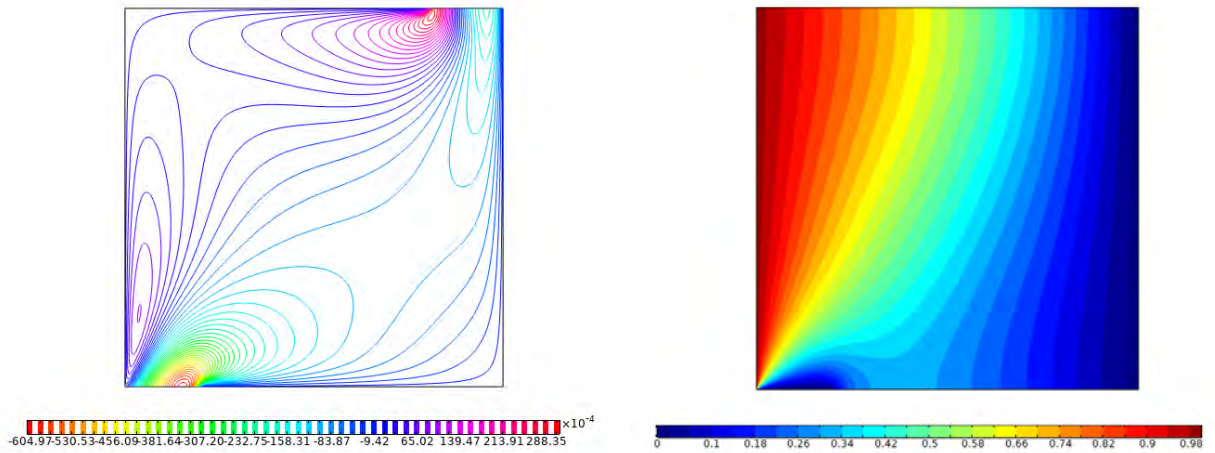


(b)



(c)

Figure 4.4: Impact of  $\phi$  on Nusselt number in (a) and temperature and velocity in (b), (c) along heated length and horizontal mean position



(a)

(b)

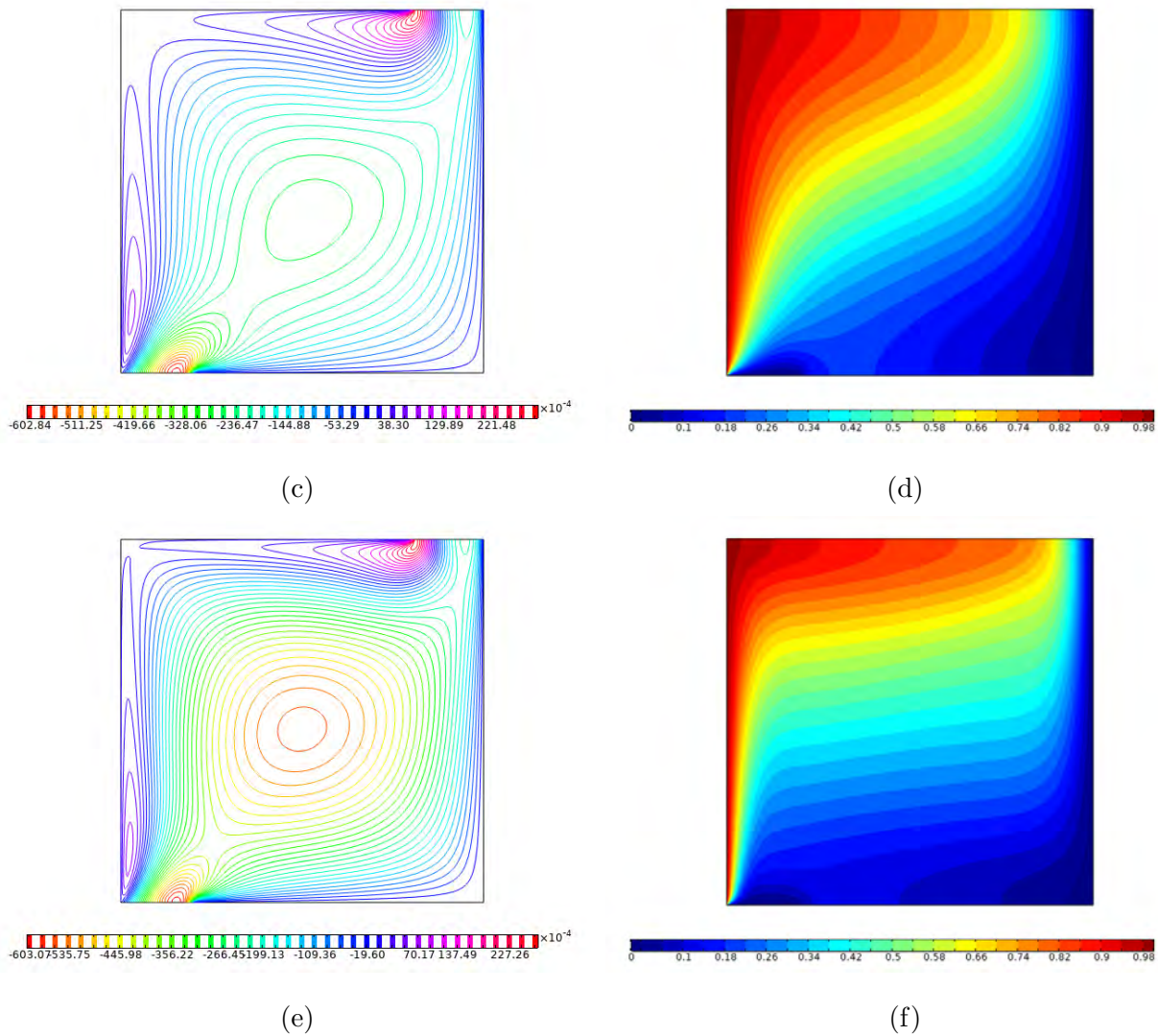
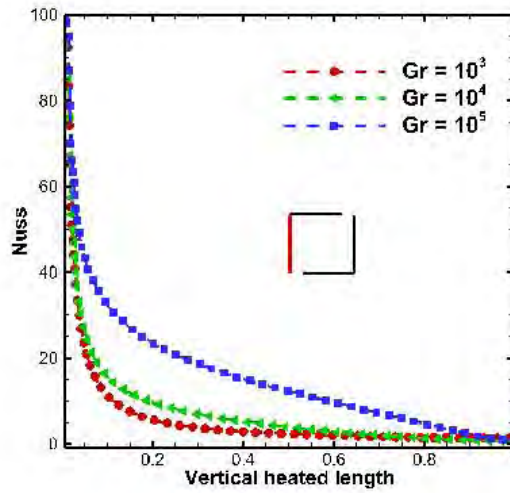
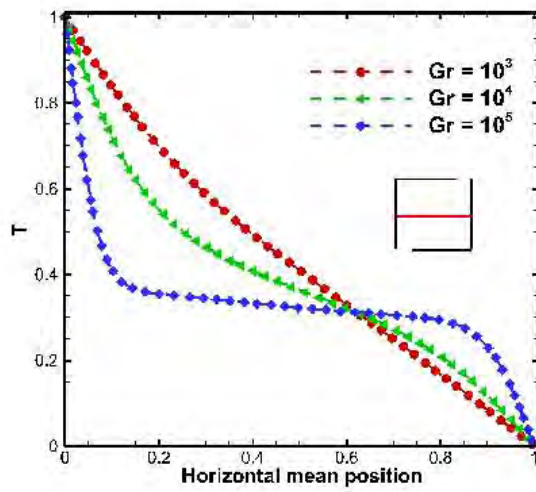


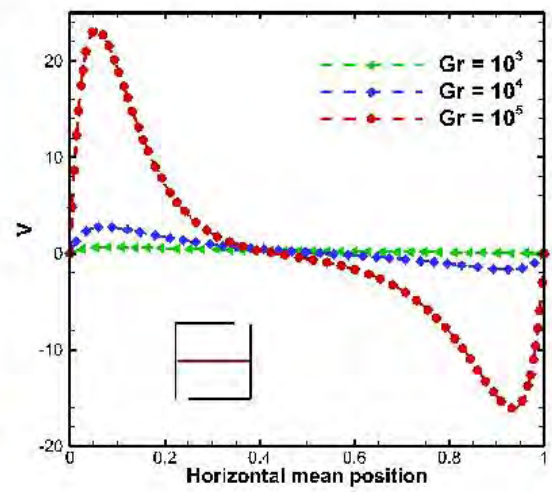
Figure 4.5: Streamlines and temperature contour for various values of  $Gr$ .  $Gr = 10^3$  ((a), (b)),  $Gr = 10^4$  ((c), (d)) and  $Gr = 10^5$  ((e), (f)).



(a)



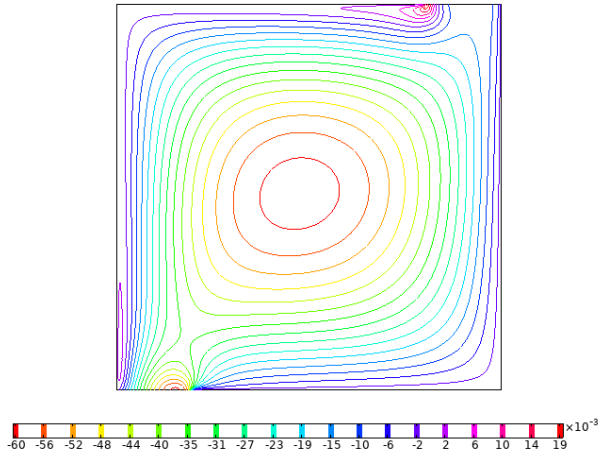
(b)



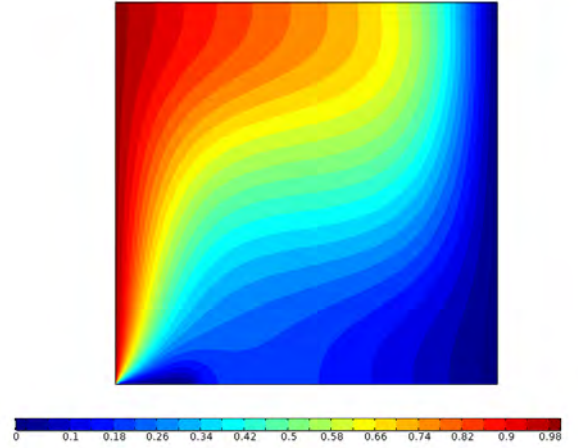
(c)

Figure 4.6: Impact of  $Gr$  on Nusselt number in (a), temperature and velocity in (b), (c) along heated length and horizontal mean position

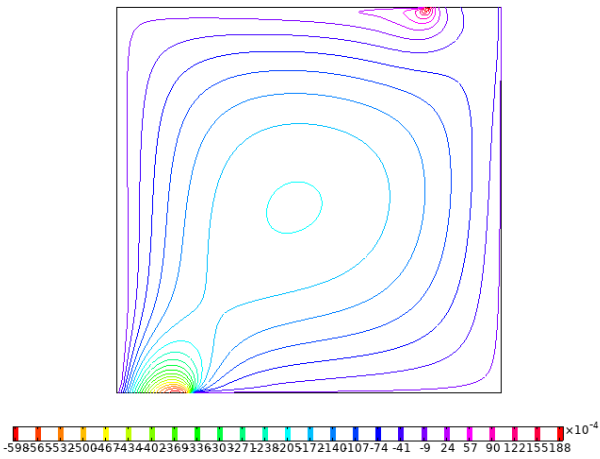




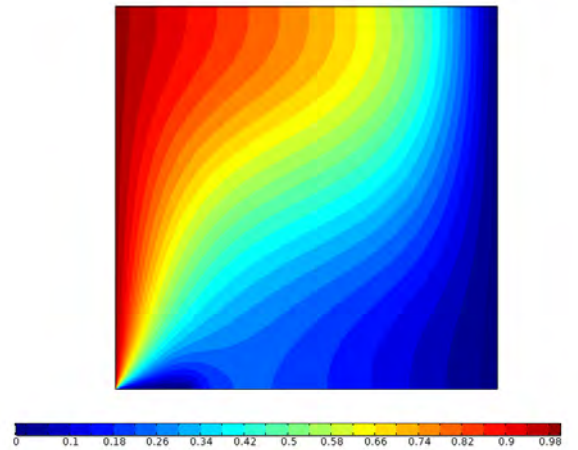
(a)



(b)



(c)



(d)

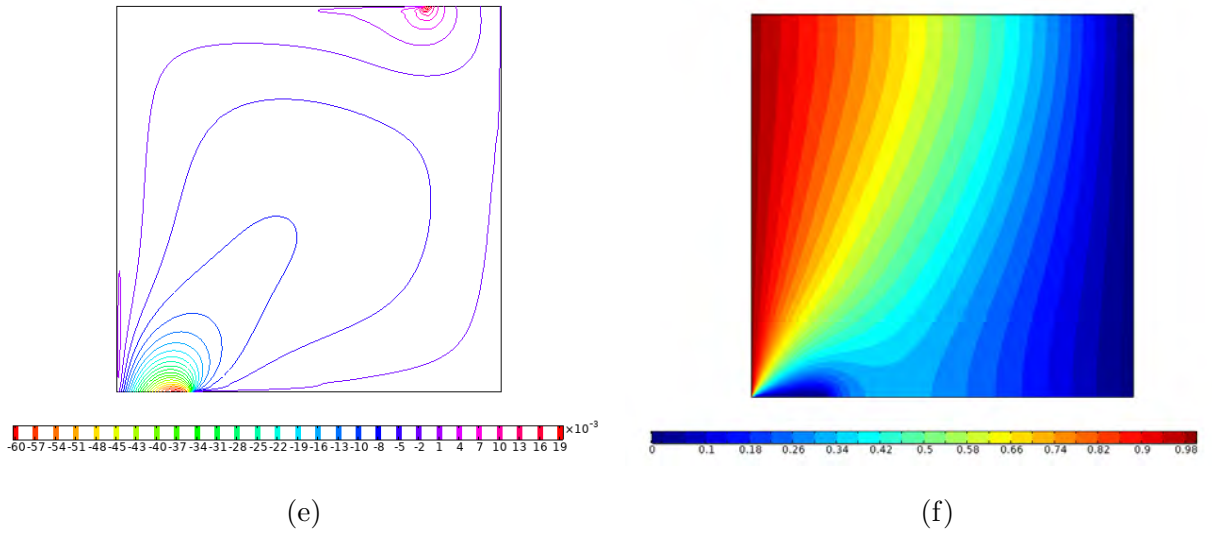
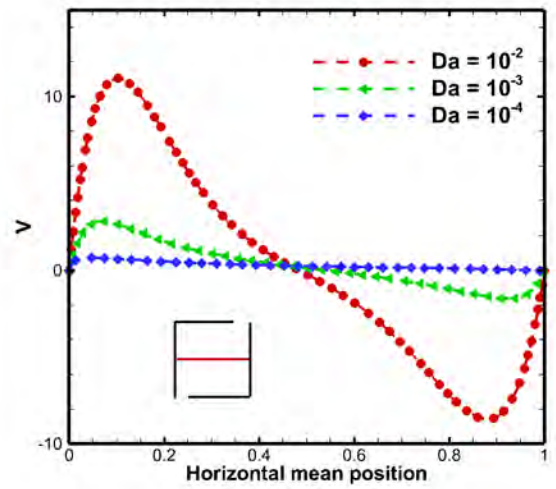
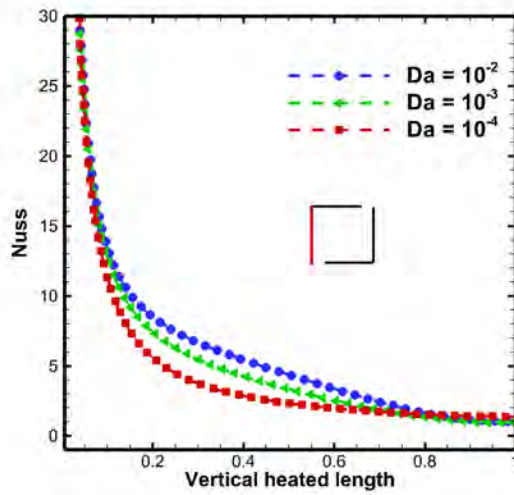
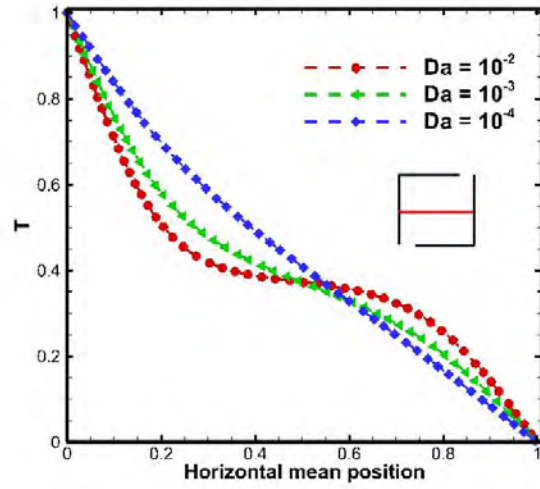


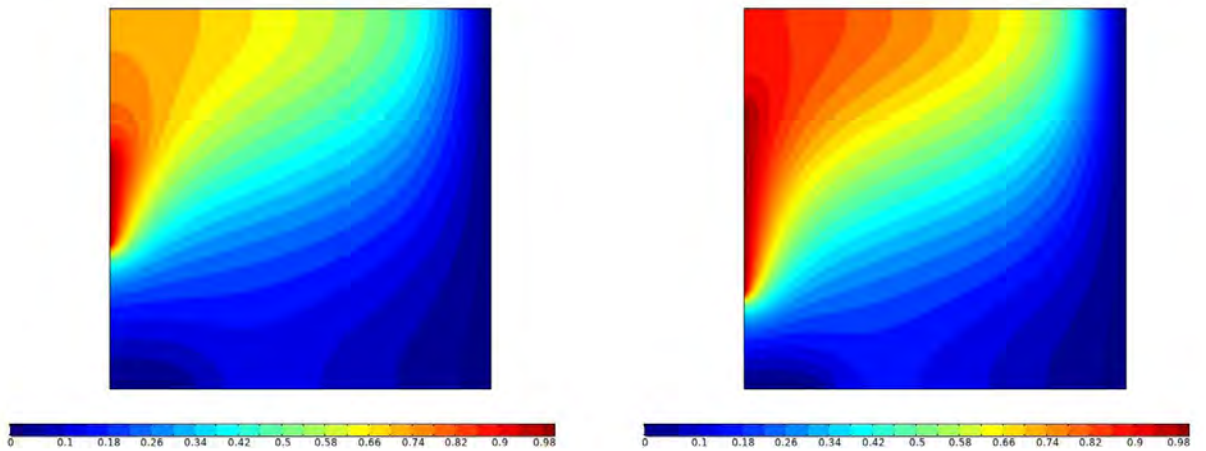
Figure 4.7: Streamlines and isotherms against various Darcy number.  $Da = 10^{-2}$  ((a), (b)),  $Da = 10^{-3}$  ((c), (d)) and  $Da = 10^{-4}$  ((e), (f)).





(c)

Figure 4.8: Influence of  $Da$  on Nusselt number in (a), velocity and temperature in (b), (c) along heated length and horizontal mean position



(a)

(b)

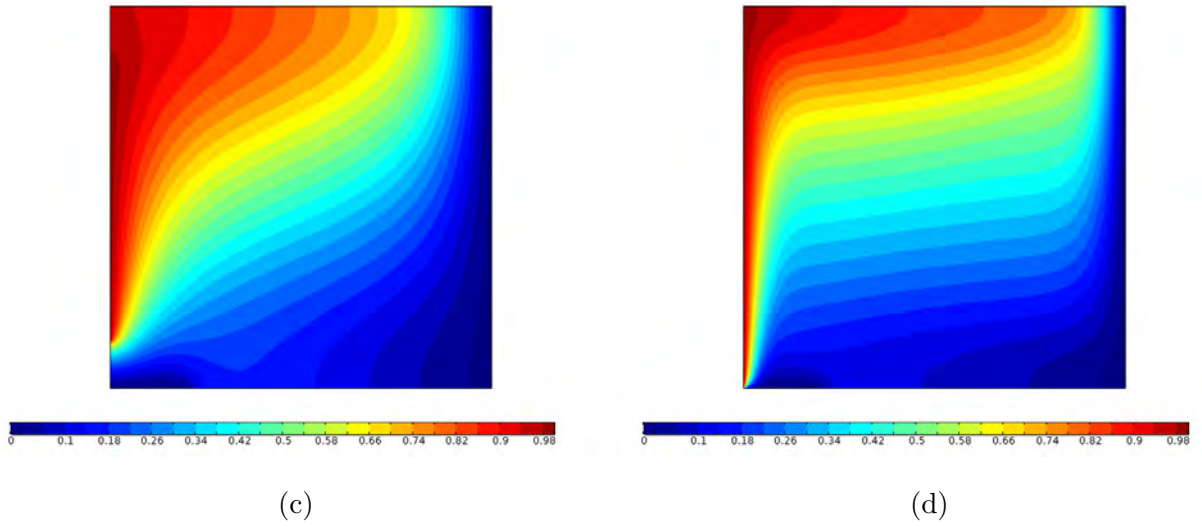


Figure 4.9: Isotherms at distinct heated segments  $Lt$ .  $Lt = 0.25$  (a),  $Lt = 0.50$  (b),  $Lt = 0.75$  (c), and  $Lt = 1.0$  (d).

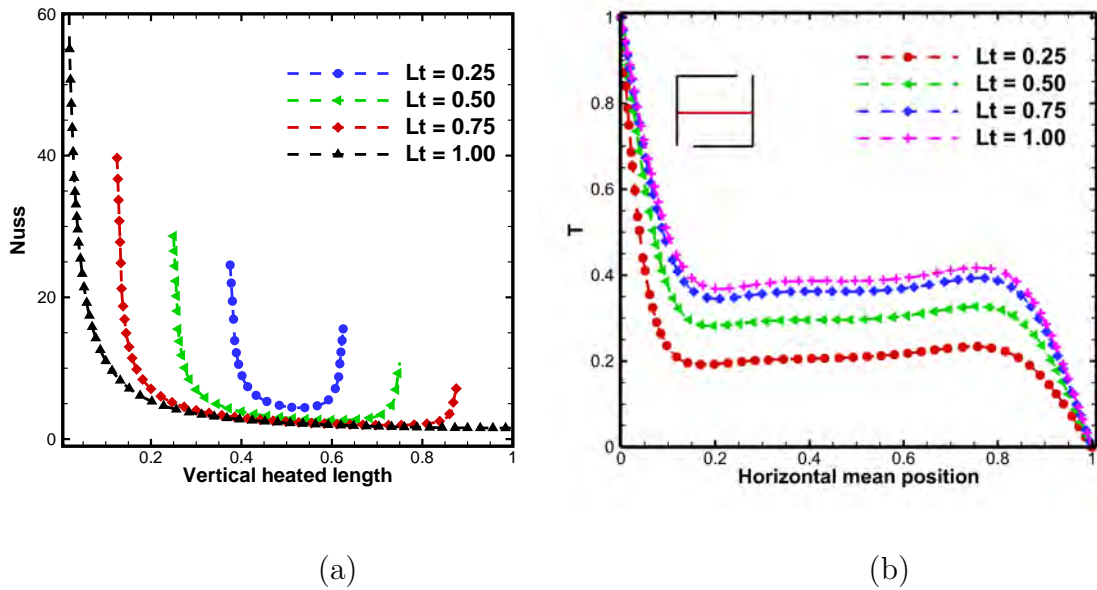
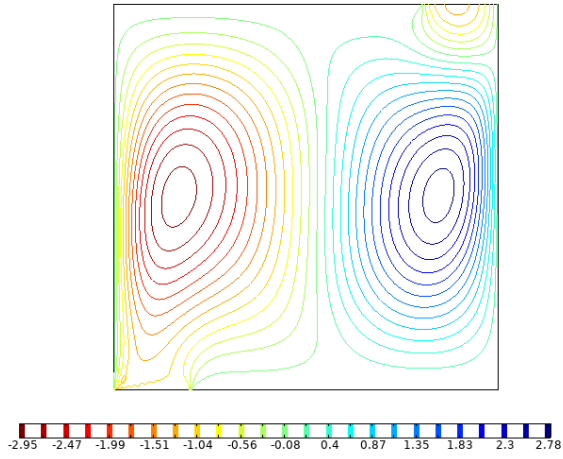
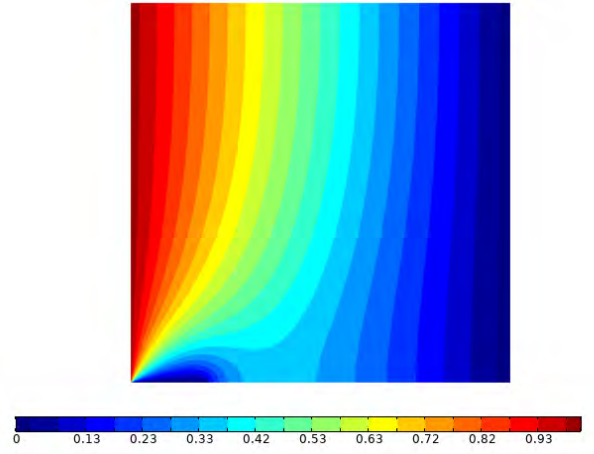


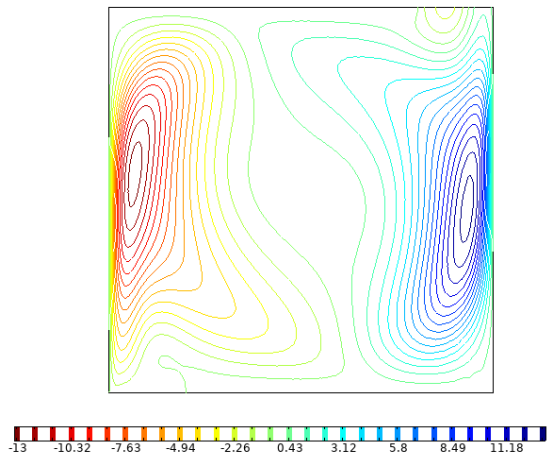
Figure 4.10: Variations in Nusselt number (a) and temperature (b) at various heated portion



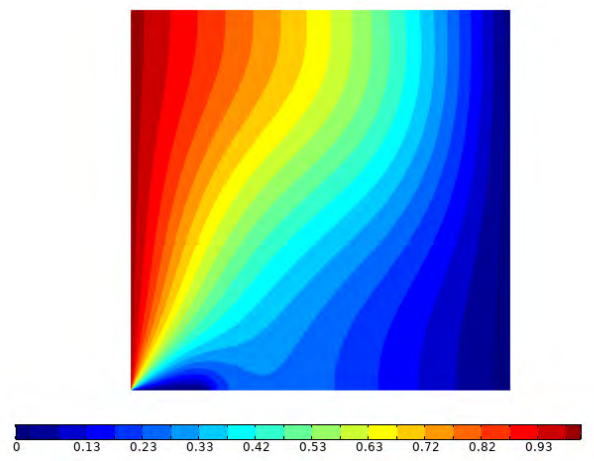
(a)



(b)



(c)



(d)

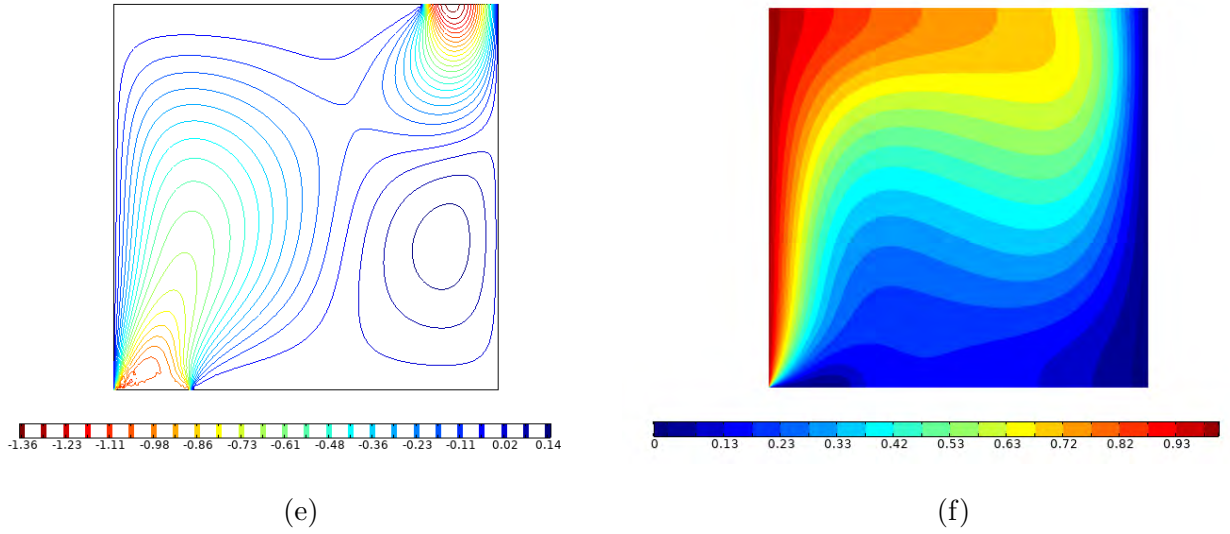


Figure 4.11: Streamline and Isotherms at various  $Re$ . ((a), (b))  $Re = 1$   $Ri = 10^3$ , ((c), (d))  $Re = 10$   $Ri = 10$  and ((e), (f))  $Re = 100$   $Ri = 0.1$ .

## 4.4 Concluding remarks

Simulation is executed for emerging parameters which decide the flow profiles and thermal perturbations inside the enclosure regime. Due to addition of  $\phi$  the primary mode of heat transfer inside the cavity switches from convection to conduction, Nusselt number also enhances against growing  $\phi$ . Streamlines pattern indicate the predominant effect of forced inflow over free convection at lesser  $Gr$ . Higher  $Gr$  corresponds to maximum Nusselt number and velocity profile near the heated wall. Primary circulations in streamlines contour gets stronger at maximum  $Da$  free convection heat transfer mode and velocity field enhances against maximum Darcy number. Raising the vertical heated source length implies stronger thermal distributions and higher Nusselt number suppressing the cold injected nanofluid. At higher  $Re$  (lower  $Ri$ ) the primary streamlines circulation enhances due to increased forced inflow of cold nanofluid. whereas at maximum  $Ri$  (lesser  $Re$ ) the isotherms contour maps depict conduction heat transfer mode.

# Chapter 5

## Simulations of micropolar nanofluid-equipped natural convective driven flow in a cavity

### 5.1 Introduction

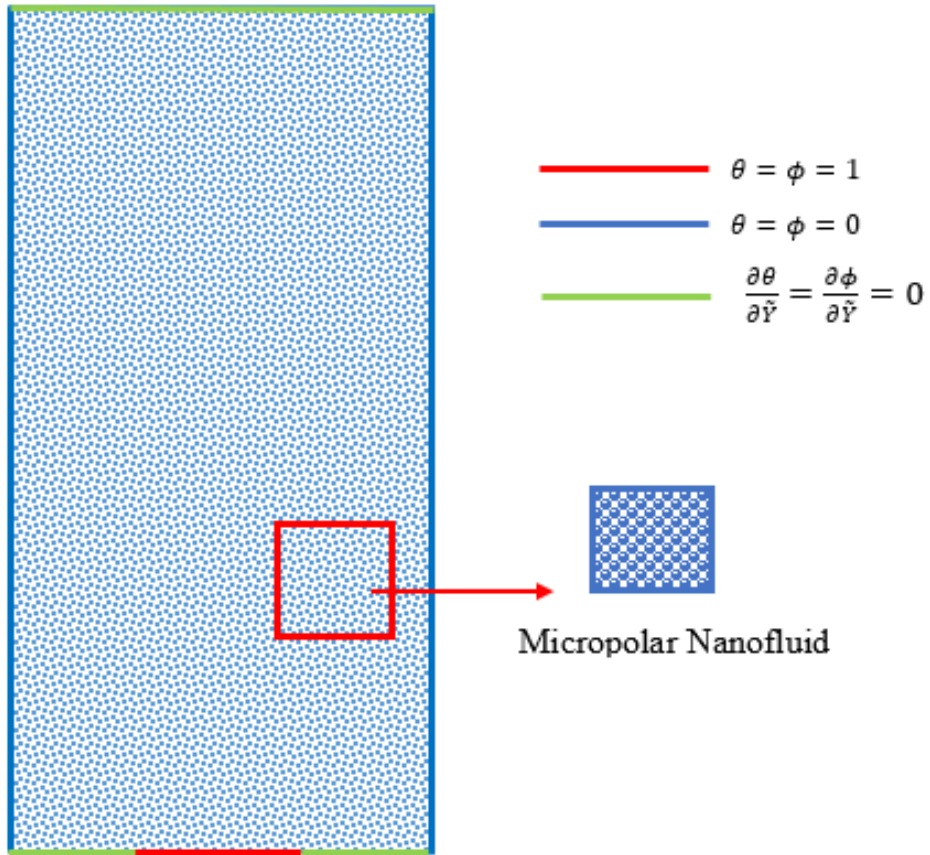
Convection in micropolar fluids finds application in various industrial products, material processing, biomechanics, slurry technology low-concentration suspensions, turbulent shear flows, colloidal suspensions etc. Erigen [43–45] initially suggested microfluidics theory in order to delineate the micro-motions of fluid particles that could not be described by the classical models. The beauty of this model is that it can characterizes various complex rheological fluids like, animal blood, polymers, lubricants, suspension and paints etc. Owing to its plenty of industrial and engineering application numerous researcher have adopted micropolar fluid basic equations to narrate flow problem in various enclosure and cavities. Convection transportation in such complex and important model in presence of nanofluid is the main theme of this chapter. The aim is to focus on the natural convective flow analysis of micropolar

nanofluid fluid in a rectangular vertical container. A heated source is placed in the lower wall to generate the internal flow. In further assumptions the left/right wall are kept cool, while the upper and lower remaining portions are insulated. Free convection prevails in the regime because of thermal difference in-between the lower warmer and upper colder region. Such physical setup owns mathematical framework in-terms of non-linear partial differential equations. The interesting features of the flow along with thermal transportation involve both translational and rotational movement of fluid particles. Performing the simulations towards flow controlling variables the outputs are put together in contour maps and line graphs.

## 5.2 Physical model and basic equations

The physical setup of the flow consists of a two dimensional rectangular shape container of length  $2l$  and width  $l$  filled with micro-polar nanofluid placed vertically in  $x, y$  coordinate system as shown in Fig. 5.1(a). Fig. 5.1(b) illustrates the triangular mesh distribution for the computational domain. The cavity is enclosed by isothermal cooled vertical left (at  $\tilde{x} = 0$ ) and right (at  $\tilde{x} = 1$ ) walls having temperature  $T_c$  and mass concentration  $C_c$  and adiabatic upper wall (at  $\tilde{y} = 2$ ). Including this, a heated source is mounted at the middle of bottom wall ( $P_1 \leq \tilde{x} \leq P_2$ ) of temperature and mass concentration  $T_h$  and  $C_h$  greater than  $T_c$  and  $C_c$  whereas the remaining portions ( $0 \leq \tilde{x} \leq P_1$  &  $P_1 \leq \tilde{x} \leq P_2$ ).





$$U^* = V^* = 0 \text{ On all boundaries}$$

$$N^* = -n \frac{\partial U^*}{\partial \tilde{Y}} \text{ On upper and lower wall}$$

$$N^* = -n \frac{\partial V^*}{\partial \tilde{X}} \text{ On left and right wall}$$

(a)

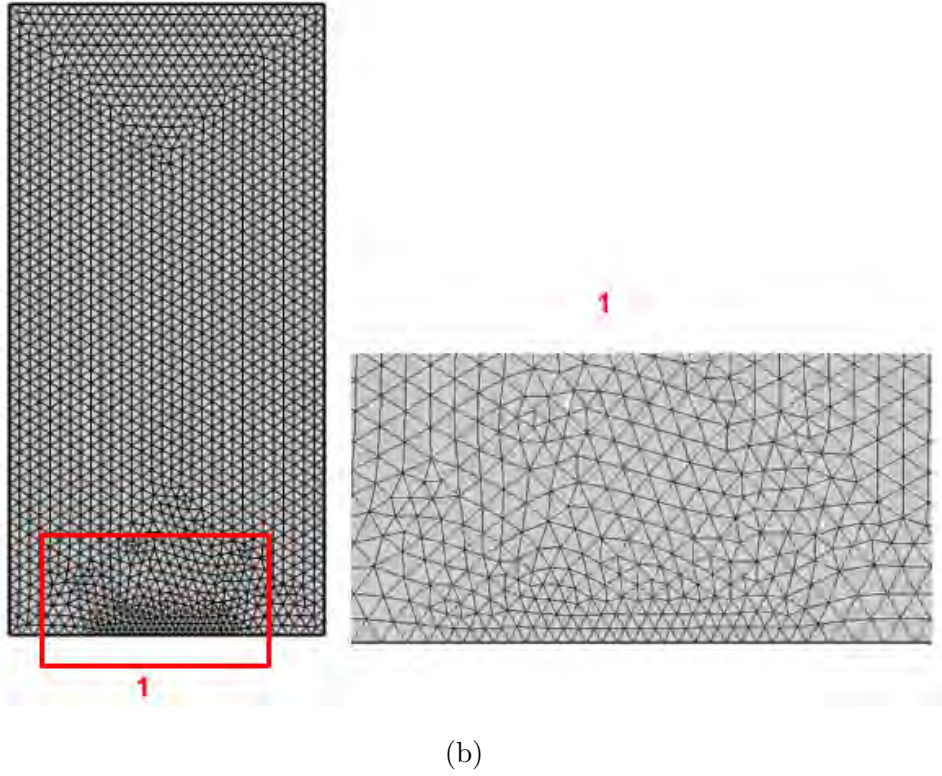


Figure 5.1: Physical schematic sketch and mesh distribution of the computational domain.

To be more specific, the Brownian motion and thermophoresis effects describe the nanopowder flow distribution. The micropolar fluid configuration characterizes two vector fields, i.e., one depicts the translatory motion (in terms of  $u^*, v^*$ ) of fluid particles and the other represents local angular motion of fluid molecules named as microrotation vector ( $n^*$ ). The microelement concentration at the boundaries is controlled by the constant  $n$  ( $0 \leq n \leq 1$ ). That is, when  $n = 0$  implies  $N^* = 0$  which corresponds to strong microelement concentration, when  $n = 0.5$  it characterizes weak microelement concentration (it means the anti-symmetric part of stress tensor vanishes), and the case  $n = 1$  identifies the turbulent flow modeling [78]. Moreover, the Boussinesq approximation is to hold in the flow field. In view of the above assumptions the following conservation equations are acceptable to narrate the said

physical configuration [48, 49].

$$\frac{\partial v^*}{\partial \tilde{y}} + \frac{\partial u^*}{\partial \tilde{x}} = 0, \quad (5.2.1)$$

$$\rho_f \left( v^* \frac{\partial u^*}{\partial \tilde{y}} + u^* \frac{\partial u^*}{\partial \tilde{x}} \right) = -\frac{\partial p^*}{\partial \tilde{x}} + (\mu_f + k) \left( \frac{\partial^2 u^*}{\partial \tilde{y}^2} + \frac{\partial^2 u^*}{\partial \tilde{x}^2} \right) + k \frac{\partial n^*}{\partial \tilde{y}} u^*, \quad (5.2.2)$$

$$\rho_f \left( v^* \frac{\partial v^*}{\partial \tilde{y}} + u^* \frac{\partial v^*}{\partial \tilde{x}} \right) = -\frac{\partial p^*}{\partial \tilde{y}} + (\mu_f + k) \left( \frac{\partial^2 v^*}{\partial \tilde{y}^2} + \frac{\partial^2 v^*}{\partial \tilde{x}^2} \right) - k \frac{\partial n^*}{\partial \tilde{x}} u^* +$$

$$g\beta\rho_f(1 - C_c)(T^* - T_c)g\beta(\rho_p - \rho_f)(C^* - C_c), \quad (5.2.3)$$

$$\rho_f j \left( v^* \frac{\partial n^*}{\partial \tilde{y}} + u^* \frac{\partial n^*}{\partial \tilde{x}} \right) = \gamma \left( \frac{\partial^2 n^*}{\partial \tilde{y}^2} + \frac{\partial^2 n^*}{\partial \tilde{x}^2} \right) - k \left( 2n^* + \frac{\partial u^*}{\partial \tilde{y}} - \frac{\partial v^*}{\partial \tilde{x}} \right), \quad (5.2.4)$$

$$v^* \frac{\partial T^*}{\partial \tilde{y}} + u^* \frac{\partial T^*}{\partial \tilde{x}} = \alpha_f \left( \frac{\partial^2 T^*}{\partial \tilde{y}^2} + \frac{\partial^2 T^*}{\partial \tilde{x}^2} \right) + \tau D_B \left( \frac{\partial T^*}{\partial \tilde{y}} \frac{\partial C^*}{\partial \tilde{y}} + \frac{\partial T^*}{\partial \tilde{x}} \frac{\partial C^*}{\partial \tilde{x}} \right) +$$

$$\tau \frac{D_T}{T_c} \left( \frac{\partial T^*}{\partial \tilde{y}} \right)^2 + \tau \frac{D_T}{T_c} \left( \frac{\partial T^*}{\partial \tilde{x}} \right)^2. \quad (5.2.5)$$

$$v^* \frac{\partial C^*}{\partial \tilde{y}} + u^* \frac{\partial C^*}{\partial \tilde{x}} = D_B \left( \frac{\partial^2 C^*}{\partial \tilde{y}^2} + \frac{\partial^2 C^*}{\partial \tilde{x}^2} \right) + \frac{D_T}{T_c} \left( \frac{\partial^2 T^*}{\partial \tilde{y}^2} + \frac{\partial^2 T^*}{\partial \tilde{x}^2} \right). \quad (5.2.6)$$

Here  $(u^*, v^*, n^*)$  are the velocity and micro-rotation vector.  $(T^*, C^*)$  denote the temperature and concentration profile.  $(\rho_f, \mu_f, k)$  indicate density, dynamic and micro-rotation viscosity kinematic viscosity. The micro-inertia and spin gradient viscosity is given by  $(j, \gamma)$ .  $(\beta, \alpha_f, \tau, D_T, D_B)$  denote thermal expansion and diffusivity, heat capacitance ratio, thermophoresis and Brownian motion effects parameters.  $(T_h, T_c$  and  $C_h, C_c)$  signifies temperature and nanoparticles distribution at heated and cold wall.

To obtain dimensionless system one can use the following variables[79].

$$\tilde{X} = \frac{\tilde{x}}{l}, \quad \tilde{Y} = \frac{\tilde{y}}{l}, \quad U^* = \frac{lu^*}{\alpha_f}, \quad V^* = \frac{lv^*}{\alpha_f}, \quad P^* = \frac{l^2 p^*}{\rho_f \alpha_f^2}, \quad N^* = \frac{l^2 n^*}{\alpha_f},$$

$$\theta(\tilde{X}, \tilde{Y}) = \frac{T^* - T_c}{T_h - T_c}, \quad \phi(\tilde{X}, \tilde{Y}) = \frac{C^* - C_c}{C_h - C_c}, \quad \text{Pr} = \frac{\nu_f}{\alpha_f}, \quad \text{Le} = \frac{\alpha_f}{D_B},$$

$$R = \frac{k}{\mu_f}, \quad \text{Ra} = \frac{g\beta(1 - C_c)(T_h - T_c)}{\alpha_f \nu_f}, \quad \text{Nr} = \frac{(\rho_p - \rho_f)(C_h - C_c)}{\rho_f \beta (T_h - T_c)(1 - C_c)}$$

$$\gamma = \left( \mu + \frac{k}{2} \right) j, \quad \text{Nb} = \frac{\tau D_B (C_h - C_c)}{\alpha_f}, \quad \text{Nt} = \frac{\tau D_T (T_h - T_c)}{\alpha_f T_c}. \quad (5.2.7)$$

Here,  $(U^*, V^*, N^*)$ ,  $P^*$ ,  $(\theta, \phi)$  are the dimensionless velocity profiles in  $x, y$  direc-

tions, micro-rotation distribution, pressure, temperature and nanopowder concentration. Whereas,  $Pr$ ,  $Le$ ,  $Ra$ , and  $R$ ,  $Nr$ ,  $Nt$ ,  $Nt$  indicate the Prandtl, Lewis, Rayleigh number and microrotation viscosity, buoyancy, thermophoresis, Brownian motion controlling parameters. By use of above dimensionless variables (5.2.7) the conservation equations (5.2.1)-(5.2.4) in reduced non-dimensional take the form

$$\frac{\partial V^*}{\partial \tilde{Y}} + \frac{\partial U^*}{\partial \tilde{X}} = 0, \quad (5.2.8)$$

$$V^* \frac{\partial U^*}{\partial \tilde{Y}} + U^* \frac{\partial U^*}{\partial \tilde{X}} = -\frac{\partial P^*}{\partial \tilde{X}} + (1+R) \Pr \left( \frac{\partial^2 U^*}{\partial \tilde{Y}^2} + \frac{\partial^2 U^*}{\partial \tilde{X}^2} \right) + \Pr R \frac{\partial N^*}{\partial \tilde{Y}} \quad (5.2.9)$$

$$V^* \frac{\partial V^*}{\partial \tilde{Y}} + U^* \frac{\partial V^*}{\partial \tilde{X}} = -\frac{\partial P^*}{\partial \tilde{Y}} + (1+R) \Pr \left( \frac{\partial^2 V^*}{\partial \tilde{Y}^2} + \frac{\partial^2 V^*}{\partial \tilde{X}^2} \right) - \Pr R \frac{\partial N^*}{\partial \tilde{X}} + Ra \Pr Nr (1-\phi) + Ra \Pr \theta, \quad (5.2.10)$$

$$V^* \frac{\partial N^*}{\partial \tilde{Y}} + U^* \frac{\partial N^*}{\partial \tilde{X}} = \Pr \left( 1 + \frac{R}{2} \right) \left( \frac{\partial^2 N^*}{\partial \tilde{Y}^2} + \frac{\partial^2 N^*}{\partial \tilde{X}^2} \right) - \Pr R \left( 2N^* + \frac{\partial U^*}{\partial \tilde{Y}} - \frac{\partial V^*}{\partial \tilde{X}} \right) \quad (5.2.11)$$

$$V^* \frac{\partial \theta}{\partial \tilde{Y}} + U^* \frac{\partial \theta}{\partial \tilde{X}} = \left( \frac{\partial^2 \theta}{\partial \tilde{Y}^2} + \frac{\partial^2 \theta}{\partial \tilde{X}^2} \right) + Nt \left( \frac{\partial \theta}{\partial \tilde{Y}} \right)^2 + Nt \left( \frac{\partial \theta}{\partial \tilde{X}} \right)^2 + Nb \left( \frac{\partial \theta}{\partial \tilde{Y}} \frac{\partial \phi}{\partial \tilde{Y}} + \frac{\partial \theta}{\partial \tilde{X}} \frac{\partial \phi}{\partial \tilde{X}} \right), \quad (5.2.12)$$

$$V^* \frac{\partial \phi}{\partial \tilde{Y}} + U^* \frac{\partial \phi}{\partial \tilde{X}} = \frac{1}{Le} \left( \frac{\partial^2 \phi}{\partial \tilde{Y}^2} + \frac{\partial^2 \phi}{\partial \tilde{X}^2} \right) + \frac{Nt}{Le Nb} \left( \frac{\partial^2 \theta}{\partial \tilde{Y}^2} + \frac{\partial^2 \theta}{\partial \tilde{X}^2} \right). \quad (5.2.13)$$

following the relevant boundary conditions

At  $\tilde{Y} = 0$  (Bottom wall)

$$\begin{aligned} \theta_{\tilde{Y}} = \phi_{\tilde{Y}} &= 0, & 0 \leq \tilde{X} \leq P_1, \\ \theta = \phi &= 1, & P_1 \leq \tilde{X} \leq P_2, \\ \phi_{\tilde{Y}} = \theta_{\tilde{Y}} &= 0, & P_1 \leq \tilde{X} \leq 1, \\ N^* &= -n_1 U_{\tilde{Y}}^*, & 0 \leq \tilde{X} \leq 1. \end{aligned} \quad (5.2.14)$$

At  $\tilde{Y} = 2$  (Top wall)

$$\begin{aligned} \theta_{\tilde{Y}} = \phi_{\tilde{Y}} &= 0, & 0 \leq \tilde{X} \leq 1, \\ N^* &= -n_1 U_{\tilde{Y}}^*, \end{aligned} \quad (5.2.15)$$

At left  $\tilde{X} = 0$  and right wall  $\tilde{X} = 1$

$$\begin{aligned}\theta &= \phi = 0, \\ N^* &= -n_1 V_{\tilde{X}}^*,\end{aligned}\quad 0 \leq \tilde{Y} \leq 2. \quad (5.2.16)$$

$U^* = V^* = 0$  on all boundaries.

In which the subscript  $Y$  denotes the partial derivative.

Local Nusselt number can be expressed as

$$Nu = -\frac{\partial\theta}{\partial n},$$

here  $n$  indicates normal direction to the plane, particularly

$$\frac{\partial\theta}{\partial n} = \sqrt{\left(\frac{\partial\theta}{\partial\tilde{X}}\right)^2 + \left(\frac{\partial\theta}{\partial\tilde{Y}}\right)^2},$$

whereas, average Nusselt number is defined as

$$Nu_{av} = -\int_{\Omega} \frac{\partial\theta}{\partial n} d\Omega,$$

where  $\Omega$  represents the heated boundary of domain.

### 5.3 Results and discussion

The theoretical analysis on the numerically solved proposed physical model is considered in this section. The viscous flow of nanofluid comprises microrotation of molecules in a vertically placed rectangular shaped enclosure is investigated. The natural convective flow is maintained in the regime due to mounted heated source at the bottom boundary. The adopted numerical scheme offered the outputs against various parameters  $Ra(10^2 - 10^3)$ ,  $R(0.5 - 2)$ ,  $Le(1 - 10^2)$ ,  $Lh(0.2 - 1.0)$  are classified in-term of line graphs and contour maps. In natural convection Rayleigh number is responsible to maintained the buoyancy-driven flow in the regime. Figures 5.2(a - d) shows the effects of  $Ra$  on velocity, microrotation profile, concentration and temperature distribution. It is obvious that as Rayleigh parameter enhances the convection

process intensify. Thus, resulting the quick movement of fluid from bottom warm region to upward cooler region, can be observed in Fig. 5.2(a). It can be noted that the fluid velocity is maximum near the bottom wall and gradually decreases in cooler region. Thermal distribution in the region also enhance as  $Ra$  augments, See Fig. 5.2(b). Another important impact of  $Ra$  on molecule microrotation is depicted in Fig. 5.2(c). Since, as the translatory movement increase due to higher  $Ra$ , the microrotation also escalates. Thus, the microrotation profile increases corresponding to  $Ra$  impact. In similar manner the concentration distribution increase upon rising  $Ra$  as illustrated in Fig. 5.2(d). Contour maps of streamlines and microrotation vector against  $Ra$  are presented in Fig. 5.3(a – f). As by nature high  $Ra$  implies stronger buoyancy effects therefore, its impact on flow depicts that when  $Ra$  augment from  $10^2 - 10^3$  two type (anti-clockwise, clockwise) of streamlines and microrotation circulation are formed. Initially, the clockwise circulations are strong at smaller  $Ra$ , whereas, the anti-clockwise circulations gradually maximizes as  $Ra$  rise. This effect for both distributions (streamlines and microrotation vector) shown in figures 5.3(a – f). The internal orientation of each particle in the micropolar fluid is controlled by vortex viscosity parameter  $R$ . Basically it characterizes the concentration of microconstituents and its magnitude increase as  $R$  increases. That is non-zero increasing nature of  $R$  corresponds to attenuation in the linear vorticity and augmentation in angular vorticity. On the other hand convective mode of heat transfer decreases in the presence of strong microconstituents concentration. Following this, the effects of additional viscosity parameter ( $R$ ) on flow and thermal profile are illustrated in line graphs 5.4(a – d) and contour maps figures 5.5(a – f). It should be noted that as  $R$  varies from 0.5 to 2 the viscous forces predominant the buoyancy effects thereby decreasing the flow field as depicted in Fig. 5.4(a). Since,  $R$  is an additional viscosity coefficient thus it would be more energy consumed to overcome the large viscosity effects which eventually decline the free molecule motion. Ac-

cordingly, the microrotation distribution diminish in the regime, as portrayed in Fig. 5.4(b). The variations in concentration and thermal distribution are not much significant. This make sense because of reduction in convective mode of flow which leads to lesser thermal and concentration distribution, see figures 5.4(c, d). Figures 5.5(a – d) exhibit the streamlines and contour plots of microrotation. Both these profiles reveal that streamlines and isoline distribution decreases. This is due to the maximum viscous nature of fluid in the presence of  $R$  which dominant over the buoyancy forces eventually reduce the translatory and rotatory movement of fluid molecules. The intensification impact of heat source length  $Lh$  on flow field is disclosed in-terms of line graphs in Figs 5.6(a – d) and in isotherms contours Figs 5.7(a – d). One can see that an increase of heated source length up-to entire lower boundary thereby boosts free convection in regime. The surge in both temperature and concentration occurs due to stronger buoyancy effects. This result is depicted in figures 5.6(a, b). This also implies that translatory and rotatory movement of molecules also augment as shown in figures 5.6(c, d). The variations in isotherms contours against various heated source length are described in figures 5.7(a – d). It can be observed from these figures that intensification of heat source corresponds to stronger buoyancy effects thus the heat propagates in the entire cavity by the response of natural convection. The alterations in flow behavior against various Lewis number are delineated in figures 5.8(a – d). As the Lewis number correlate the thermal and mass diffusivity. It should be noted that maximum  $Le$  corresponds to higher thermal diffusivity and less mass transfer. In the results a stronger thermal environment and lower concentration distribution are found as evident in figures 5.8(a, b). The velocity and microrotation graphs against  $Le$  depict that velocity depresses while the micro-rotation vector is not much effected by Lewis number, can be assessed in figures 5.8(c, d). The escalating behavior of average Nusselt number against  $Ra$  and  $Lh$  is shown in figures 5.9(a, b).

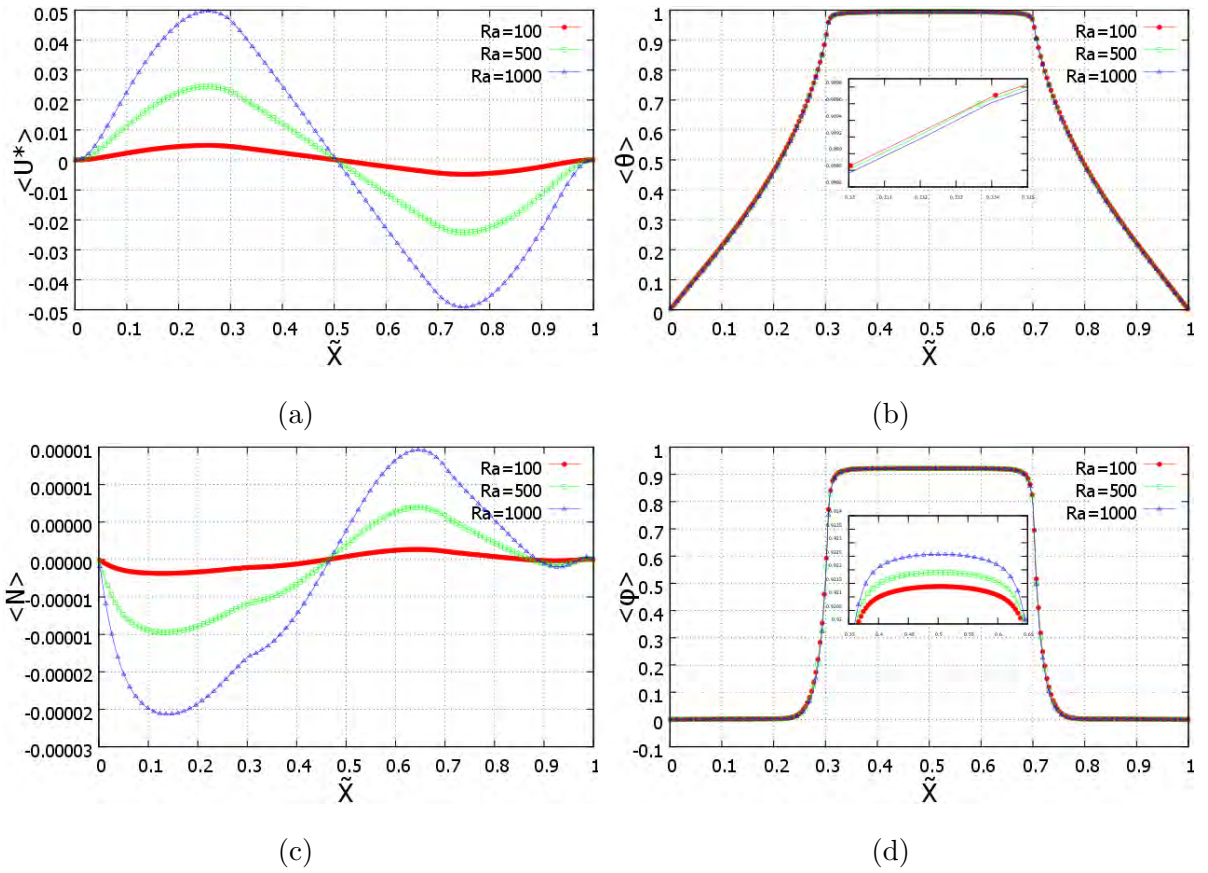
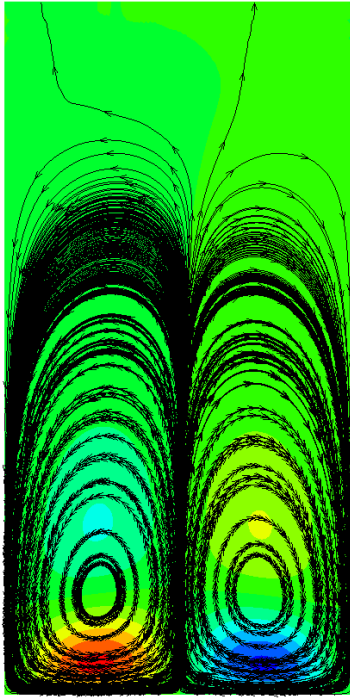
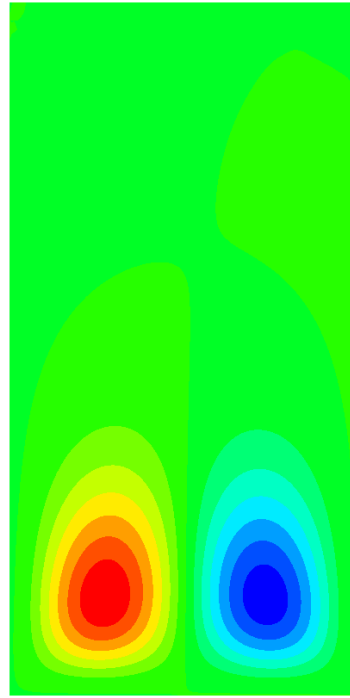
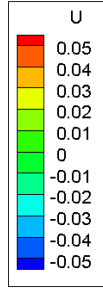
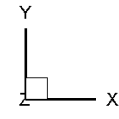


Figure 5.2: Impact of various  $Ra$  on: a) Horizontal velocity component, b) Temperature, c) Angular momentum, d) Concentration.

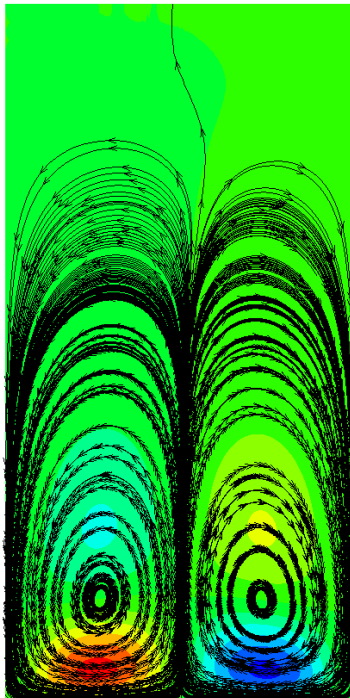
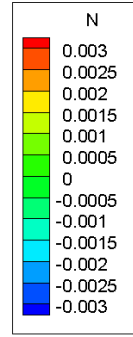
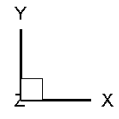




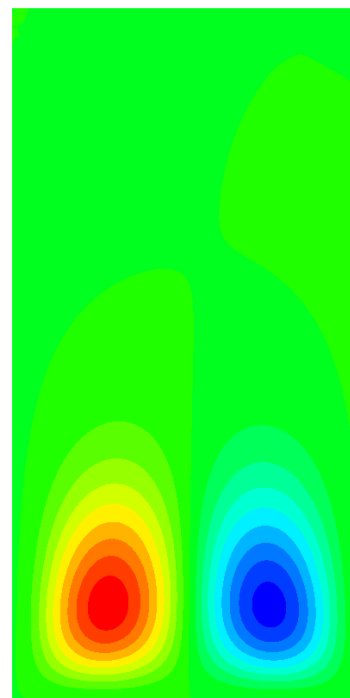
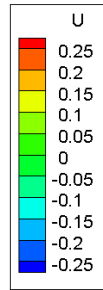
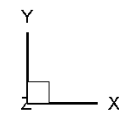
(a)



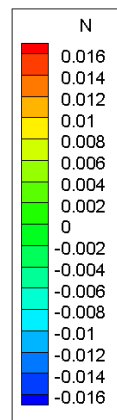
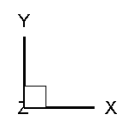
(b)



(c)



(d)



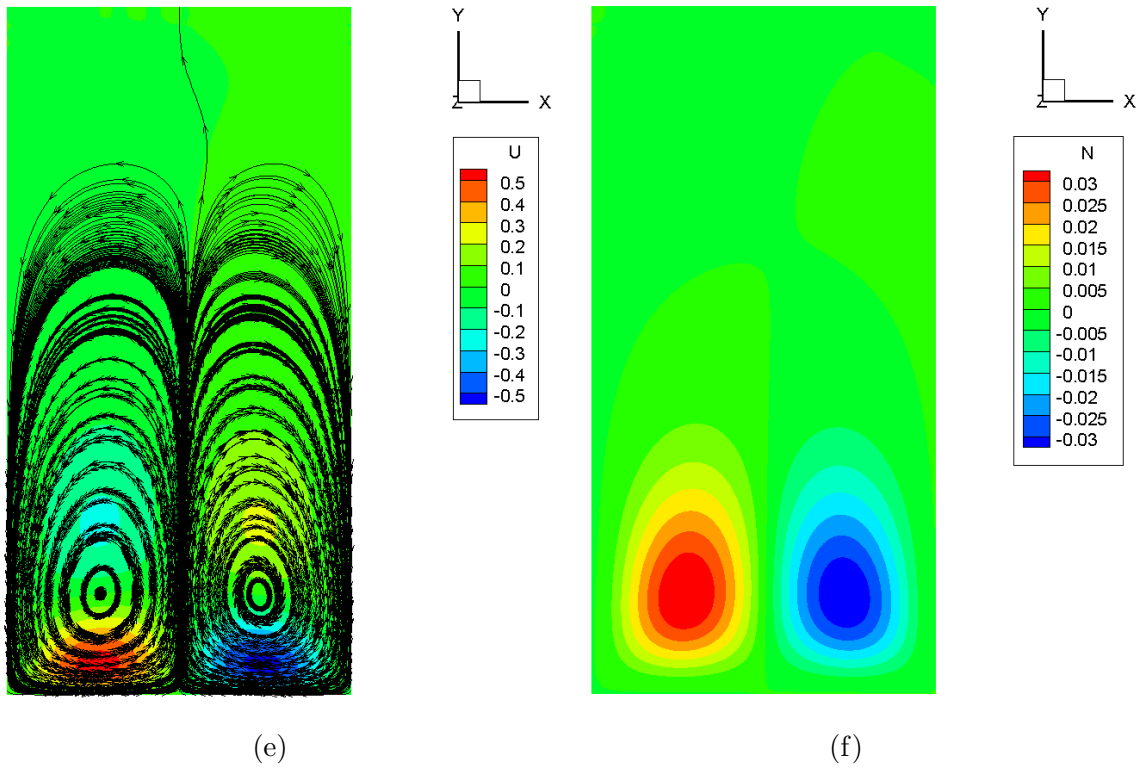
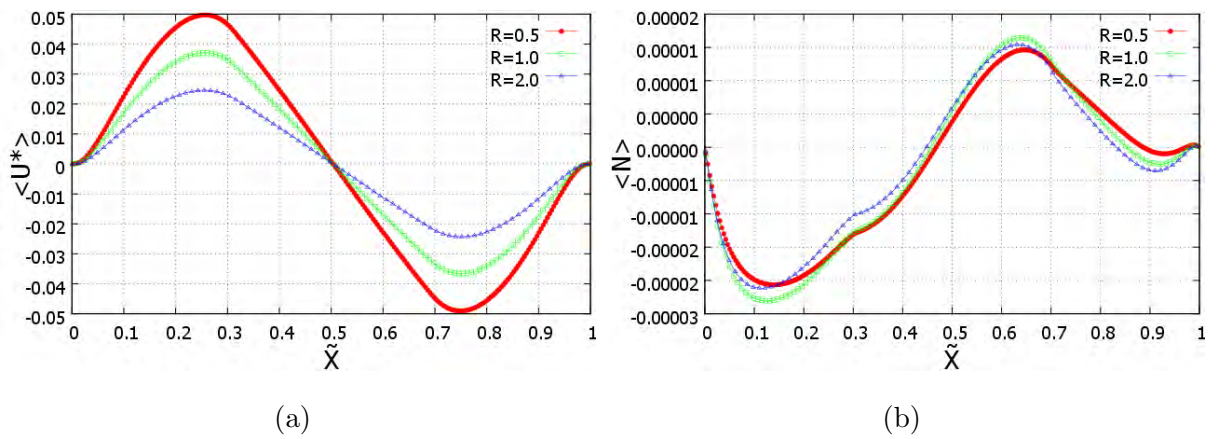
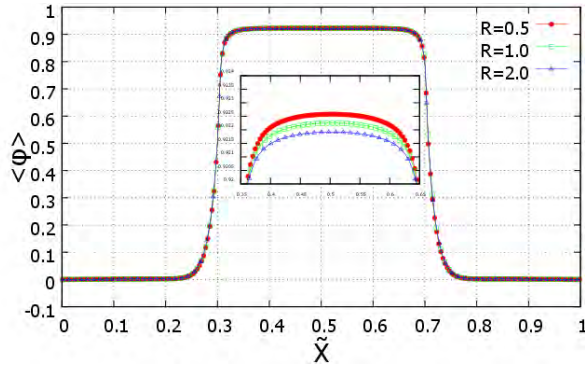
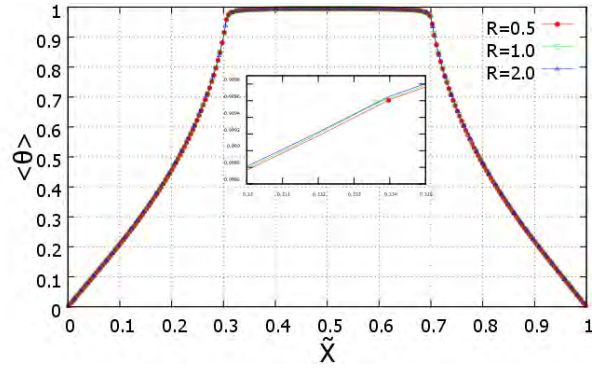


Figure 5.3: Variations in streamlines and microinertia vector at  $Pr = 2.0, Nr = 0.01, Le = 100, R = 0.5, Nt = 0.5, Nb = 0.5, Lh = 0.4$  : (a, b)  $Ra = 100$ , (c, d)  $Ra = 500$ , (e, f)  $Ra = 1000$ .





(c)

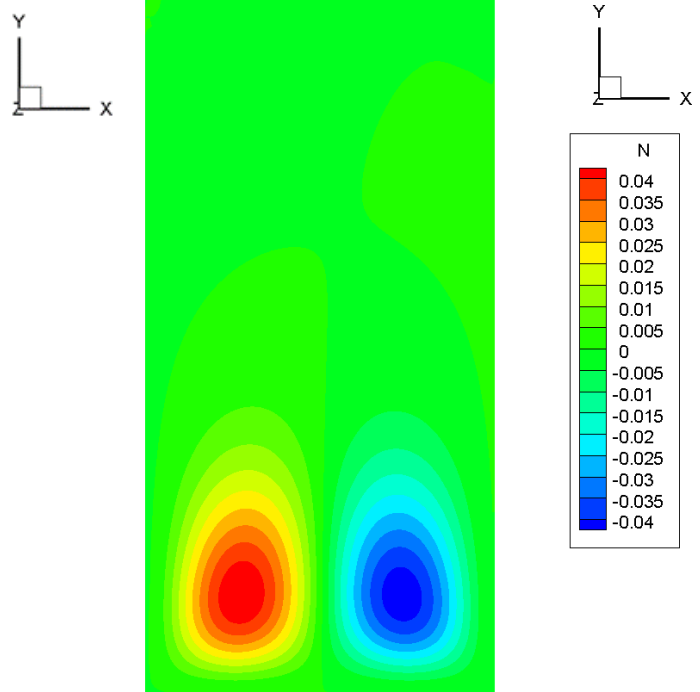


(d)

Figure 5.4: Impact of  $R$  on: a) velocity b) microrotation vector, c) concentration, d) temperature.



(a)



(b)

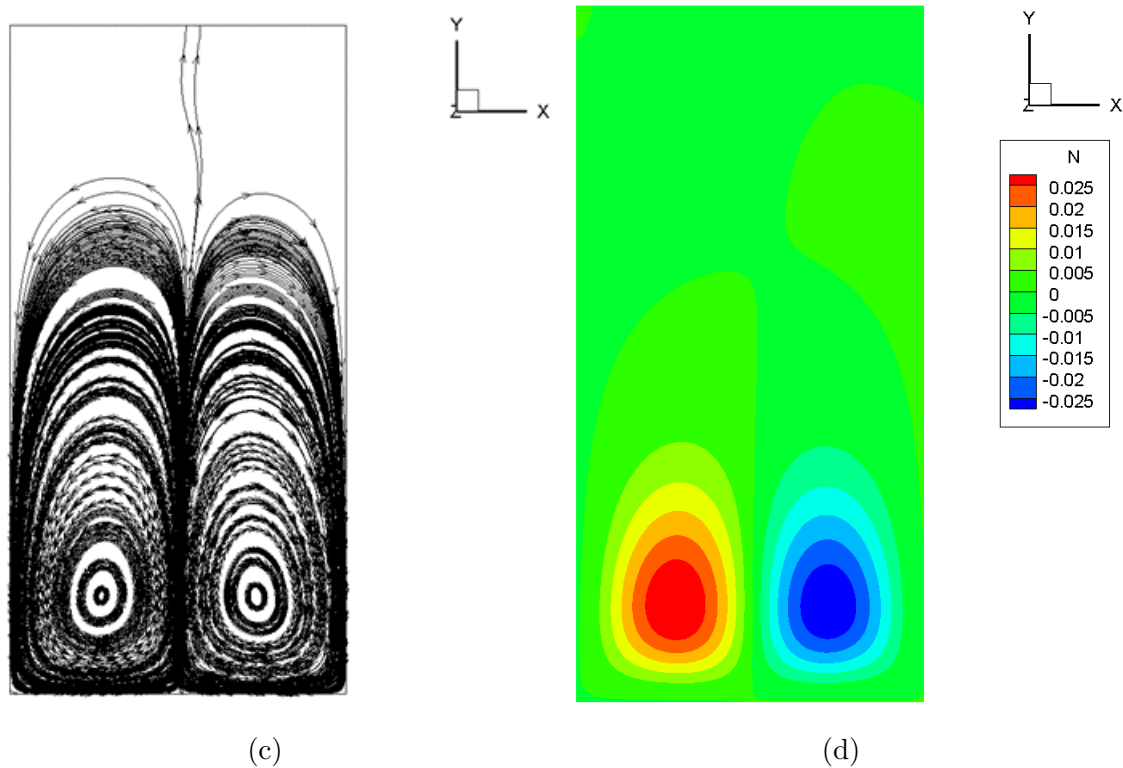
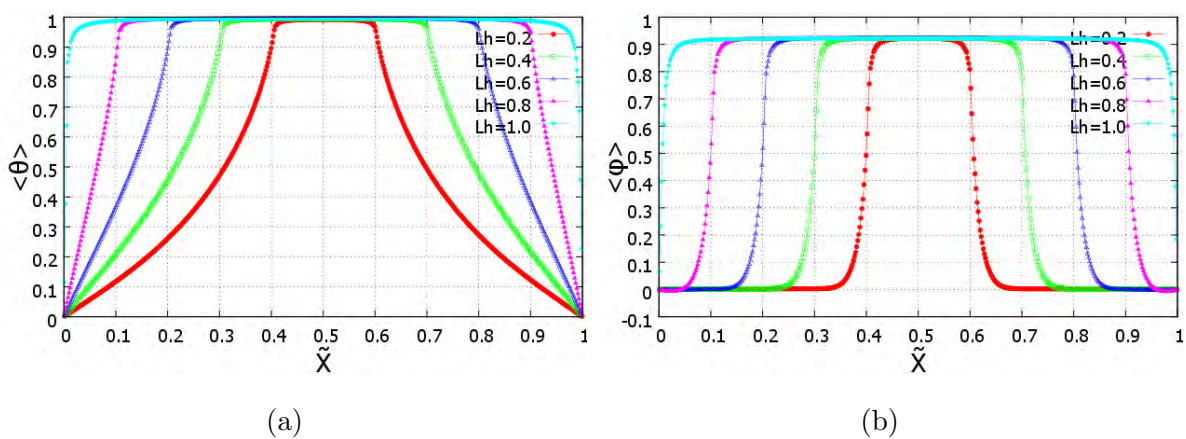
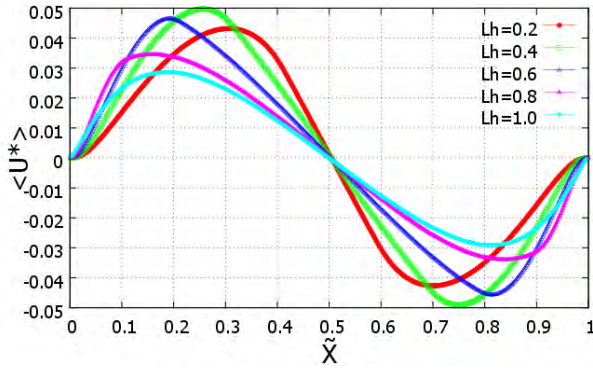
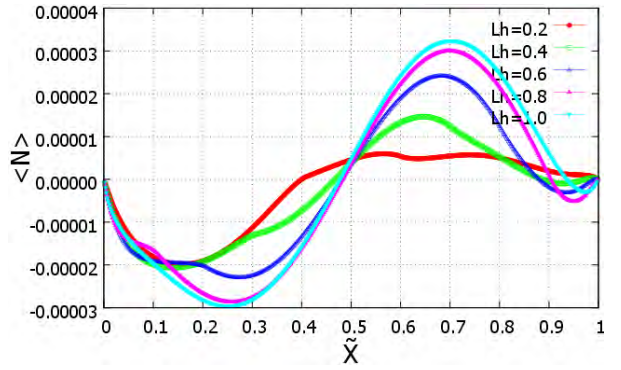


Figure 5.5: Variations in streamlines and microinertia vector at  $Pr = 2.0, Nr = 0.01, Le = 100, Ra = 1000, Nt = 0.5, Nb = 0.5, Lh = 0.4$  : (a, b)  $R = 1$ , (c, d)  $R = 2.0$ .



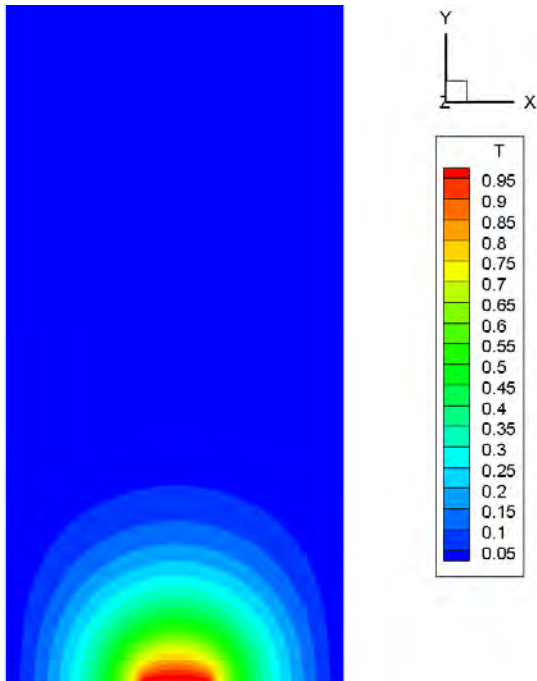


(c)

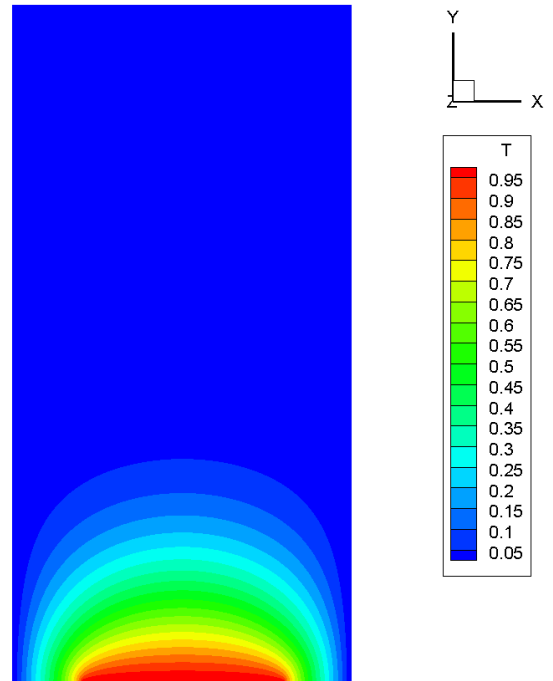


(d)

Figure 5.6: Impact of  $Lh$  on thermal, concentration and flow profiles.



(a)



(b)

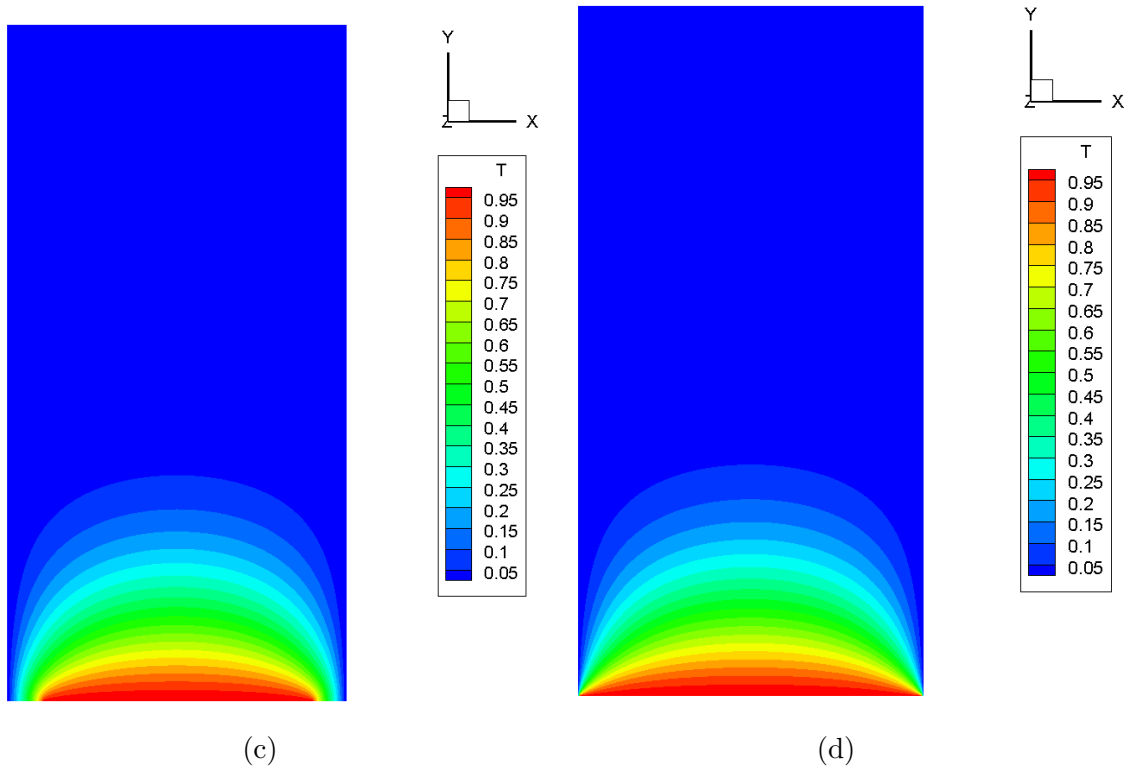
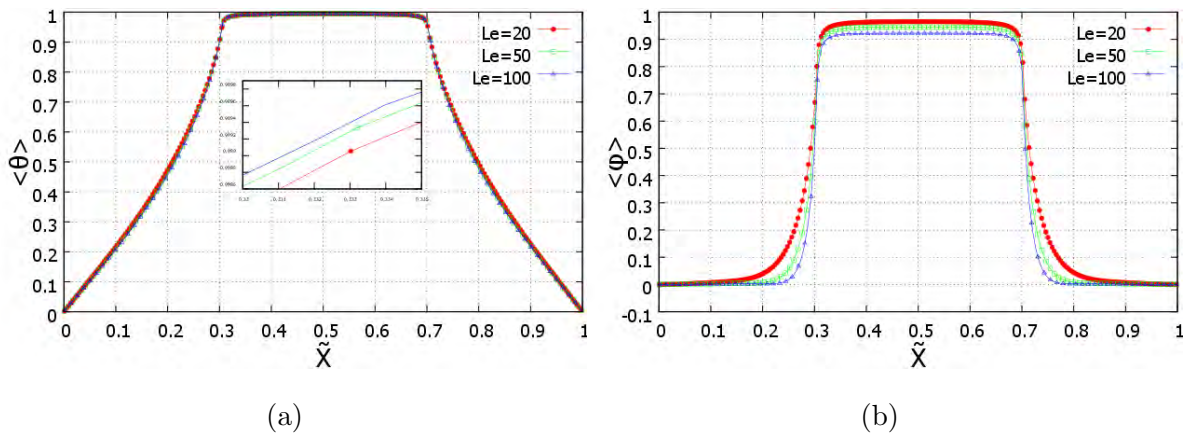
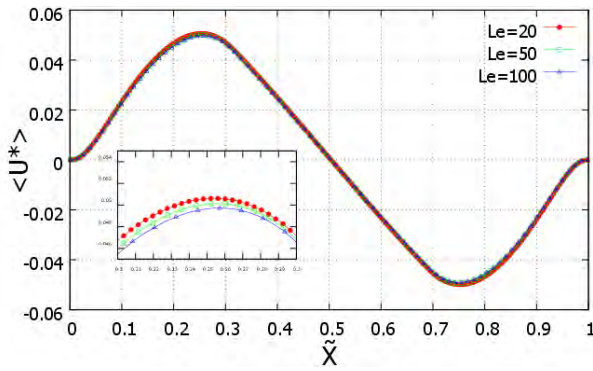
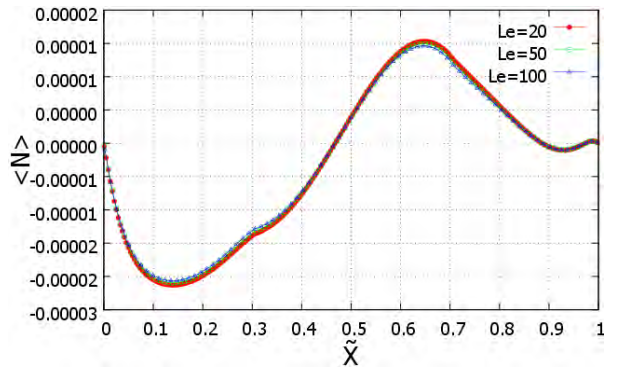


Figure 5.7: Isotherms against various  $Lh$ .

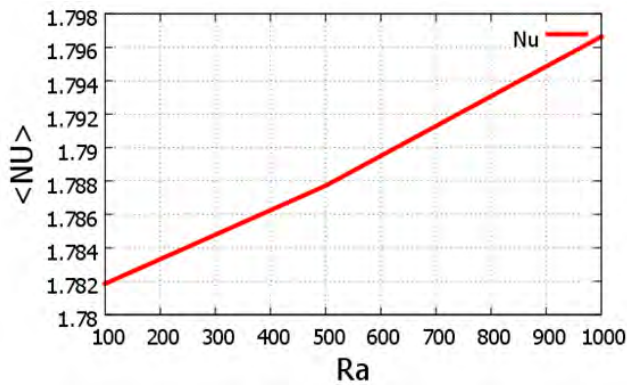




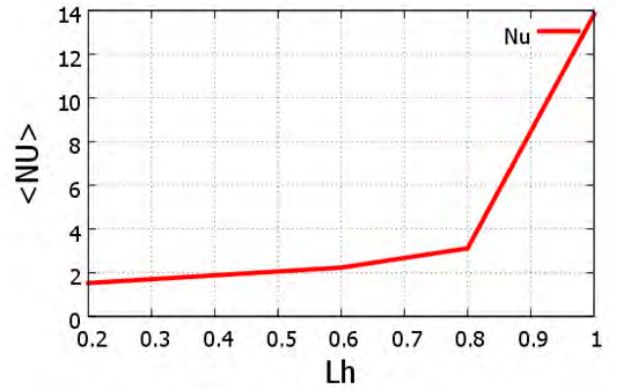
(c)



(d)

Figure 5.8: Impact of  $Le$  on flow field and thermal distribution.

(a)



(b)

Figure 5.9: Variations in average Nusselt number against (a)  $Ra$  and (b)  $Lh$ .

## 5.4 Concluding remarks

This investigation contains the free convective flow induced by a heated source in the bottom of vertical rectangular enclosure. Finite volume scheme is adopted to simulate the partial differential system of the physical model. The parameters controlling the flow field includes Rayleigh number, vortex viscosity, Lewis and heated source length. It is concluded that, the velocity, microrotation vector, temperature and concentration augments at larger  $Ra$ . Streamlines distribution increase as  $Ra$  elevates. Rising impact of  $R$  possess decay in flow profiles due to stronger viscous nature. Increase in  $R$  corresponds to decrease in convective transport mode which implies decay in temperature and concentration profiles. Increment in heated source length strengthen the buoyancy forces which implies the rise in flow and thermal field. Addition of  $Le$  leads to rise in temperature and fall in concentration distribution. Average velocity and temperature diminish against  $R$  whereas, average Nusselt number is enhanced against both  $Ra$  and  $Lh$ .



# Chapter 6

## Simulation for nanofluid convective flow inside a partially adiabatic enclosure influenced by a sinusoidal oriented heated element

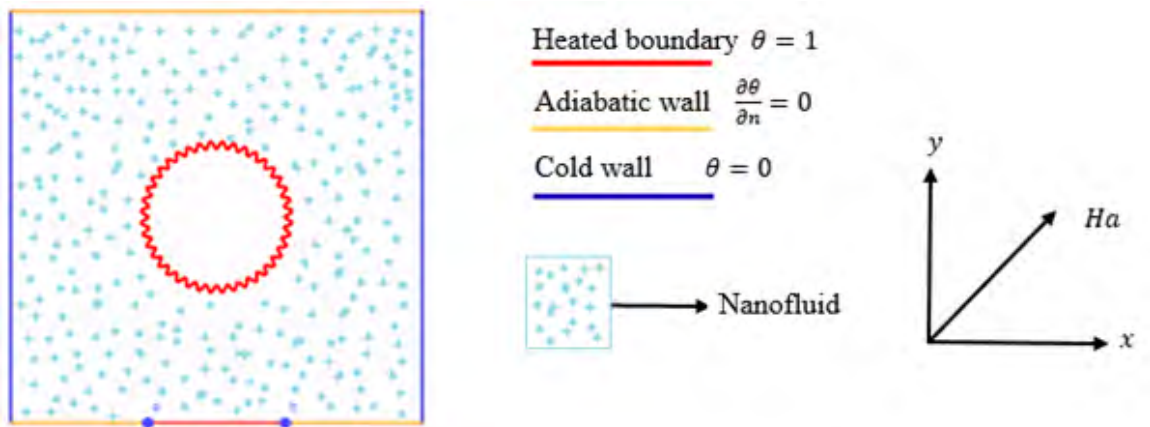
### 6.1 Introduction

Natural convection is produced by buoyancy force, in which fluid movement is caused by the rise and fall of hot and cold fluid that is followed by density difference. Free/natural convection has emerging applications in engineering [80] and industries such as petroleum [81], nuclear reactors [82], cooling of electronic devices [83], crystal growth [84], solar collectors [85], biomass [86] and sterilization of canned food [87] etc. To enhance the convection transportation we have performed a numerical experiment of convective flow situation in the presence of nanoparticles in this chapter. In the configuration a heated element placed at core region of squared shaped enclosure which is filled with water-based Oxide nanoparticles. The flow distribution is sub-

ject to magnetic field applied in an inclined manner. Further, assumption includes the left and right wall of cavity are considered cooled, the lower boundary is heated partially, and the remaining boundaries are taken adiabatic. This whole physical system is translated in mathematical form which involve partial differential system. Specifically, the flow dynamics and thermal transmission are the quantities of physical interest. The computational scheme presents the outcomes toward various emerging parameters in both line-graphs and isolines.

## 6.2 Model description and governing equations

The physical configuration shown in figure 6.1(a) consists of an enclosure which contained a heated element placed at the core region. The cavity side-length is assumed to be  $L$ , the outside boundaries of enclosure are considered such that, lower wall is partially heated the upper is taken adiabatic while the left and right walls are kept cooled. Further, the cavity contains  $CuO$ -water nanofluid which undergoes a two-dimensional flow dynamics and thermal distribution in a steady state.



(a)

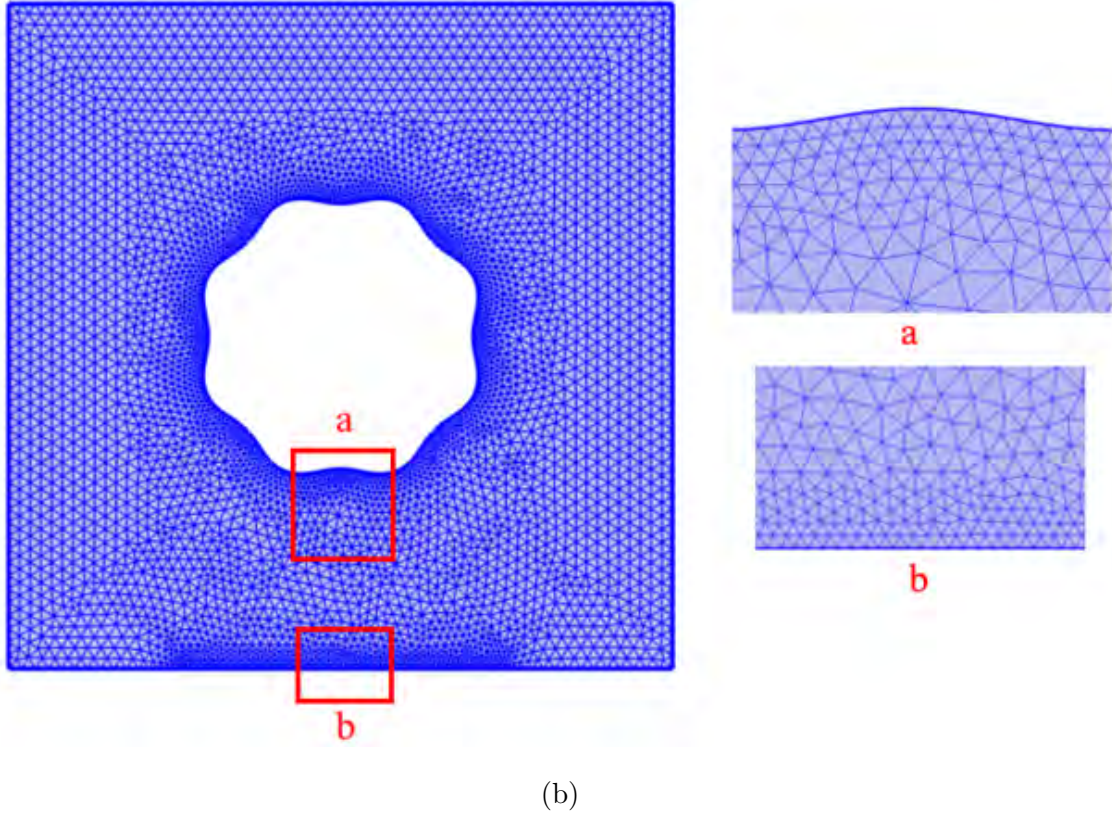


Figure 6.1: Physical configuration and (b) Mesh distribution of domain.

Specifically, the existence of temperature difference in the regime involve buoyancy forces which are responsible for free convective flow distribution. Moreover, the operating fluid is affected by Lorentz forces applied in an inclined manner to the flow situation. The viscosity and thermal conductivity are assumed to be temperature dependent, thus incorporating the Boussinesq approximation the basic governing equations are as follows:

$$\vec{\nabla} \cdot \vec{v} = 0, \quad (6.2.1)$$

$$\vec{v} \cdot \nabla \vec{v} = \frac{-1}{\rho_{nf}} \nabla p + \nu_{nf} \nabla^2 \vec{v} + \frac{\vec{i}}{\rho_{nf}} f_x + \frac{\vec{j}}{\rho_{nf}} \left( f_y + (\rho\beta)_{nf} g (T - T_c) \right), \quad (6.2.2)$$

$$\vec{v} \cdot \nabla T = \frac{k_{nf}}{(\rho C_p)_{nf}} \nabla^2 T. \quad (6.2.3)$$

Here  $\vec{v} = (u, v)$  is the velocity profiles  $\nabla = \left( \frac{\partial}{\partial x}, \frac{\partial}{\partial y} \right)$  is two-dimensional differential

operator,  $(\rho_{nf}, \nu_{nf})$  indicate the nanofluid density and viscosity,  $(\beta_{nf}, (Cp)_{nf}, k_{nf})$  are the thermal expansion coefficient, specific heat and thermal conductivity of nanofluid.  $T$  signify temperature profile while  $(T_h, T_c)$  are the thermal distribution on heated and cooled boundaries.  $f_x$  and  $f_y$  denote the applied inclined Lorentz forces which are defined as:

$$\begin{aligned} f_x &= \sigma_{nf} B_0^2 \sin \alpha (v \cos \alpha - u \sin \alpha), \\ f_y &= \sigma_{nf} B_0^2 \cos \alpha (-v \cos \alpha + u \sin \alpha). \end{aligned} \quad (6.2.4)$$

In which  $(\alpha, B_0)$  are the inclination angle and strength of the imposed magnetic field, whereas  $\sigma_{nf}$  is the nanofluid's electrical conductivity.

Here adopted model for thermophysical characteristics is presented by Koo–Kleinstreuer–Li [57, 58] the properties are described as:

$$k_{nf} = k_{static} + k_{Brownian}. \quad (6.2.5)$$

The conventional static and Brownian motion part as discussed by [56, 57] can be described as

$$k_{static} = k_f \left( 1 + \frac{3 \left( \frac{k_s}{k_f} - 1 \right) \phi}{\left( \frac{k_s}{k_f} + 2 \right) - \left( \frac{k_s}{k_f} - 1 \right) \phi} \right), \quad (6.2.6)$$

where the dynamic part is given by

$$k_{Brownian} = 5 \times 10^4 \phi (\rho C_p)_f \sqrt{\frac{k_b T_0}{\rho_s d_s}} f(T_0, \phi). \quad (6.2.7)$$

Equation (6.2.7) is modified by Li [58] and defined a new function  $\zeta$  thus the relation reduces as

$$k_{Brownian} = 5 \times 10^4 \phi (\rho C_p)_f \sqrt{\frac{k_b T_0}{\rho_s d_s}} \zeta(T_0, \phi, d_s). \quad (6.2.8)$$

In which,  $(k_b = 1.38 \times 10^{-23}, T_0 = 0.5(T_h - T_c), d_s)$  are the Boltzmann constant, average temperature and solid particles diameter, whereas the modified function  $\zeta$  is

given by:

$$\zeta(T_0, \phi, d_s) = (a_1 + a_2 \ln d_s + a_3 \ln \phi + a_4 \ln d_s \ln \phi + a_5 \ln d_s^2) \ln T_0 + a_6 + a_7 \ln d_s + a_8 \ln \phi + a_9 \ln d_s \ln \phi + a_{10} \ln d_s^2. \quad (6.2.9)$$

In above equation (6.2.9) the coefficients  $a_1 - a_{10}$  and numerical values of thermo-physical properties for *CuO*-water are shown in table 2.1 and 2.2. Moreover, the electrical conductivity and effective viscosity in term of static and Brownian motion as considered in [56, 57] can be written as:

$$\mu_{nf} = \mu_{static} + \mu_{Brownian} = \frac{\mu_f}{(1 - \phi)^{2.5}} + \frac{k_{Brownian} \mu_f}{k_f Pr}, \quad (6.2.10)$$

$$\sigma_{nf} = \sigma_f \left( 1 + \frac{3 \left( \frac{\sigma_s}{\sigma_f} - 1 \right) \phi}{\left( \frac{\sigma_s}{\sigma_f} + 2 \right) - \left( \frac{\sigma_s}{\sigma_f} - 1 \right) \phi} \right). \quad (6.2.11)$$

A dimensionless equations system can be obtained by utilizing the following variables [75, 88].

$$(X, Y) = \left( \frac{x}{L}, \frac{y}{L} \right), \quad (U, V) = \left( \frac{uL}{\alpha_f}, \frac{vL}{\alpha_f} \right), \quad P = \frac{pL^2}{\rho_f \alpha_f}, \quad \theta = \frac{T - T_c}{T_h - T_c},$$

$$Ra = \frac{g \beta_f (T - T_c) L^3}{\alpha_f \nu_f}, \quad Pr = \frac{\nu_f}{\alpha_f}, \quad Ha = B_0 L \sqrt{\frac{\sigma_f}{\mu_f}}. \quad (6.2.12)$$

By use of the above variables the non-dimensional equations take the form

$$\check{\check{V}} \cdot \nabla \check{\check{V}} = \frac{-\rho_f}{\rho_{nf}} \nabla P + \frac{\nu_{nf}}{\nu_f} Pr \nabla^2 \check{\check{V}} + \vec{i} \frac{\rho_f}{\rho_{nf}} Pr F_X + \vec{j} \frac{\rho_f}{\rho_{nf}} \left( Pr F_Y + \frac{(\rho \beta)_{nf}}{(\rho \beta)_f} Pr Ra \theta \right), \quad (6.2.13)$$

$$\check{\check{V}} \cdot \nabla \theta = \frac{(\rho C_p)_f}{(\rho C_p)_{nf}} \frac{k_{nf}}{k_f} \nabla^2 \theta. \quad (6.2.14)$$

Where  $\check{\check{V}} = (U, V)$  is the dimensionless flow velocity,  $(Pr, Ra, Ha)$  are the Prandtl number, Rayleigh parameter and Hartman number, while the non-dimensional Lorentz

forces  $(F_X, F_Y)$  are defined as:

$$\begin{aligned} F_X &= \frac{\sigma_{nf}}{\sigma_f} Ha^2 \sin\alpha (V \cos\alpha - U \sin\alpha), \\ F_Y &= \frac{\sigma_{nf}}{\sigma_f} Ha^2 \cos\alpha (-V \cos\alpha + U \sin\alpha). \end{aligned} \quad (6.2.15)$$

The boundary constraints of physical domain can be written in non-dimensional form as: The no-slip condition implies that  $U = V = 0$  on all boundaries. The thermal conditions are as follows. At vertical portions of the setup:

$$\begin{aligned} \text{At } X = 0, 0 \leq Y \leq 1, \\ X = 1, 0 \leq Y \leq 1, \end{aligned} \quad \theta = 0. \quad (6.2.16)$$

Upper and lower adiabatic portions:

$$\begin{aligned} \text{At } Y = 0, 0 \leq X \leq a, \quad b \leq X \leq 1 \\ Y = 1, 0 \leq X \leq 1, \end{aligned} \quad \frac{\partial\theta}{\partial n} = 0. \quad (6.2.17)$$

At outer length and inner element

$$\text{At } Y = 0, a \leq X \leq b, \theta = 1, \quad (6.2.18)$$

$$\text{At } (X - 0.5)^2 + (Y - 0.5)^2 = r^2, \theta = 1. \quad (6.2.19)$$

Here we have consider the inner element in the form of parametric curve as:

$$C(t) = (r(t)\cos(t), r(t)\sin(t)), \quad (6.2.20)$$

where  $r(t) = A_m \sin(nt) + r$ , in which  $(A_m, n)$  signify the amplitude and element frequency. The heat transfer rate is the quantity of physical interest, here it is defined as said by Nusselt number can be expressed as follows

$$Nu = -\frac{k_{nf}}{kf} \int_{h_L} \frac{\partial T}{\partial n} dX, \quad (6.2.21)$$

where,  $h_L$  represents both the outer and internal heated portions while  $n$  is the normal direction to the heated surfaces.

### 6.3 Results and discussion

The simulation has been carried out on the governing equations of the physical model consisting: a partially heated square enclosure with heated element inside core. The setup is filled with *CuO*-water nanofluid, herein the results obtained after numerical simulation against the range of emerging physical parameters controlling flow profile (velocity field and stream function) and thermal distribution (temperature and heat transfer rate), such as nanoparticles fraction, Rayleigh number, Hartmann number, inclination angle of applied magnetic field, frequency and amplitude of inner heated element, are presented in line graphs and contour plots. Since the operating fluid is Newtonian nanofluid therefore the Prandtl number has fixed value ( $Pr = 6.2$ ), the other parameters are considered in the range ( $1e3 \leq Ra \leq 1e4$ ), ( $10 \leq Ha \leq 1e2$ ), ( $\frac{\pi}{4} \leq \alpha \leq \frac{3\pi}{4}$ ) ( $0 \leq \phi \leq 0.15$ ), ( $0 \leq n \leq 0.1$ ). The thermophysical properties and values of the coefficients  $a_i$  are presented in table 2.1 and 2.2.

Figures 6.2(*a – d*) present the line-graphs for Nusselt numbers, temperature and velocity profile at the defined tracks against nano-particles concentrations. It is examined that the Nusselt number taken along inner heated element up-surges in wavy manner by the increment of solid particles fraction. See figure 6.2(*a*) however, the heat transport rate computed at bottom heated source length decline in response to addition of nanoparticles fraction as illustrated in figure 6.2(*b*). The thermal transmission and flow distribution along the vertical mean path are depicted in figures 6.2(*c, d*). It is reported in figure 6.2(*c*) that increasing  $\phi$  the thermal field has maximum values between (0.0 – 0.3) and decreasing nature in the interval (0.7 – 1.0) the later diminishing behavior illustrate the influence of upper cooled wall. The flow profile  $V$  in figure 6.2(*d*) depicts that at lower concentration it has maximum values in both interval (0.0 – 0.3) and (0.7 – 1.0). Its behavior decline as the fluid becomes more concentrated by adding nano-particles fraction. To be more specific when  $\phi$

augments it implies more viscous regime thereby the flow dynamics fall along the vertical mean path. The isotherms variations and streamline distribution against various nano-particles fractions are demonstrated in figure 6.3(*a – f*). From portrayed figures it can be observed that at low concentration the natural convection is stronger and thereby the contour maps for stream function and isotherms are stronger in the regime. See figures 6.3(*a, b*). On the other hand, when particle fraction grow the figures 6.3(*c – f*) ensure that buoyancy forces getting weaker and, in the output, secondary circulations (clockwise) get stronger while the heat transmission switches from convection to conduction mode. In physical meaning the molecules strength enhances due to the addition of nano-particles volume fractions which provides resistance to the flow dynamics and therefore effect the isolines distribution as evident in figures 6.3(*a – f*) below.

The variations in flow and heat configuration influenced by the element frequency number  $n$  are presented in line-graphs and contour maps. It is portrayed in figure 6.4(*a*) that heat transfer rate computed at inner heated element propagate in wave form in the regime. It should be noted that undulation number  $n$  really affect the heat flux rate which possess higher values as  $n$  ascends. Heat transfer rate estimated at outer heated-portion is found decreased as considered in figure 6.4(*b*), this is because of the increasing number of undulations suppresses the thermal transmission in the lower regime. Figures 6.4(*c, d*) depict the thermal profile and  $y$ -velocity component computed along the mean vertical path. The graph displayed in figure 6.4(*c*) describe that temperature in the enclosure increases as the element frequency  $n$  grow. Since as,  $n$  multiply the element strength increases which leads to maximum thermal transmission in the enclosure. The velocity field has minimum values by increasing the undulation of the heated element. It can be noticed that maximum rolls of heated element possess resistance to the flow profile, hence decreasing flow field in  $y$ -direction as illustrated in figure 6.4(*d*). The flow patterns and thermal contours in-term of



streamlines and isotherms against various element frequency number  $n$  are presented in figures 6.5( $a - e$ ) and figure 6.5( $b - f$ ). It seems that in the flow pattern the clockwise circulations are increased whereas, the counterclockwise tends to decline as  $n$  changes from 0.02 to 0.08. See figures 6.5( $a - e$ ). The isotherms in figures 6.5( $b - f$ ) depict that at the default  $n$  ( $= 0.02$ ) the thermal distribution is of convective nature; it switches to conductive mode when the element undulations increase up to 0.08. At smaller  $n$  the isotherms indicate that temperature is distributed through convection while at large element undulations isotherms spread uniformly, and its intensity decreases due to predominant conduction effect.

Another important parameter arise due to the impact of Lorentz forces is the Hartmann number  $Ha$ , and its influences on flow dynamics and energy distribution are considered in figures 6.6 and 6.7. Form the line graphs shown in figures 6.6( $a - d$ ) it can be noticed that the stronger Lorentz forces translated by maximizing Hartmann number  $Ha$ , the attenuation of flow profile occurs due to resistive nature of the Lorentz forces. Consequently, the  $y$ -velocity component decrease computed along the vertical mean position as described in the figure 6.6( $a$ ). The temperature profile has a transverse effect against  $Ha$ . As plotted in the figure 6.6( $b$ ) it is examined that along the vertical path temperature has escalating behavior between (0.0 – 0.3) and reduces in the interval (0.7 – 1.0). The heat transmission rate both at the inner element and outer heated length is a decreasing function of  $Ha$  as illustrated in figures 6.6( $c, d$ ). It can be noticed that increase of Hartmann number attenuates the convective heat transfer mechanism, implies that the applied magnetic field possess negative effects on buoyancy forces resulting the dominant conductive heat transfer in the regime thus Nusselt numbers decline. Figures 6.7( $a - e$ ) and 6.7( $b - f$ ) present the streamlines and isotherms for various  $Ha$ . The flow patterns indicate that streamlines rarefy at higher Hartmann number. It ensures that magnetic forces oppose the flow dynamics and can be confirmed from the isolines in figures 6.7( $a - e$ ) that intensity

of the form formed circulations (clockwise and anti-clockwise) reduces against  $Ha$  in the range (1 – 100). As in the above explanation we have discussed that increase of Hartmann number the convective heat transmission in the enclosure reduces and the conductive transportation remains dominant. Hence, from the isotherms contour in figures 6.7( $b - f$ ) clarifies that at lower  $Ha$  there is still convective heat transmission occurs but when its values multiply the mode of thermal transport converted to conduction mechanism and the isothermal lines spread uniformly in the cavity.

The angle of inclination of applied magnetic field also influenced the flow and thermal profiles, its variations are presented in figure 6.8. For  $\alpha = 0$  i.e., when the magnetic field is parallel to the flow direction there is no significant impact on the flow pattern, two circulations in streamlines distribution with uniform density are formed as shown in figure 6.8( $a$ ). Varying inclination angle from  $\frac{\pi}{4}$  to  $\frac{\pi}{2}$  and  $\frac{3\pi}{4}$  the flow patterns change, at  $\alpha = \frac{\pi}{4}$  the contours of stream function indicate that anti-clockwise circulations are pushed upward while the clockwise circulations squeezed downward. See figure 6.8( $c$ ). When the Lorentz forces impact occur perpendicular (i.e.,  $\alpha = \frac{\pi}{2}$ ) to the flow both streamline circulations tend to reduce as exhibited in figure 6.8( $e$ ). The magnetic force applied at  $\alpha = \frac{3\pi}{4}$  the orientations of the clockwise circulation changes form downward to upward whereas, the counterclockwise patterns are pushed downward as presented in figure 6.8( $g$ ). On the other hand, thermal profile depicts that there is no significant impact of the angle of inclination of the magnetic field. The isotherms are spread uniformly in the cavity just its orientation is reversed when  $\alpha$  changes from  $\frac{\pi}{4}$  to  $\frac{3\pi}{4}$  i.e., at angle  $\alpha = \frac{\pi}{4}$  isotherms are pushed slightly upward while at  $\alpha = \frac{3\pi}{4}$  isolines are pressed downward as given in figures 6.8( $b - h$ ). The stem-parameter involve in natural convection transportation is Rayleigh number  $Ra$  and its impact on flow configuration cannot be ignored. The outcomes of the proposed solution against different  $Ra$  are reported in line-graphs and contour maps as portrayed in figure 6.9 and 6.10. By nature,  $Ra$  is related to buoyancy forces which maintain

natural convection in the regime. Hence, strengthening  $Ra$  boosts buoyancy effects which leads to stronger convection regime. The heat transfer rate against improving Rayleigh number indicate maximum values computed at both heated sources (i.e., inner element and outer portion). See figures 6.9(*a, b*). The temperature distribution given in figure 6.9(*c*) exhibit that in the interval (0.0 – 0.3) it depicts decreasing value while in interval (0.7 – 1.0) it has maximizing behavior. This can be interpreted as at lower half the heat transmitted from heated lower length and inner element opposes each other thus thermal profile has lower values. Whereas, in the upper half heat propagated from inner element in the upward cooled region thus its values increase as  $Ra$  augments. The  $y$ -velocity component computed along the vertical mean path illustrate higher values at various  $Ra$  as given in figure 6.9(*d*). The flow distribution demonstrated by stream function and isotherms is also controlled by Rayleigh number. It can be observed that increasing impact of  $Ra$  possess stronger buoyancy forces. The stream function depict that the flow pattern involves two circulations and with growing  $Ra$  both the vertices getting stronger. This implies that convection transportation is dominant in the region see figures 6.10(*a – e*). The isotherms also report that thermal transmission take place through convection remains dominant, since as  $Ra$  is directly proportional to stronger buoyancy effects. This explanation can be confirmed from the following figures 6.10(*b – f*).

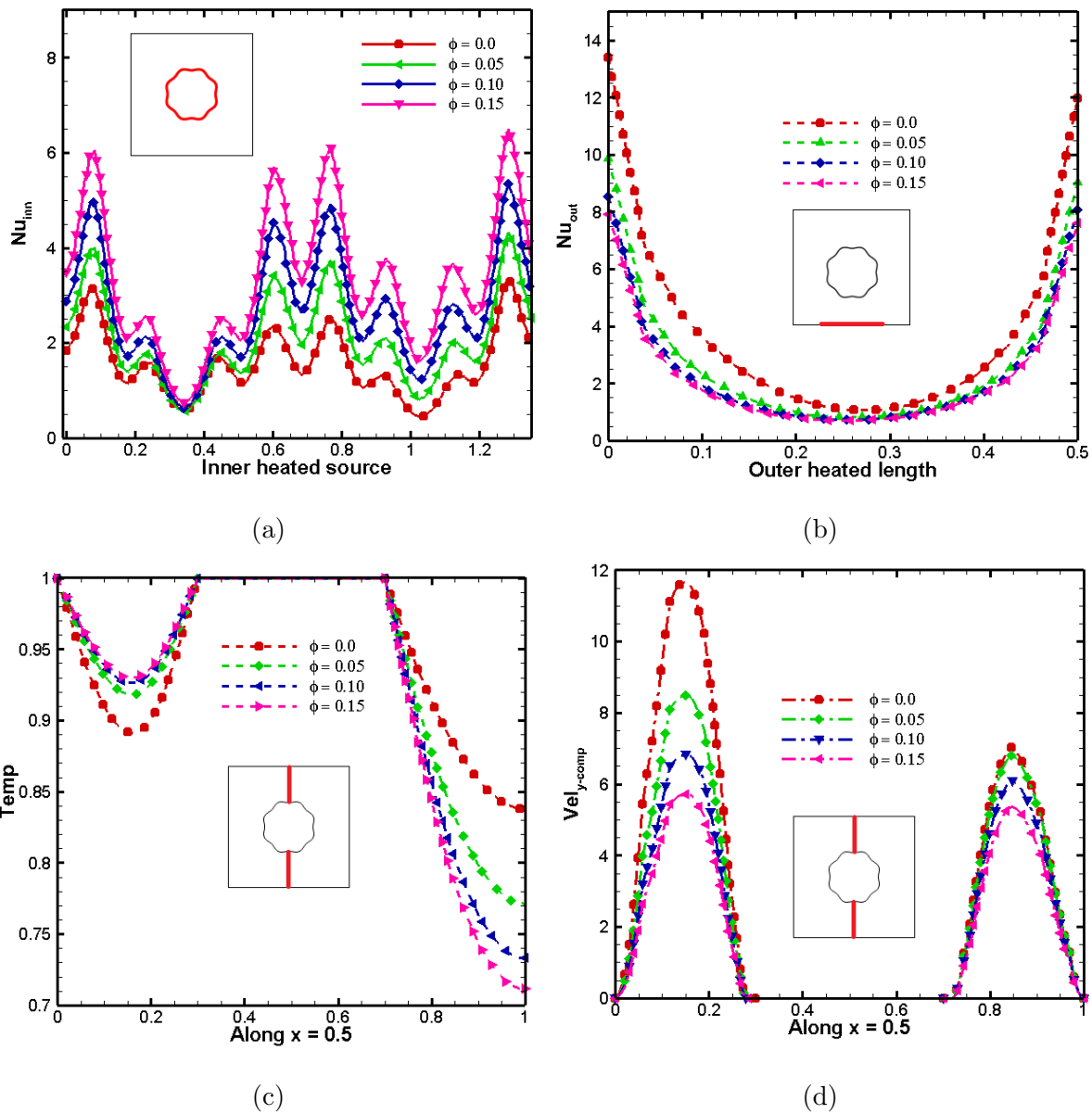
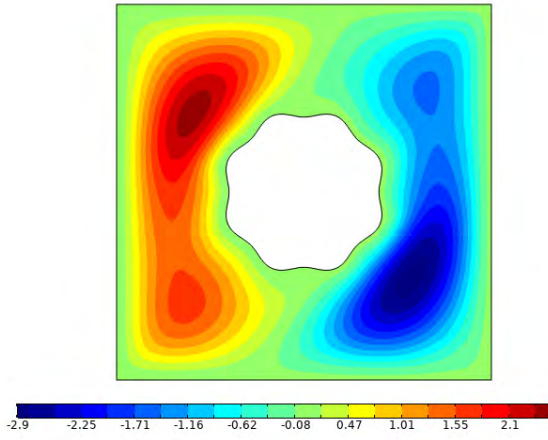
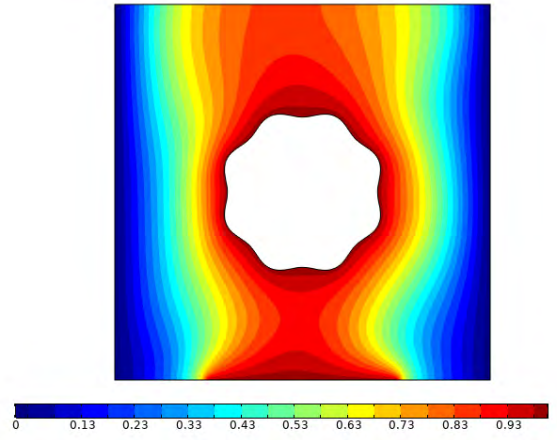


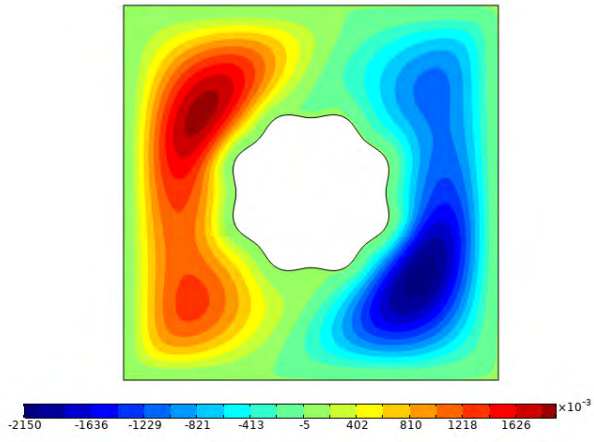
Figure 6.2: Impact  $\phi$  on (a),(b) Nusselt numbers (c) temperature and (d) velocity along the defined paths.



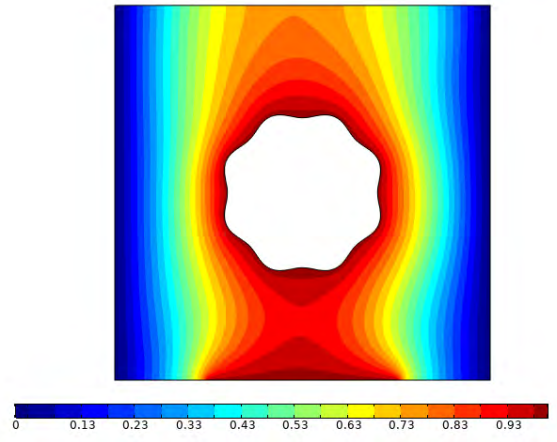
(a)  $\phi=0.0$



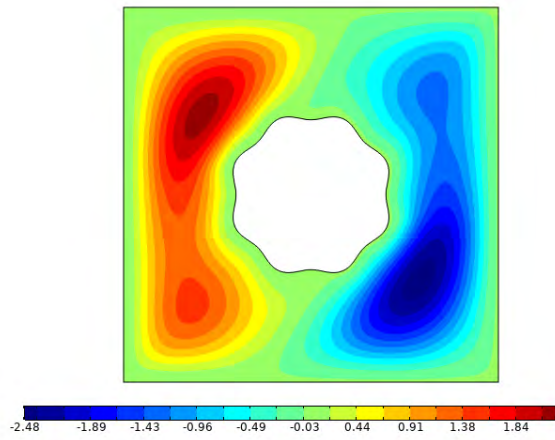
(b)  $\phi=0.0$



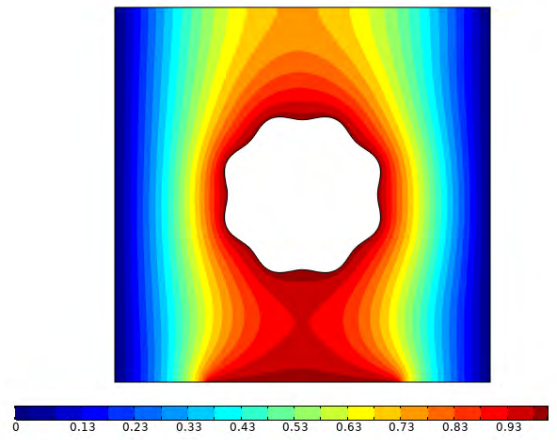
(c)  $\phi=0.05$



(d)  $\phi=0.05$



(e)  $\phi=0.10$



(f)  $\phi=0.10$

Figure 6.3: Variations in Isotherms (left) and Streamlines (right) at various  $\phi$ .

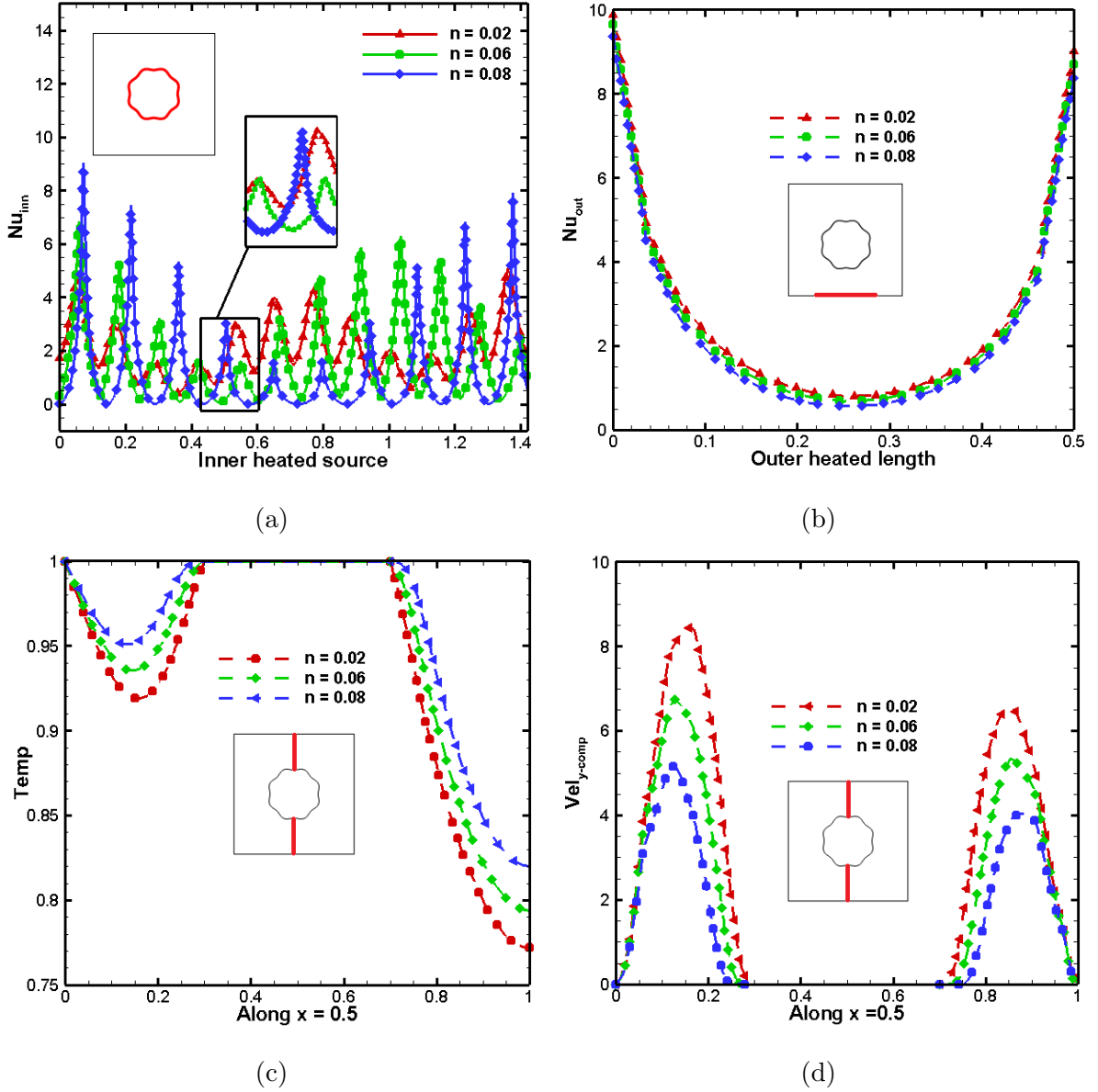


Figure 6.4: Influence of element frequency  $n$  on (a, b) Nusselt numbers, (c) temperature and (d) velocity at shown paths.

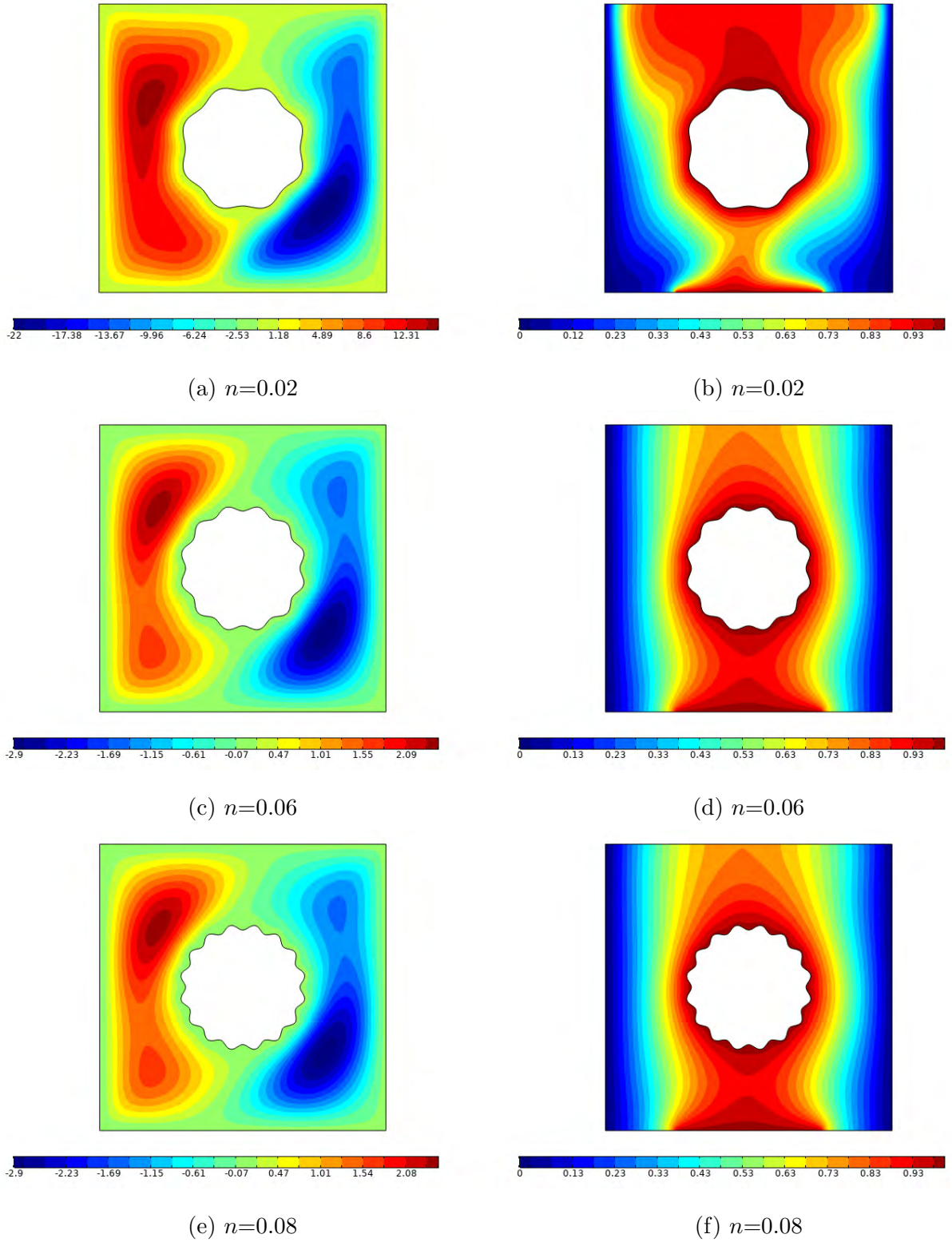
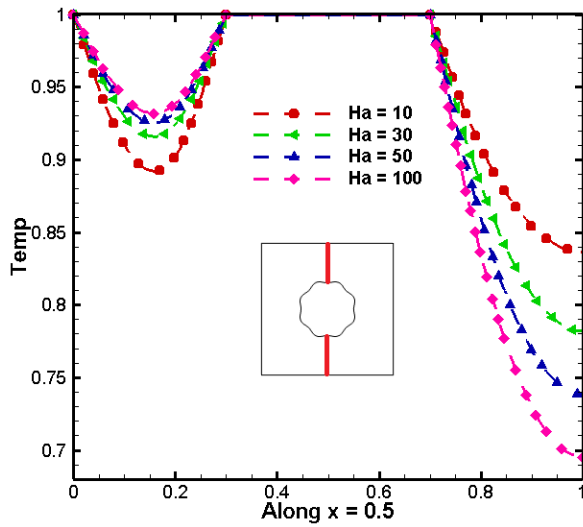
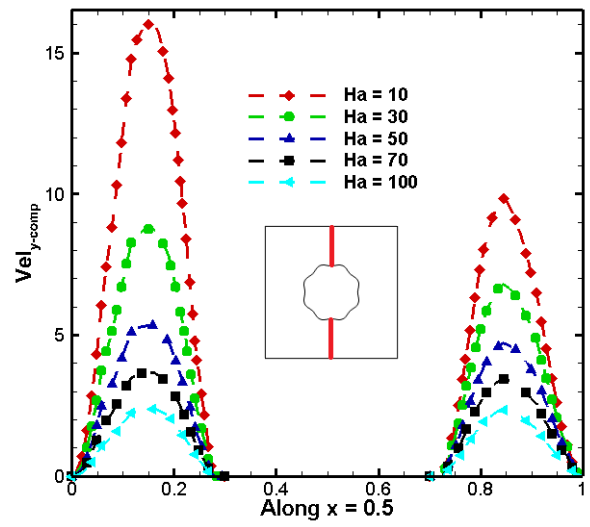


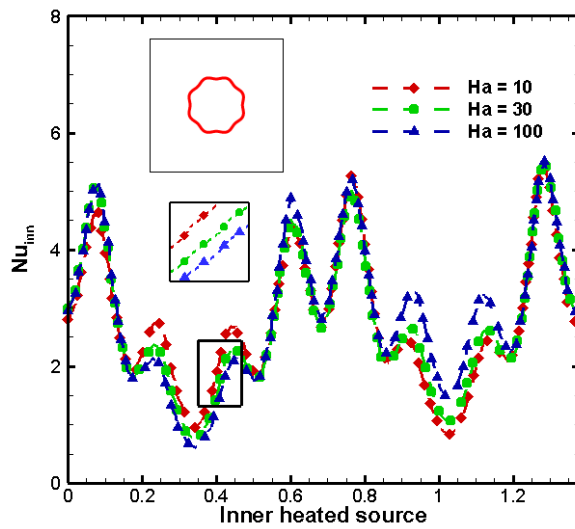
Figure 6.5: Streamlines (left) and Isotherms (right) at different heated element frequency  $n$ .



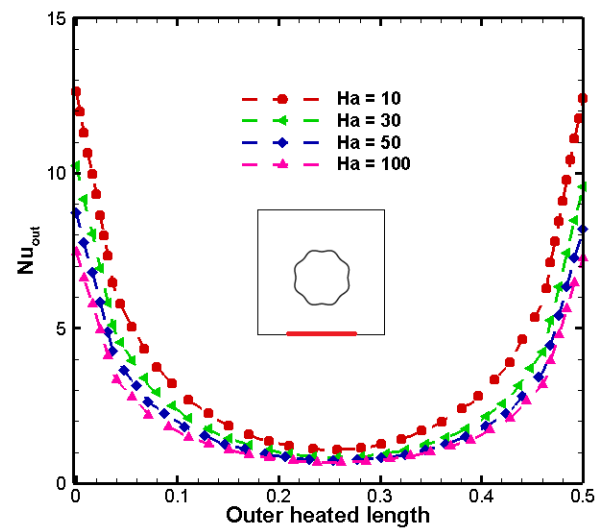
(a)



(b)



(c)



(d)

Figure 6.6: Hartman number impact on (a), (b) heat transfer rate, (c) temperature and (d)  $y$ -velocity at indicated paths.



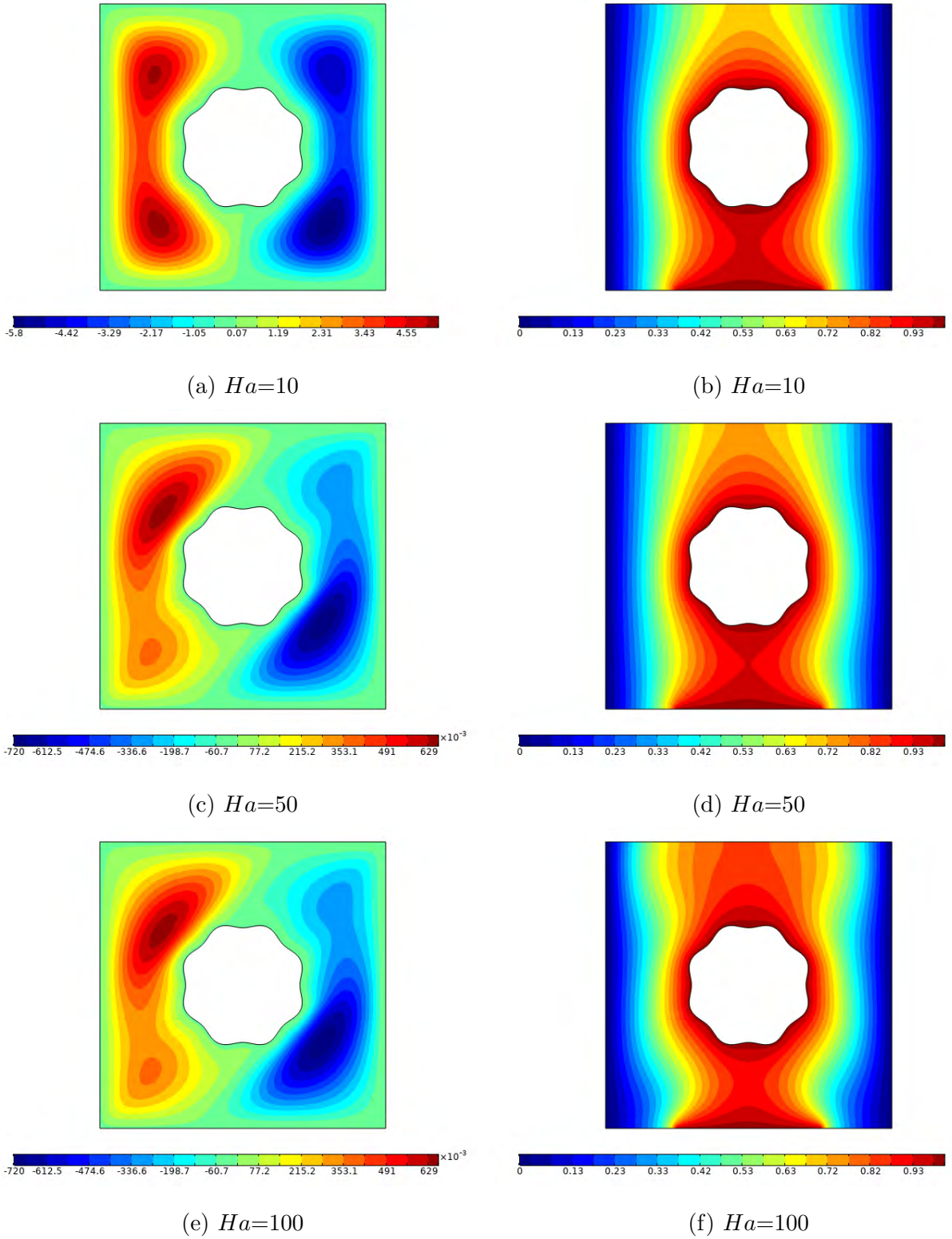
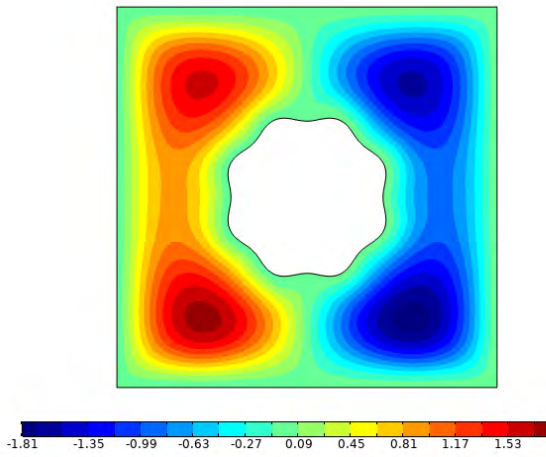
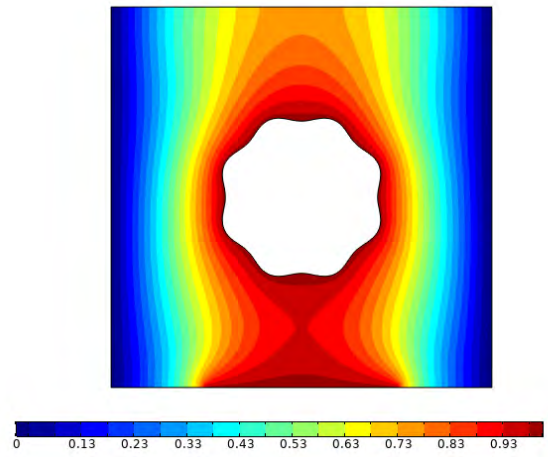


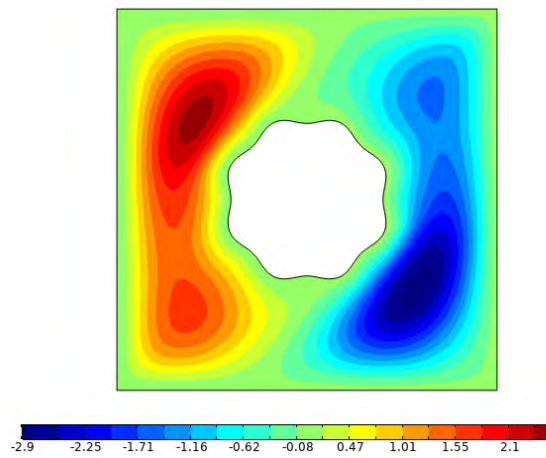
Figure 6.7: Streamlines (a-e) and Isotherms (b-f) variations with respect to Hartman number  $Ha$ .



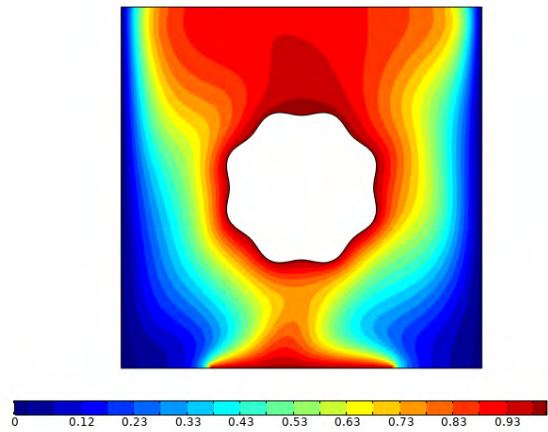
(a)  $\alpha = 0$



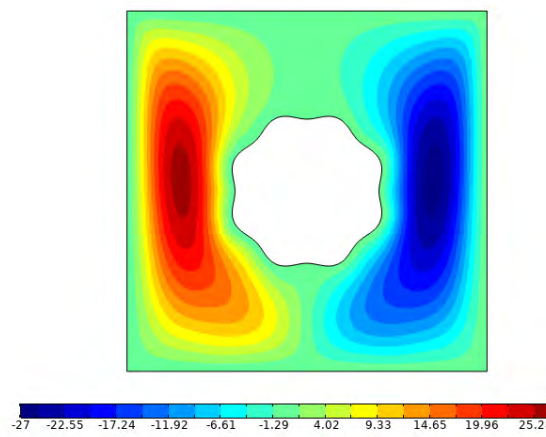
(b)  $\alpha = 0$



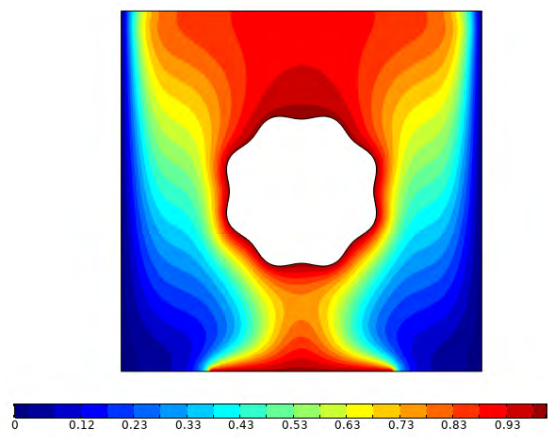
(c)  $\alpha = \frac{\pi}{4}$



(d)  $\alpha = \frac{\pi}{4}$



(e)  $\alpha = \frac{\pi}{2}$



(f)  $\alpha = \frac{\pi}{2}$

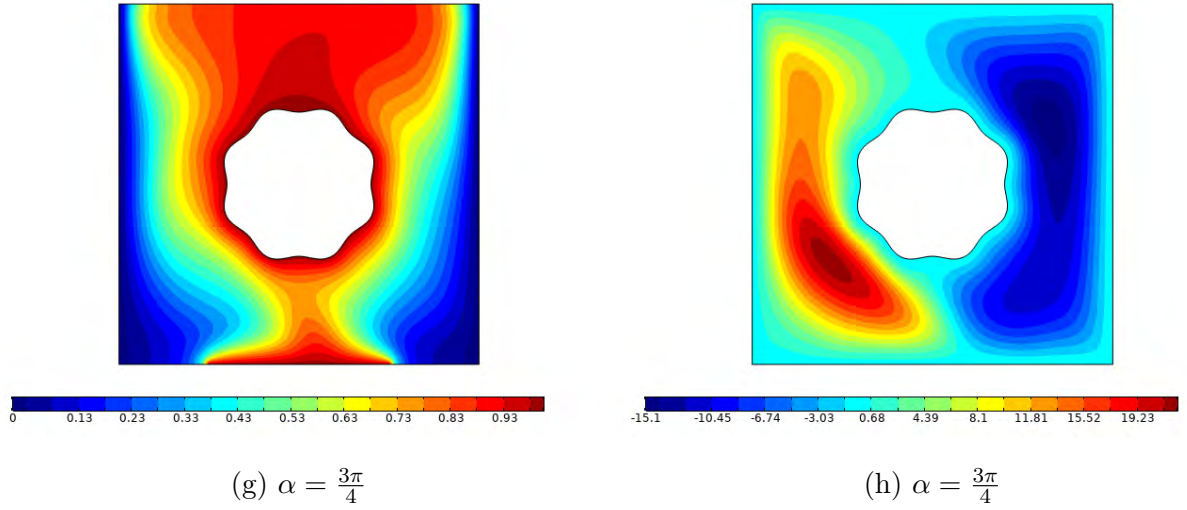
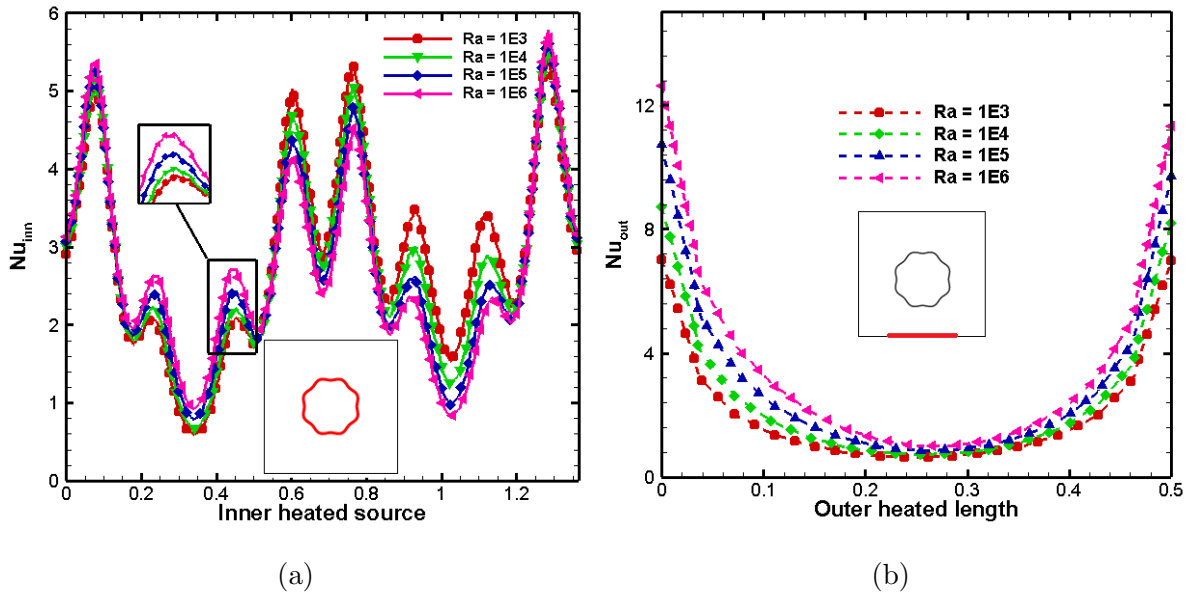
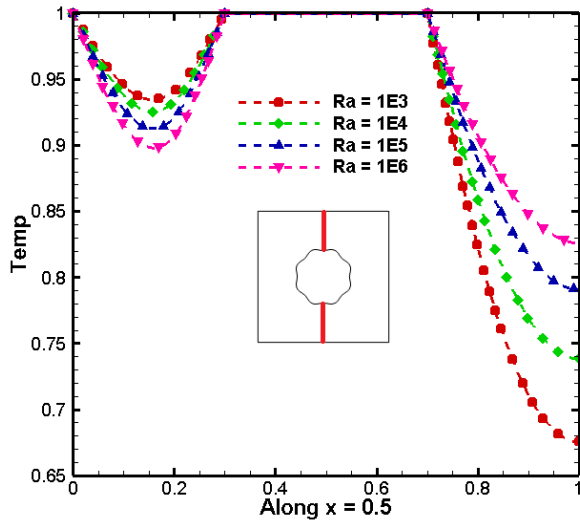
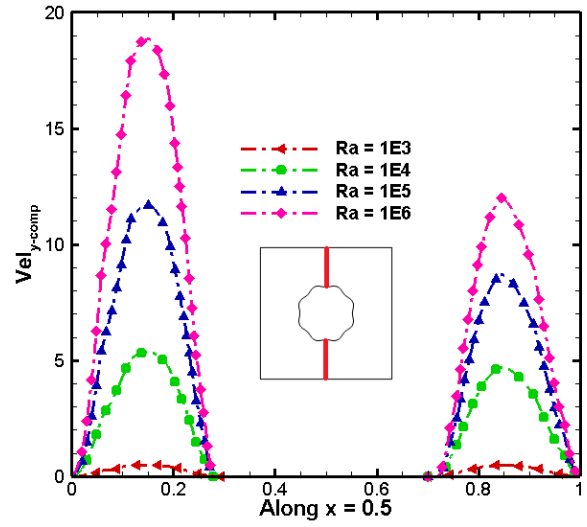


Figure 6.8: Variation in Streamlines (a-g) and Isotherms (b-h) at different inclination angle  $\alpha$ .



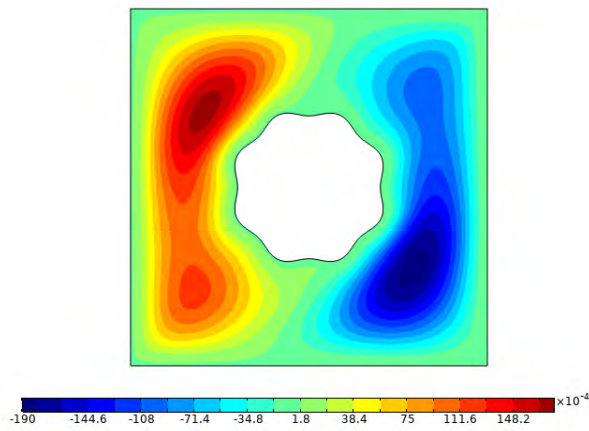


(c)

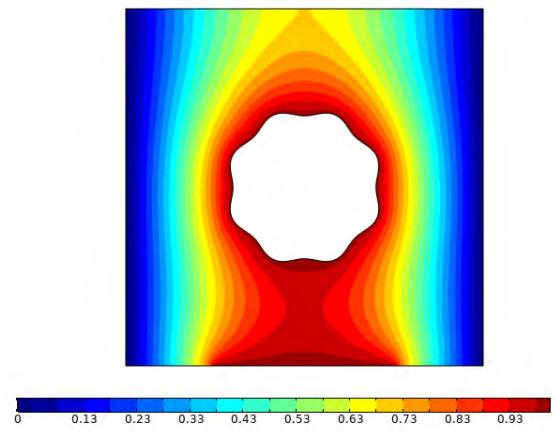


(d)

Figure 6.9: Impact of Raleigh number on (a, b) heat transfer rate, (c) temperature and (d)  $y$ -velocity at indicated paths.



(a)  $Ra = 10^3$



(b)  $Ra = 10^3$

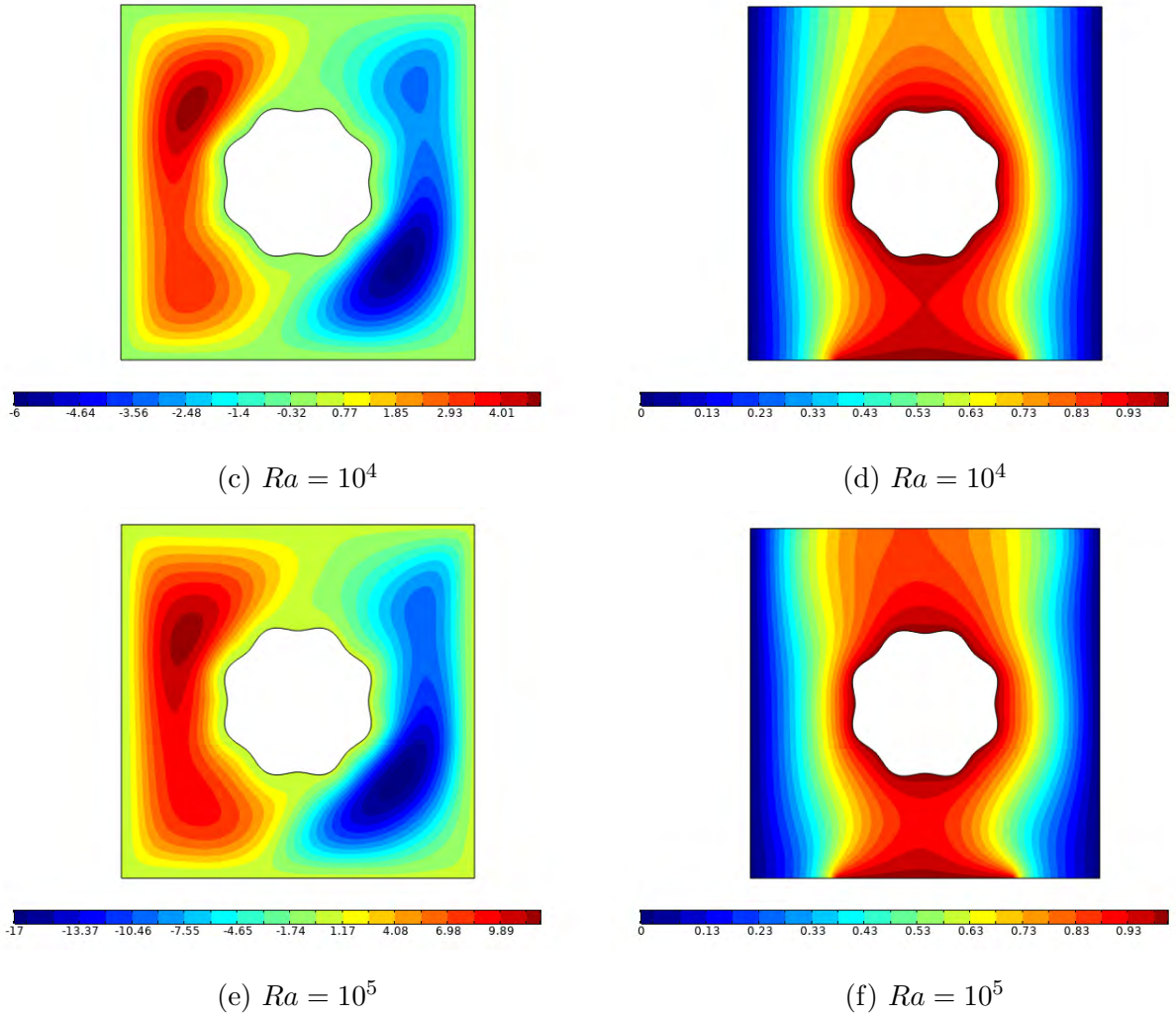


Figure 6.10: Influence of  $Ra$  on Streamlines (a-e) and Isotherms (b-f).

## 6.4 Concluding remarks

Finite element simulation is performed to examine the flow problem arising from a physical system which contain an enclosure filled with nanofluid. The free-convective flow situation occurs due to the presence of core-heated element influenced by oblique magnetic forces. Some physical parameters involved in the flow dynamics which control the thermal and flow configuration. Interesting results are obtained (1D-linegraphs and contour maps) against element undulation, particle fraction, Hart-

mann number and Rayleigh parameter. The key findings are concluded as:

- Nanoparticles addition rarefies the flow profile while the thermal transmission improves.
- Increasing undulation of heated element heat transport rate has higher values whereas, the flow field reduces.
- The flow distribution is suppressed by the applied magnetic force however the Nusselt number escalates.
- The orientation of the isolines (streamlines and isotherms) changes at various inclination angle of the applied magnetic force.
- At higher Rayleigh parameter not only the heat transportation rates shoot up the flow distribution also rises because of the stronger buoyancy regime.
- The free-convective regime is maintain presented by isolines at various improving  $Ra$ .

# Chapter 7

## Forced convection of rotating cylinder in nanofluid filled vented porous parallelogram enclosure

### 7.1 Introduction

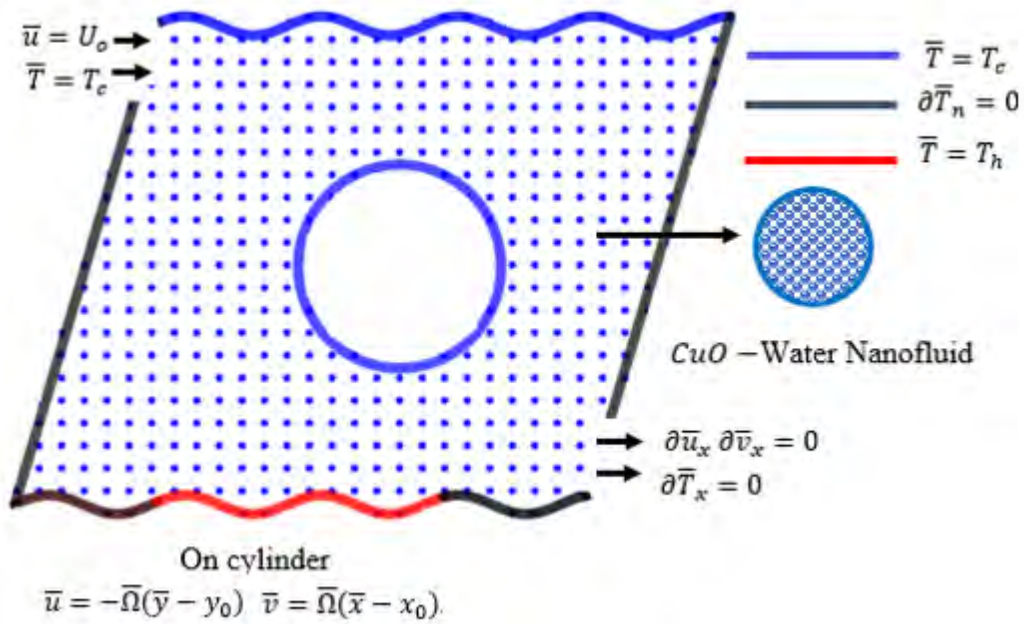
Flows confined in enclosure with rotating object have practical applications and great importance in various engineering and industrial aspects, for instant, in the centrifugally-driven separation processes, electrochemical cells, chemical reactors, tribology, in the production of oil and gas, hydraulic equipment and fluid viscometers etc. Understanding the mixed convective flow situation in an enclosure with sinusoidal horizontal walls and with rotating cylinder in a vertically-oriented annular gap whose outer wall is stationary while the inner wall rotates is a topic of great significance within the broader scope of fluid flows. Forced convection of  $CuO$  nanofluid in porous parallelogram cavity having inlet and outlet ports is analyzed here in this chapter. Flow and thermal distributions are influenced by porous media and  $CuO$  nanoparticles. Force convection in an enclosure is developed by external cold fluid

inflow and rotating cylinder. Partially heated corrugated wall at the bottom of cavity maintain free convection. Moreover, upper corrugated wall is cold, while the remaining walls of the enclosure are taken to be insulated. This physical model is converted into partial differential equations and solution of these equations are attained through finite element method. The outcomes are presented in terms of Nusselt number, line graphs and contour maps.

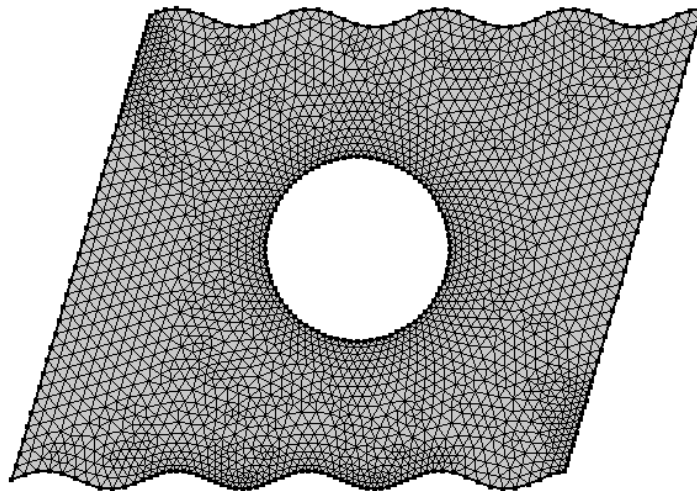
## 7.2 Physical model and governing equations

Consider the steady flow of  $CuO$ -water nanofluid in a partially heated parallelogram enclosure. Rotating cylinder is placed at the center of enclosure with constant temperature  $T_c$ . Inflow opening is placed at the top left corner of the enclosure and inflow fluid is assumed to be cold. Outlet port is placed at the bottom left corner of the enclosure. The vertical walls of enclosure are insulated. Lower corrugated wall of the enclosure has a constant temperature  $T_h$ . Figure 7.1(a) displays the geometry of the problem. Triangular mesh distribution of the physical domain is exhibited in figure 7.1(b).





(a)



(b)

Figure 7.1: Physical model and (b) Mesh distribution of domain.

The considered flow problem is influenced by porous medium resistance and particles concentration as well. Base fluid and nanoparticles are assumed to be in thermal

equilibrium. Under these considerations given problem obeys the following conservation laws:

$$\frac{\partial \bar{u}}{\partial \bar{x}} + \frac{\partial \bar{v}}{\partial \bar{y}} = 0, \quad (7.2.1)$$

$$\bar{u} \frac{\partial \bar{u}}{\partial \bar{x}} + \bar{v} \frac{\partial \bar{u}}{\partial \bar{y}} = -\frac{1}{\rho_{nf}} \frac{\partial \bar{p}}{\partial \bar{x}} + \nu_{nf} \left( \frac{\partial^2 \bar{u}}{\partial \bar{x}^2} + \frac{\partial^2 \bar{u}}{\partial \bar{y}^2} \right) - \frac{\nu_{nf}}{K_p} \bar{u}, \quad (7.2.2)$$

$$\bar{u} \frac{\partial \bar{v}}{\partial \bar{x}} + \bar{v} \frac{\partial \bar{v}}{\partial \bar{y}} = -\frac{1}{\rho_{nf}} \frac{\partial \bar{p}}{\partial \bar{y}} + \nu_{nf} \left( \frac{\partial^2 \bar{v}}{\partial \bar{x}^2} + \frac{\partial^2 \bar{v}}{\partial \bar{y}^2} \right) + \frac{(\rho\beta)_{nf}}{\rho_{nf}} g(\bar{T} - T_C) - \frac{\nu_{nf}}{K_p} \bar{v}, \quad (7.2.3)$$

$$\bar{u} \frac{\partial \bar{T}}{\partial \bar{x}} + \bar{v} \frac{\partial \bar{T}}{\partial \bar{y}} = \frac{k_{nf}}{(\rho C_p)_{nf}} \left( \frac{\partial^2 \bar{T}}{\partial \bar{x}^2} + \frac{\partial^2 \bar{T}}{\partial \bar{y}^2} \right). \quad (7.2.4)$$

With the associated boundary conditions for parallelogram enclosure are given as:

Temperature at left and right walls

$$\begin{cases} \frac{\partial \bar{T}}{\partial \bar{x}} = 0, & \text{at } 0.0 \leq \bar{y} \leq l, \bar{x} = 0.0, \\ \frac{\partial \bar{T}}{\partial \bar{x}} = 0, & \text{at } 0.0 \leq \bar{y} \leq l, \bar{x} = \frac{15l}{10}. \end{cases} \quad (7.2.5)$$

Temperature at upper wall

$$\begin{cases} \bar{T} = T_c, & \text{at } \bar{y} = \lambda \sin\left(\frac{\omega\pi}{l}\bar{x}\right), \frac{3l}{10} \leq \bar{x} \leq \frac{5l}{10}. \end{cases} \quad (7.2.6)$$

Temperature at lower wall

$$\begin{cases} \frac{\partial \bar{T}}{\partial \bar{y}} = 0, & \text{at } \bar{y} = \lambda \sin\left(\frac{\omega\pi}{l}\bar{x}\right), 0.0 \leq \bar{x} \leq \frac{3l}{10}, \\ \frac{\partial \bar{T}}{\partial \bar{y}} = 0, & \text{at } \bar{y} = \lambda \sin\left(\frac{\omega\pi}{l}\bar{x}\right), \frac{9l}{10} \leq \bar{x} \leq \frac{12l}{10}, \end{cases} \quad (7.2.7)$$

and

$$\begin{cases} \bar{T} = T_h, & \text{at } \bar{y} = \lambda \sin\left(\frac{\omega\pi}{l}\bar{x}\right), \frac{3l}{10} \leq \bar{x} \leq \frac{9l}{10}. \end{cases} \quad (7.2.8)$$

At inlet

$$\bar{T} = T_c, \quad \bar{u} = U_o, \quad \bar{v} = 0 \quad \text{at} \quad \frac{8l}{10} \leq \bar{y} \leq l, \bar{x} = 0. \quad (7.2.9)$$

At outlet

$$\frac{\partial \bar{T}}{\partial \bar{x}} = 0, \quad \bar{u} = 0, \quad \bar{v} = 0 \quad \text{at} \quad 0 \leq \bar{y} \leq \frac{2l}{10}, \bar{x} = \frac{15l}{10}. \quad (7.2.10)$$

At cylinder

$$\bar{T} = T_c, \quad \bar{u} = -\bar{\Omega}(\bar{y} - \bar{y}_0), \quad \bar{v} = \bar{\Omega}(\bar{x} - \bar{x}_0). \quad (7.2.11)$$

Velocity at remaining walls

$$\bar{u} = 0, \quad \bar{v} = 0. \quad (7.2.12)$$

Here  $(x, y)$  components of fluid's velocity are  $(\bar{u}, \bar{v})$  and  $\bar{T}$  denotes the temperature.  $k_{nf}$ ,  $(\rho C_p)_{nf}$ ,  $(\rho\beta)_{nf}$ ,  $\nu_{nf}$ ,  $\rho_{nf}$  represents thermal conductivity, heat capacitance, thermal expansion coefficient, kinematic viscosity and effective density of the nanofluid. Whereas, temperature at cooled and heated boundaries are  $T_c$  and  $T_h$ .  $\Omega$  is the rotational velocity of the cylinder. Koo–Kleinstreuer–Li defines thermal conductivity and dynamic viscosity as [56–58].

$$k_{nf} = k_{static} + k_{Brownian}.$$

Maxwell defined  $k_{static}$  as

$$k_{static} = k_f \left( 1 + \frac{3 \left( \frac{k_s}{k_f} - 1 \right) \phi}{\left( \frac{k_s}{k_f} + 2 \right) - \left( \frac{k_s}{k_f} - 1 \right) \phi} \right).$$

Dynamic part is represented as

$$k_{Brownian} = 5 \times 10^4 \phi (\rho C_p)_f \sqrt{\frac{K_b T_0}{\rho_s D_s}} f(T_0, \phi).$$

Here,  $D_s$ ,  $T_0$  ( $= \frac{1}{2}(T_h - T_c)$ ),  $K_b$  ( $= 1.38 \times 10^{-23}$ ) are diameter of nanoparticles, average temperature and Boltzmann constant while  $f(T_0, \phi)$  is expressed as

$$f(T_0, \phi) = 0.011(100\phi)^{-0.7272} \{ (-6.04\phi + 0.4705) T_0 + (1722.3\phi - 134.63) \}. \quad (7.2.13)$$

Viscosity due to Brownian motion is expressed as

$$\mu_{nf} = \mu_{static} + \mu_{Brownian} = \frac{\mu_f}{(1 - \phi)^{2.5}} + \frac{k_{Brownian} \mu_f}{k_f \text{Pr}},$$

Remaining thermodynamic properties are expressed by [73].

$$\begin{aligned}
\rho_{nf} &= (1 - \phi)\rho_f + \phi\rho_s, \\
(\rho C_p)_{nf} &= (1 - \phi)(\rho C_p)_f + \phi(\rho C_p)_s, \\
(\rho\beta)_{nf} &= (1 - \phi)(\rho\beta)_f + \phi(\rho\beta)_s.
\end{aligned} \tag{7.2.14}$$

Defining the non-dimensional variables as [74, 75].

$$\begin{aligned}
X &= \frac{\bar{x}}{l}, \quad Y = \frac{\bar{y}}{l}, \quad U = \frac{\bar{u}}{U_o}, \quad V = \frac{\bar{v}}{U_o}, \quad T = \frac{\bar{T} - T_c}{T_h - T_c}, \\
P &= \frac{\bar{P}}{\rho_f U_o^2}, \quad Da = \frac{K_p}{l^2}, \quad Re = \frac{U_o l}{\nu_f}, \quad Pr = \frac{\nu_f}{\alpha_f}, \quad \Omega = \frac{l}{U_o} \bar{\Omega}.
\end{aligned} \tag{7.2.15}$$

By using these variables the governing equations (7.2.2)-(7.2.4) with boundary conditions (7.2.5) to (7.2.12) reduce to non dimensional form as follows

$$U \frac{\partial U}{\partial X} + V \frac{\partial U}{\partial Y} = 0, \tag{7.2.16}$$

$$U \frac{\partial U}{\partial X} + V \frac{\partial U}{\partial Y} = -A \frac{\partial P}{\partial X} + \frac{B}{Re} \left( \frac{\partial^2 U}{\partial X^2} + \frac{\partial^2 U}{\partial Y^2} \right) - U \frac{B}{Re Da}, \tag{7.2.17}$$

$$U \frac{\partial V}{\partial X} + V \frac{\partial V}{\partial Y} = -A \frac{\partial P}{\partial Y} + \frac{B}{Re} \left( \frac{\partial^2 V}{\partial X^2} + \frac{\partial^2 V}{\partial Y^2} \right) + CT \frac{Gr}{Re^2} - V \frac{B}{Re Da}, \tag{7.2.18}$$

$$U \frac{\partial T}{\partial X} + V \frac{\partial T}{\partial Y} = \frac{D}{Pr Re} \left( \frac{\partial^2 T}{\partial X^2} + \frac{\partial^2 T}{\partial Y^2} \right). \tag{7.2.19}$$

Temperature at both vertical walls

$$\left. \begin{aligned}
0.0 \leq Y \leq 1.0, \quad X = 0.0 \\
0.0 \leq Y \leq 1.0, \quad X = 1.5
\end{aligned} \right\} \frac{\partial T}{\partial X} = 0. \tag{7.2.20}$$

Temperature at upper wall

$$Y = A_m \sin(\omega\pi X), \quad 0.3 \leq X \leq 1.5 \} T = 0. \tag{7.2.21}$$

Temperature at lower wall

$$\left. \begin{aligned}
Y = A_m \sin(\omega\pi X), \quad 0.0 \leq X \leq 0.3 \\
Y = A_m \sin(\omega\pi X), \quad 0.9 \leq X \leq 1.2
\end{aligned} \right\} \frac{\partial T}{\partial Y} = 0. \tag{7.2.22}$$

and

$$Y = A_m \sin(\omega\pi X), \quad 0.3 \leq X \leq 0.9 \} T = 1. \quad (7.2.23)$$

At inlet

$$U = 1, V = 0, \quad 0.8 \leq Y \leq 1, X = 0.0 \} T = 0. \quad (7.2.24)$$

At outlet

$$U = 0, V = 0, \quad 0.0 \leq Y \leq 0.2, X = 1.5 \} \frac{\partial T}{\partial X} = 0. \quad (7.2.25)$$

At cylinder

$$U = -\Omega(Y - Y_0), \quad V = \Omega(X - X_0) \} T = 0. \quad (7.2.26)$$

Velocity at remaining walls

$$U = V = 0. \quad (7.2.27)$$

Dimensionless physical parameters in the above equations are denoted as

$$A = \frac{\rho_f}{\rho_{nf}}, \quad B = \frac{A}{(1 - \phi)^{2.5}} + \frac{A \times k_{Brownian}}{\text{Pr } k_f}, \quad (7.2.28)$$

$$D = \frac{(\rho C_p)_f}{(\rho C_p)_{nf}} + \frac{(\rho C_p)_f}{(\rho C_p)_{nf}} \left( \frac{k_{static}}{k_f} - 1 \right) + \frac{(\rho C_p)_f}{(\rho C_p)_{nf}} \frac{k_{Brownian}}{k_f}, \quad (7.2.29)$$

$$C = A \left( 1 - \phi + \phi \frac{(\rho\beta)_s}{(\rho\beta)_f} \right), \quad A_m = \frac{\lambda}{l}. \quad (7.2.30)$$

Where  $A, B, C$  and  $D$  are dimensionless thermophysical parameters.

Heat transfer along the heated lower corrugated wall of the enclosure can be defined as

$$Nu = -\frac{k_{nf}}{k_f} \frac{\partial \theta}{\partial Y} \Big|_{wall} \quad Nu_m = \int_s Nuds. \quad (7.2.31)$$

Here  $s$  represents the heated surface of the enclosure.

### 7.3 Results and discussion

Forced convection heat transfer inside a parallelogram cavity filled with CuO-water nanofluid is examined here. The enclosure is partially heated at the bottom. The flow and heat transfer regimes are influenced by bottom heating, rotating cylinder, inflow and outflow. The finite element method is adopted to attain the solution of governing PDEs. Temperature field has been examined in terms of isotherms and temperature profiles for the horizontal mean position while the flow field has been examined in terms of streamlines within the fluid domain and velocity profiles for a horizontal mean position respectively. Furthermore, the average Nusselt number has been considered to calculate the heat transfer along the heated corrugated wall of the cavity. Consequences of this study have been illustrated graphically in figures 7.2-7.9, respectively. The outcomes for various ranges ([89]) of  $Ri$  ( $10^{-2}$  to  $10^2$ ),  $Da$  ( $10^{-3}$  to  $10^{-1}$ ),  $\phi$  (0.0 to 0.2) and  $\Omega$  ( $-50$  to  $50$ ) are disclosed in the upcoming subsections.

Figures 7.2(a, b) demonstrate the line graphs of velocity and temperature for various values of Richardson number. It can be observed that, velocity profiles decline near inlet port, upraise in the velocity occurs due to the presence of rotating cylinder and then again velocity declines near the exit port. Moreover, the temperature line tends to increase because the thickness of thermal boundary layer getting stronger with the increase in  $Ri$ . This shows that with the rise in  $Ri$ , influence of forced convection declines and natural convection prevails in the enclosure. Another important property to consider is the heat transfer rate and its average value against thermally active portion is computed for various Grashof number. It is reported in figure 7.2(c) that average Nusselt number has maximum behavior at higher  $Gr$  and minimum values at lower  $Gr$ . This reveals that approaching to large Grashof number natural convection regime gets dominant. Figures 7.3(a – f) displays the streamlines and isotherms for various Richardson number while other parameters are kept fixed.

Richardson number is the ratio of free and forced convection i.e.,  $Ri = \frac{Gr}{Re^2}$ . At small values of Richardson number i.e., less than unity, forced convection prevails and it overcomes the natural convection. At  $Ri = 0.01$ , fluid enters the cavity from inlet port and creates a single vortex as portrayed in figure 7.3(a). Due to the dominance of shear force which is produced by the fluid inflow and rotation of the cylinder, entire fluid flows in an anticlockwise direction around rotating cylinder situated at the center of enclosure and then leaves the cavity from the outlet port. Because, at fixed  $Gr$ , small values of  $Ri$  implies large values of  $Re$  that augments the shear driving force and prompts forced convection. figure 7.3(b) illustrates that isotherms are crowded near the heated portion of the enclosure because of stronger force inflow and enhanced rotating speed at high Reynolds number. By increasing Richardson up to unity, forced convection turns to the mixed convection mode that is the combination of two effects. The first one is shear force, which produces from rotation of the cylinder and fluid inflow, while the second one is buoyancy force produces from temperature difference. Thus at  $Ri = 1$ , streamlines and isotherms are the result of interaction of free and forced convection as illustrated in figures 7.3(c, d). Further rise in Richardson number augments the buoyancy force, which promotes natural convection and the influence of forced convection declines. At  $Ri = 100$ , buoyancy force is prevailing as a result, clockwise vortex develops in the left bottom of the cavity. In addition, due to the weakening of cylinder's rotation some fluid flows over the cylinder towards outlet port (see figure 7.3(e)). Because at large values of  $Ri$ , buoyancy effect escalates and the influence of fluid inflow and cylinder's rotation is minimal due to low values of Reynolds number. On the other hand, figure 7.3(f) reveals that isotherms distribute in the whole cavity, since boundary layer thickness increases with the enhancement of buoyancy force. Line graphs of velocity and temperature for various Darcy numbers are exhibited in figures 7.4(a, b). With the enhancement of  $Da$  line graph of velocity along the horizontal mean position displays decreasing behavior near the inlet port

and increasing behavior near the outlet port. Temperature of the fluid rises with the rise in  $Da$  as portrays in figure 7.4(b). Since with the escalation of  $Da$ , solid matrix distance increases which eventually enhance fluid motion and strengthen the convection. In view of porous medium resistance average Nusselt number computed along heated wavy length is presented in figure 7.4(c). The displayed results confirm the above physically explained behavior that at maximum  $Da$  the convective heat transfer rate has maximum value and lower value at smaller  $Da$ . Since the resistance of porous medium is greater when the solid matrix gap is smaller. Thus along the thermal active portion the surface friction coefficient is greater at smaller  $Da$ , it is due to more viscous nature of flow profile. This influence of  $Da$  is presented in figure 7.4(d). The influence of various Darcy number on streamlines and isotherms for fixed  $Re = 10$ ,  $Gr = 1e3$ ,  $\phi = 0.1$  and  $\Omega = 50$  is portrayed in figures 7.5(a – f). Streamlines in figure 7.5(a) illustrates that at  $Da = 10^{-3}$ , flow circulation is weak, inflow fluid flows above and below the cylinder toward outlet port and small amount of fluid rotates around the cylinder (see figure 7.5(a)). Because at low values of Darcy number, permeability of porous media is less that offers more resistance and causes the porous matrix to cease the flow in a porous region as a result speed of the flow reduces. figure 7.5(b) depicts that isotherms are nearly parallel and less dense around the heated wall displaying that heat is transferred through conduction. Streamline in figure 7.5(c) reveals that as Darcy number increases to  $Da = 10^{-2}$ , resistance decreases and solid matrix distance increases as a result permeability of the porous media enhances and fluid flows easily through the pores. figure 7.5(d) portrays that isotherms are getting closer to the heated portion of the enclosure specifying that convection is prevailing. As Darcy number rises to  $Da = 10^{-1}$ , the strength of flow circulation increases and entire fluid circulates around the rotating cylinder that almost covers the whole enclosure as presented in the figure 7.5(e). Because high values of  $Da$ , upsurgs the permeability of porous media and solid matrix distance by weak-

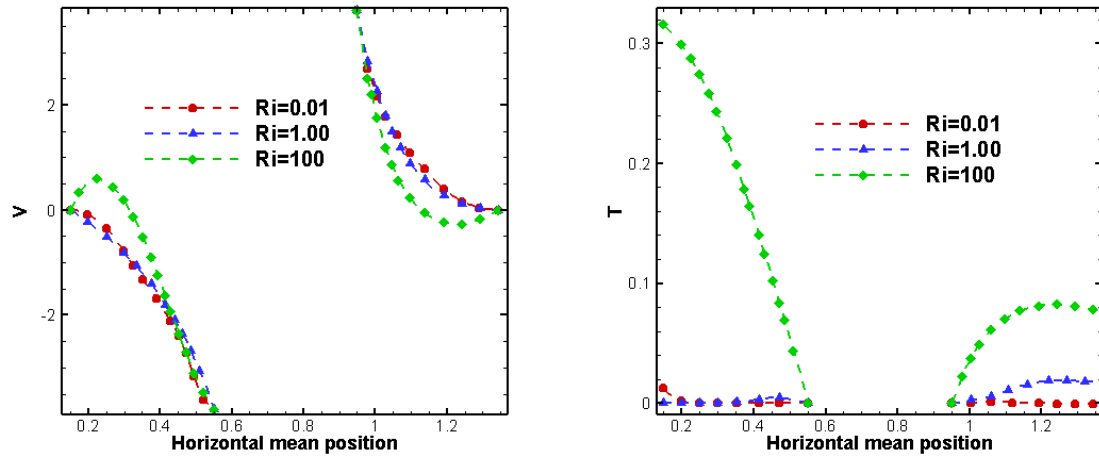


ening the resistance. Consequently strength of flow circulation intensifies and fluid travels through the pores easily. Isotherms are moving closer to the heated wall of the cavity as illustrated in figure 7.5(*f*) because with the increase in permeability of porous media heat is transported through convection for large values of Darcy number.

The outcomes for velocity and temperature against various  $\phi$  along horizontal mean position is presented in figures 7.6(*a, b*). With augmentation in the values of  $\phi$  both velocity and temperature profiles declines near the inlet port and rises near the outlet port. Since, escalation in the thermal conductivity with the addition of nanoparticles leads to an intensification in the heat transfer rate. Thus it is depicted in figure 7.6(*c*) average Nusselt number has augmented behavior against higher particle concentration and being the property of nanoparticles the heat transfer rate escalates versus its maximum volume concentration. Figures 7.7(*a–f*) demonstrates streamline and isotherms for various nanofluid solid volume fractions. figure 7.7(*a*) depicts that at  $\phi = 0$ , two clockwise circulations are established at the bottom of the cavity. Small amount of fluid flows around rotating cylinder in anticlockwise direction and maximum fluid flows above the cylinder towards the outlet port. At  $\phi = 0.1$ , right circulation vanishes and the size of left circulation reduces as presented in figure 7.7(*c*). Flow circulations decline with enhancing volume fraction since, higher concentration of nanoparticles into base fluid upsurges the fluid viscosity, that slows down the flow movement. At  $\phi = 0.2$  all secondary circulations vanish and entire cavity is covered with single anticlockwise circulation (see figure 7.7(*e*)). Since addition of nanofluid to the base fluid causes declination in velocity of the flow inside the enclosure. figure 7.7(*b*) depicts that at  $\phi = 0$ , isotherms are almost steep near the heated wall of the cavity. With the increase in volume fraction up to  $\phi = 0.2$  isotherms turn out to be parallel along the heated wall (see figure 7.7(*f*)). Isotherms reveals that with the increases in volume fraction mode of heat transfer varies from convection towards

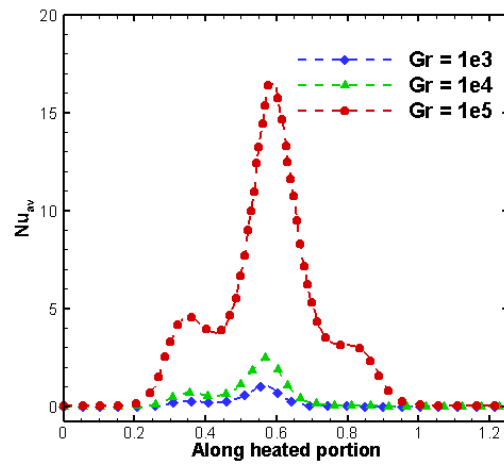
conduction. Hence, with the enhancement of volume fraction conduction mode of heat transfer is prevailing that upsurges the thermal conductivity of the working fluid. Figures 7.8(*a – d*) exhibits the impact of rotation in anticlockwise and clockwise direction on temperature and velocity in terms of Line graph. When cylinder is rotating in an anticlockwise direction, velocity of the fluid at inflow is greater than outflow but in clockwise direction, velocity of fluid at outflow is greater than inflow as given in figures 7.8(*a, c*). In anticlockwise rotation, direction of the cylinder is opposite to the flow direction that produce fluctuations in temperature value but in clockwise rotation, direction of cylinder is same to the flow direction that enhances temperature value as depicted in figures 7.8(*b, d*). Since cylinder rotation has considerable impact on flow situation thus it is important to compute the average skin friction coefficient along the rotating body as well. The evaluated result against  $\Omega$  is presented in figures 7.8(*e, f*). As shown that the average drag coefficient has smaller values at lower  $\Omega$  and higher at maximum rotation. This behavior is because when the cylinder rotates at slower speed (i.e.,  $\Omega = 10$ ) it provide smaller resistance to the inflow fluid. Whereas, at faster cylinder rotation the in-flow is faced by strong resistance because when the inflow comes in contact with the faster rotating cylinder it is pushed back. That's why the average surface friction is higher at large rotating speed  $\Omega$ . The impact of the direction of rotating cylinder in terms of streamlines and isotherms is illustrated in figures 7.9(*a – j*). It can be observed from figure 7.9(*a*) that when cylinder is static i.e., at  $\Omega = 0$  flow field configurations are the consequence of inflow and temperature difference. Cold fluid spreads in the enclosure through inlet port situated at the top of left wall. In this case, cylinder acts as cold obstacle situated at the center of cavity thus fluid moves transversely downward and leave the cavity through outlet port situated at the bottom of right wall. Temperature difference give rise to buoyancy force, which produces clockwise circulation underneath the stationary cylinder. figure 7.9(*b*) exhibits that isotherms are prevailing in the wider region of the enclosure when

cylinder is stationary, which reveals that buoyancy effect is controlling as compared to shear driving effect. At  $\Omega = 10$ , flow configurations are established because of shear force (that is produced by combine effect of fluid inflow and cylinder rotation) and buoyancy force (that is produced by temperature difference). When cylinder is rotating in an anticlockwise direction, it opposes the direction of fluid inflow thus less fluid pass above the cylinder and direction of most of the fluid changes and it flows beneath the cylinder to reach the outlet port. Circulation shown up at the left bottom of the enclosure in the motionless cylinder case reduces in size due to the diminution of buoyancy force as presented in figure 7.9(c). Increased cylindrical rotation has suppressed the isotherms due to the enhancement of shear force as depicts in figure 7.9(d). At  $\Omega = -10$  cylinder is rotating in clockwise direction, it aids the direction of fluid inflow, most of the fluid flows above the cylinder towards the outlet port, and isotherms spread in the wider region of the enclosure as depicts in figure 7.9(e). The impact of rotating cylinder is enhanced at high values of rotational speed i.e., at  $\Omega = 50$ . In case of anticlockwise rotation, all fluid flow beneath the cylinder and reaches the outlet port as displays in figure 7.9(g). At  $\Omega = -50$  cylinder is rotating in an anticlockwise direction, rotating cylinder pushes all inflow fluid above the cylinder toward the outlet port as portrayed in figure 7.9(i). In both cases, single vortex is formed by the rotation of cylinder that encompasses almost entire enclosure due the enhancement of shear force. Isotherms compressed towards the heated surface in anticlockwise rotation as shown in figure 7.9(h). Clockwise rotation spreads the isotherms in the entire enclosure as revealed in figure 7.9(j).



(a)

(b)



(c)

Figure 7.2: Influence of  $Ri$  on  $V$ ,  $T$  and  $Nu_{av}$  in ((a), (b)) and (c) along horizontal mean position and heated portion.

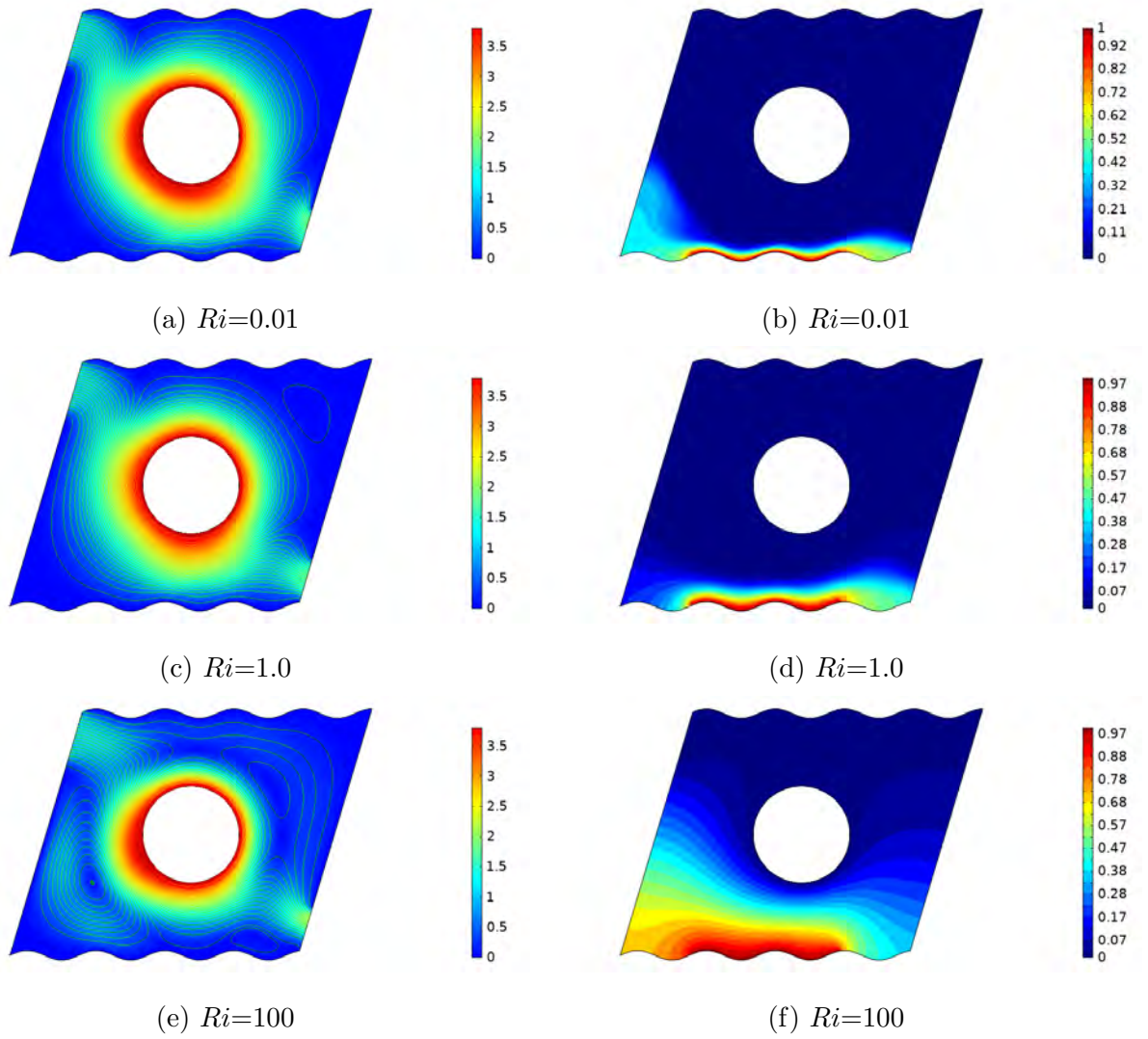
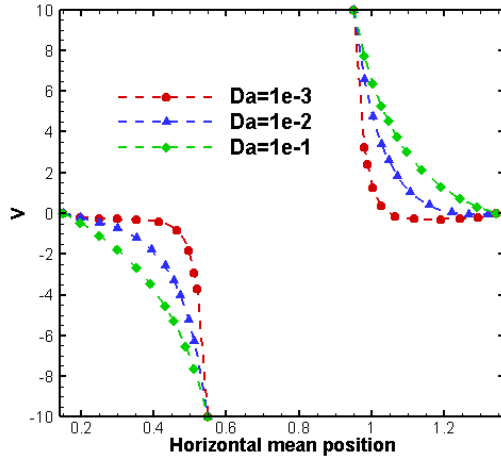
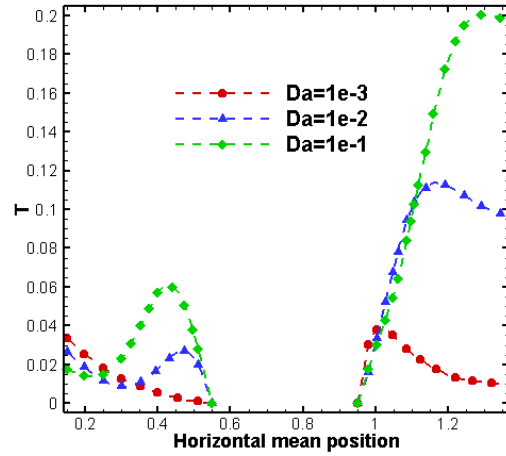


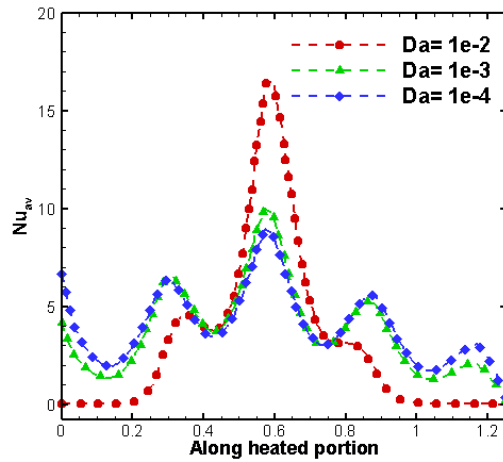
Figure 7.3: Streamlines (left) and Isotherms (right) at various Richardson number  $Ri$



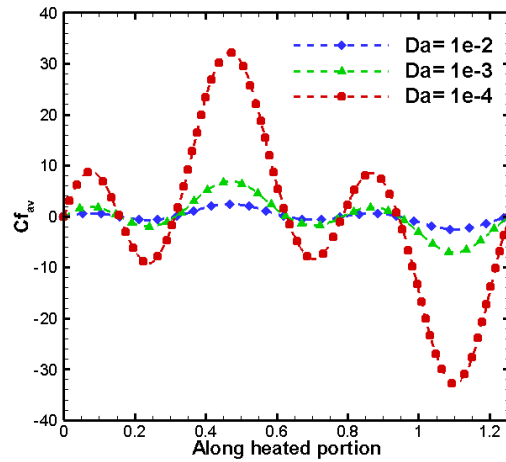
(a)



(b)



(c)



(d)

Figure 7.4: Influence of  $Da$  on  $V$  and  $T$  in ((a), (b)) along horizontal mean position and  $Nu_{av}$  and  $Cf_{av}$  in ((c), (d)) against heated portion.

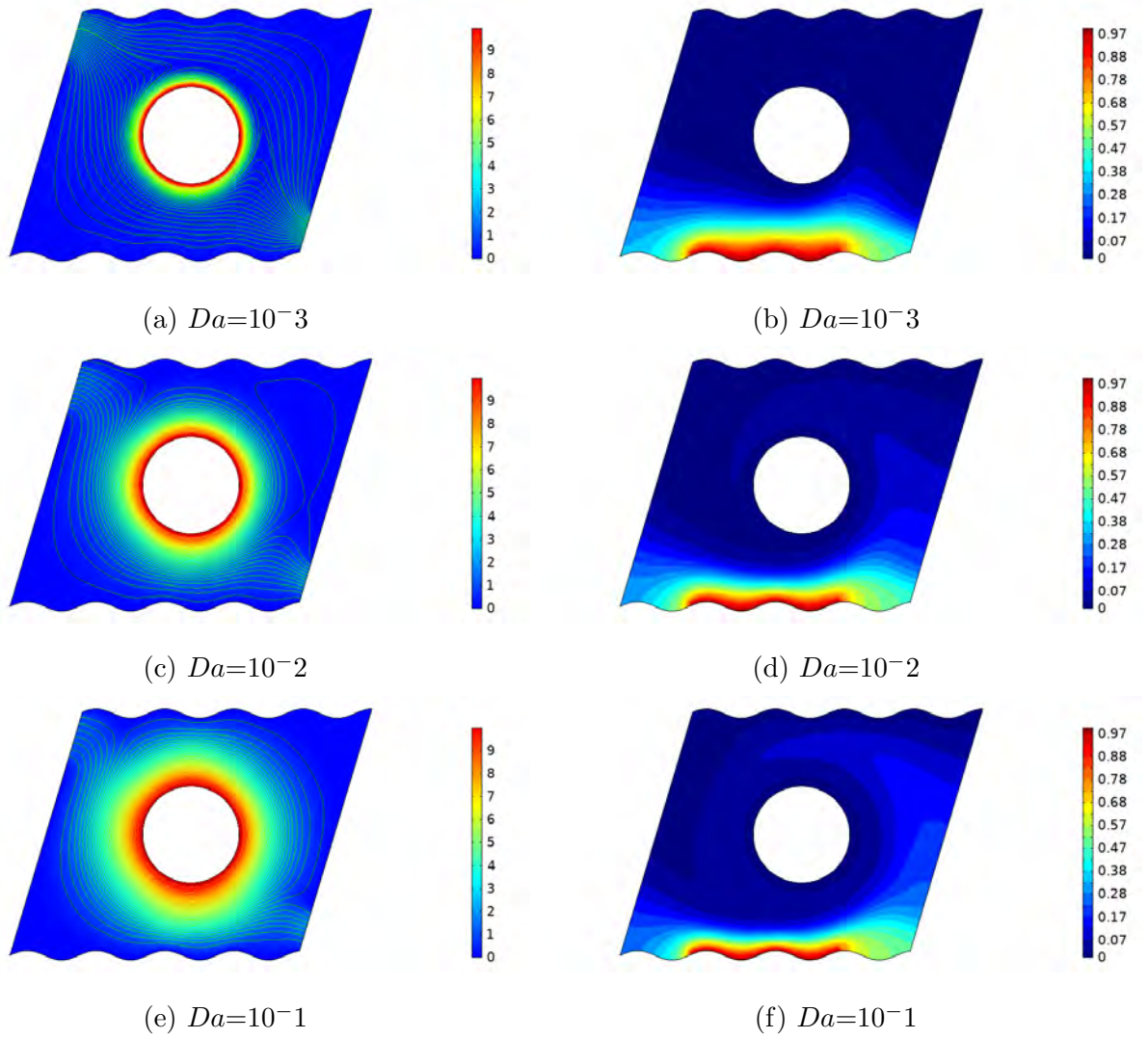
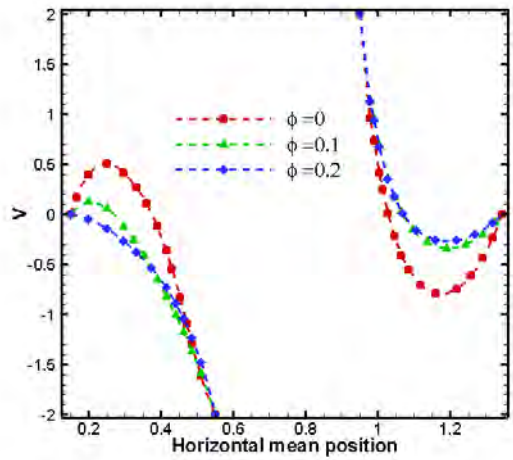
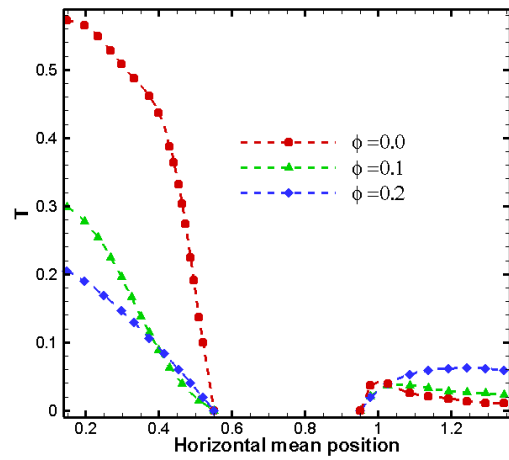


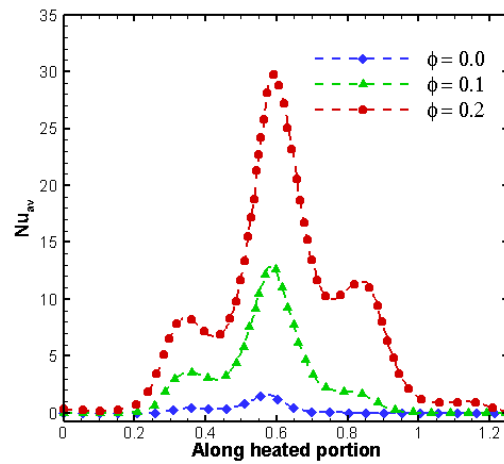
Figure 7.5: Streamlines (left) and Isotherms (right) at various Darcy number  $Da$



(a)



(b)



(c)

Figure 7.6: Influence of  $\phi$  on  $V$ ,  $T$  and  $Nu_{av}$  in ((a), (b)) and (c) along horizontal mean position and heated portion.



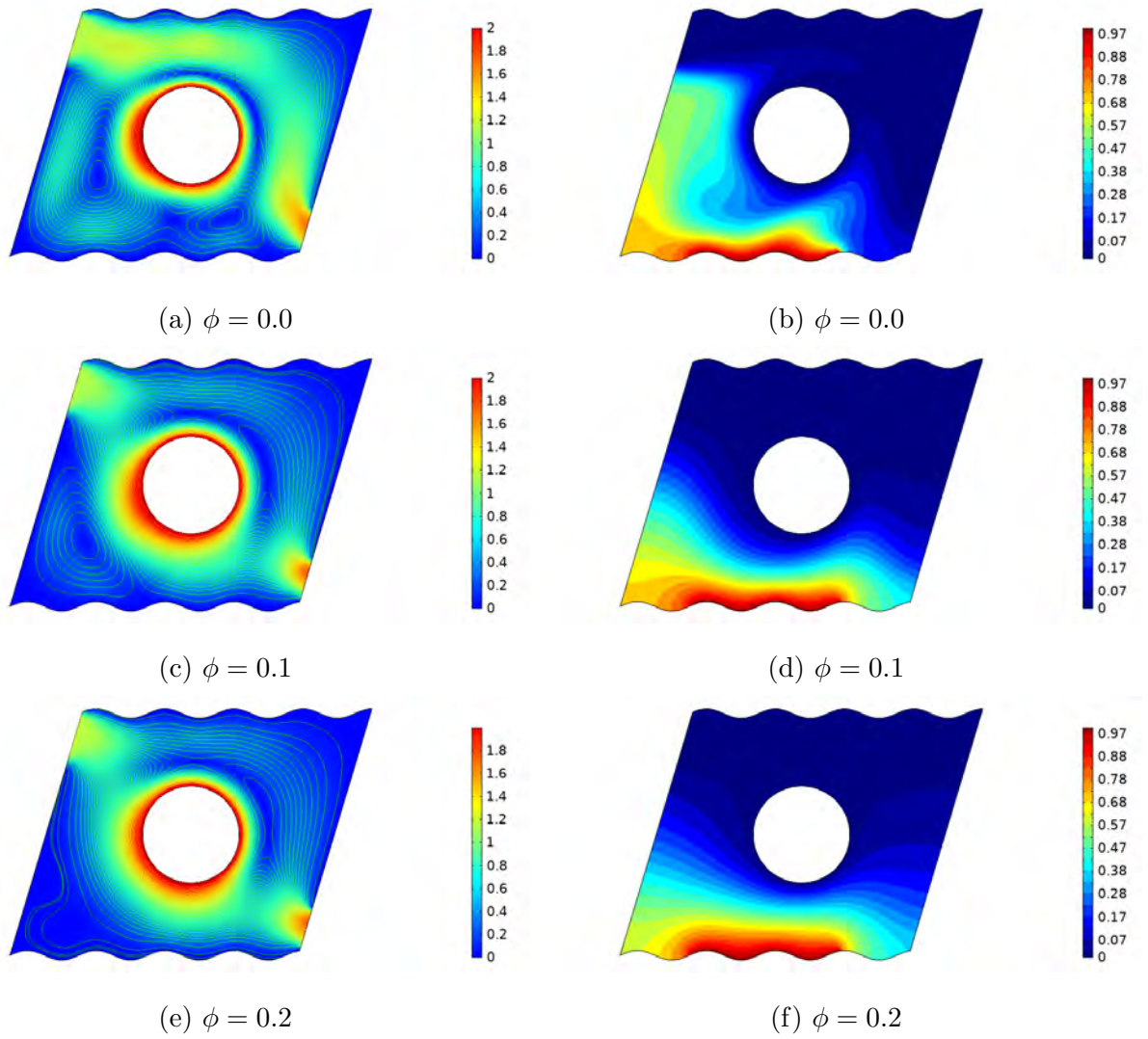
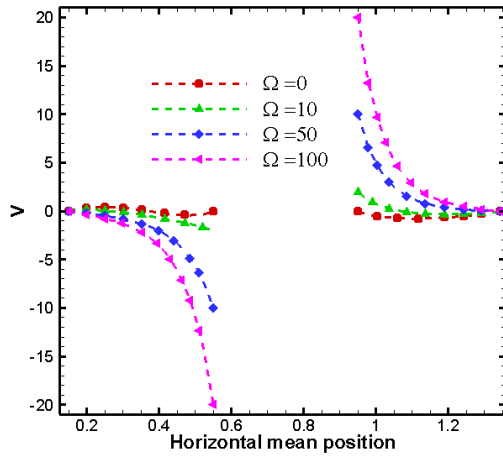
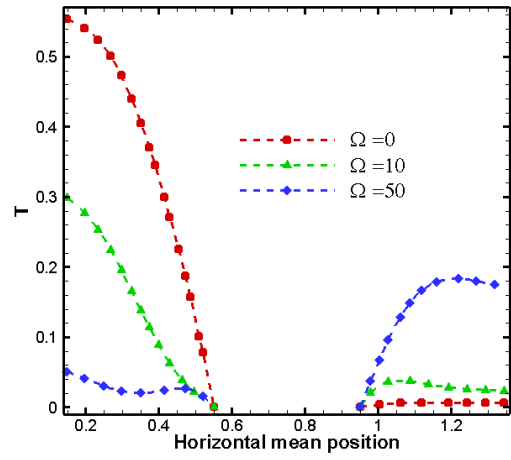


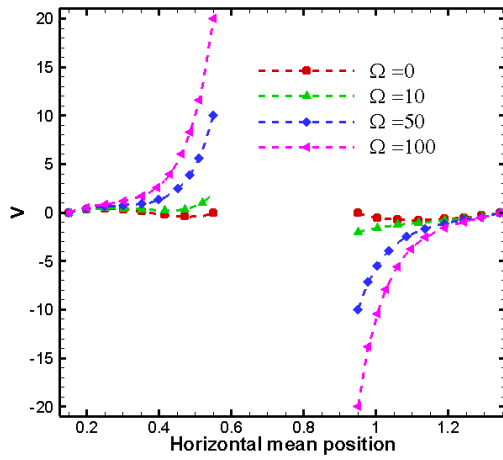
Figure 7.7: Streamlines (left) and Isotherms (right) at various volume fractions  $\phi$



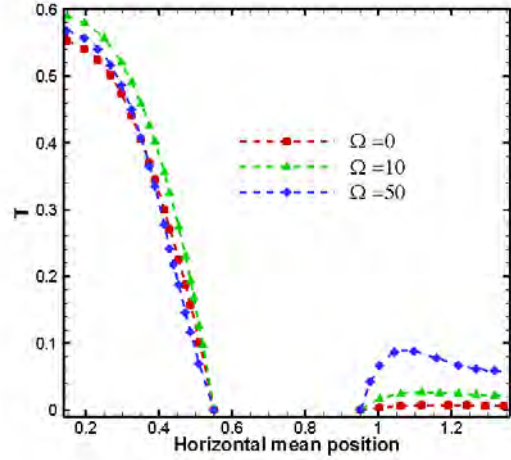
(a)



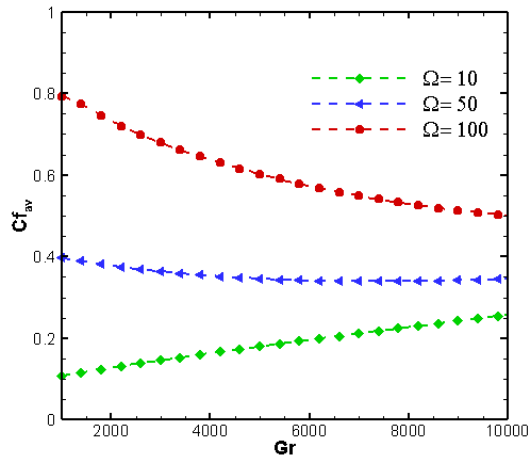
(b)



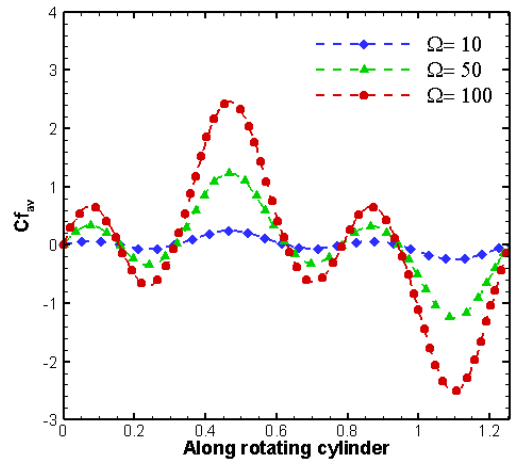
(c)



(d)

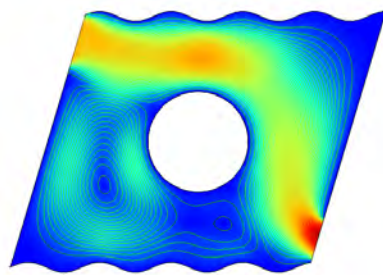


(e)

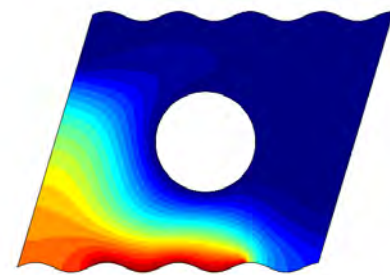


(f)

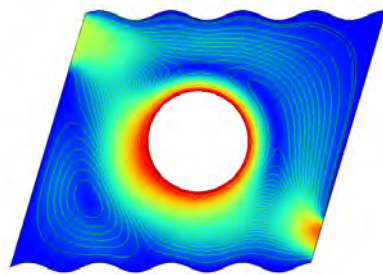
Figure 7.8: Influence of  $\Omega$  on  $V$ ,  $T$  and  $Cf_{av}$  in anticlockwise ((a), (b), (e), (f)) and clockwise directions ((c), (d)).



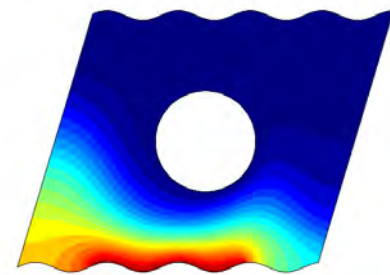
(a)  $\Omega = 0$



(b)  $\Omega = 0$



(c)  $\Omega = 10$



(d)  $\Omega = 10$

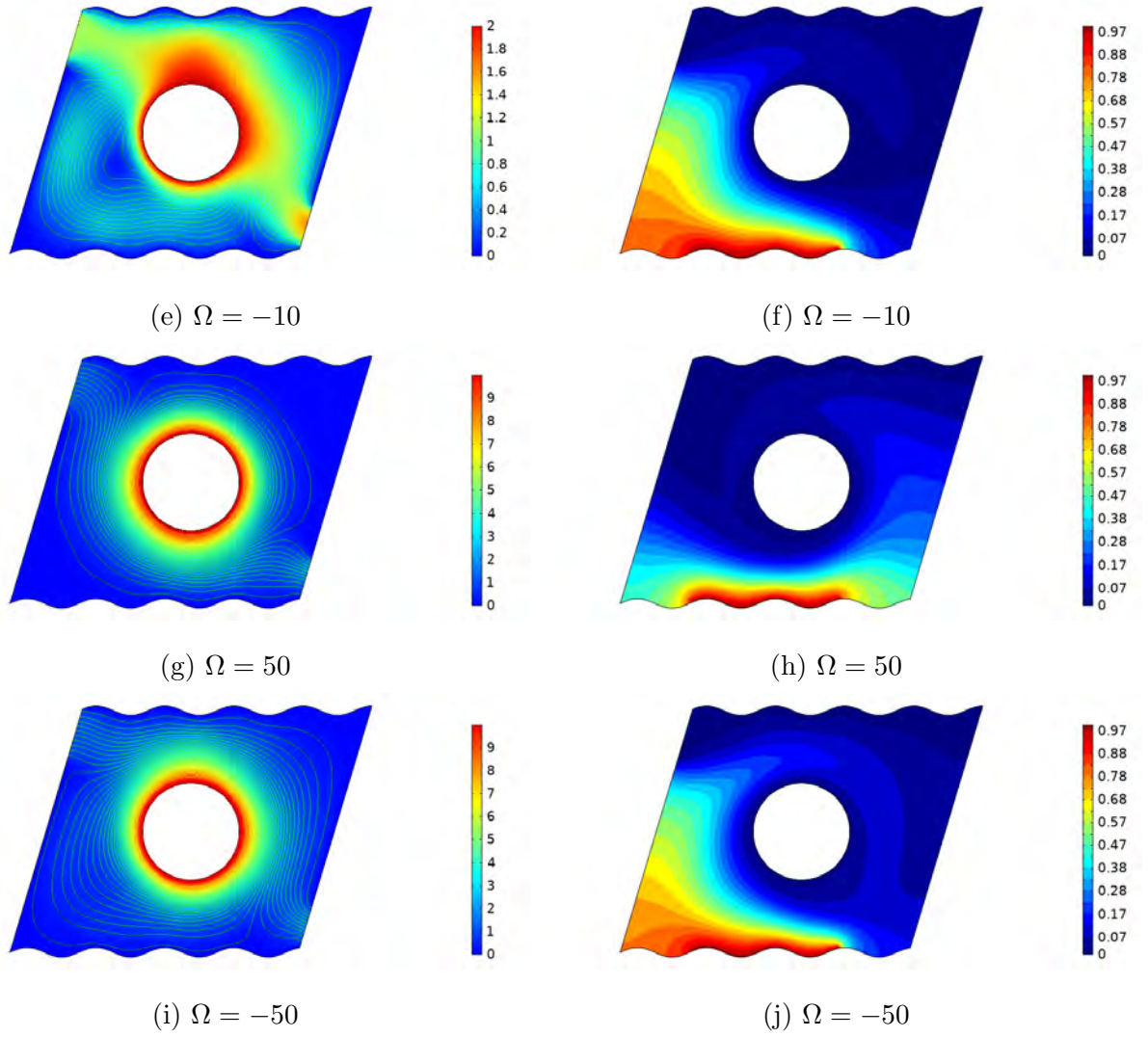


Figure 7.9: Streamlines (left) and isotherms (right) at different rotation speeds and directions  $\Omega$ .

## 7.4 Concluding remarks

This study has scrutinized a numerical simulation of forced convection in porous vented parallelogram enclosure containing nanofluid with partially heated lower wall. The simulations have analyzed the impact of Darcy number, Richardson number, nanoparticles volume fraction and magnitude and direction of rotating cylinder on flow configuration. Escalation of Richardson number, leads to the development of additional anticlockwise circulation due to the enhancement of buoyancy force and isotherms move farther from heated source and dispersed in the wider portion of the cavity. Rise in Darcy number upsurges the permeability of porous media by weakening the resistance. Consequently strength of flow circulation intensifies and isotherms reveal that convection mode of heat transfer become prevailing as compare to conduction. Increasing the volume fraction of nanoparticles leads to an intensification in flow circulations and heat transfer. Circulations get stronger at the enhanced values of rotating magnitude. Heat transportation is maximum when cylinder is rotating in clockwise direction as compared to anticlockwise direction.

# Bibliography

- [1] S. Ostrach. Completely confined natural convection. In *Developments in Mechanics, Proc. Tenth Midwestern Mechanics Conf*, volume 4, pages 53–81. Johnson, Fort Collins, CO, 1968.
- [2] S. Ostrach. Natural convection in enclosure. *Adv Heat Transf*, 8:161–227, 1972.
- [3] S. Ostrach, R.R. Loka, and A. Kumar. Natural convection in low aspect ratio rectangular enclosures. *Nat Convect Enclos*, 8:426–37, 1980.
- [4] S. Ostrach and R.G. Hantman. Natural convection inside a horizontal cylinder. *Chem Eng Commun*, 9(1-6):213–243, 1981.
- [5] S. Ostrach. Natural convection heat transfer in cavities and cells. In *Heat Transfer, Proc Int Heat Transfer Conf*, pages 365–379. Begel House Inc., 1982.
- [6] S. Ostrach. Natural convection in enclosures. *J Heat Mass Transf*, 110(4B):1175–1190, 1988.
- [7] K.R. Ismail and V.L. Scalon. A finite element free convection model for the side wall heated cavity. *Int J Heat Mass Transf*, 43(8):1373–1389, 2000.
- [8] I. Sezai and A.A. Mohmad. Natural convection from a discrete heat source on the bottom of a horizontal enclosure. *Int J Heat Mass Transf*, 43(13):2257–2266, 2000.

- [9] A. Haghshenas, M. Rafati Nasr, and M.H. Rahimian. Numerical simulation of natural convection in an open-ended square cavity filled with porous medium by lattice boltzmann method. *Int Commun Heat Mass Transf*, 37(10):1513–1519, 2010.
- [10] A. Louaraychi, M. Lamsaadi, M. Naïmi, H. El Harfi, M. Kaddiri, A. Raji, and M. Hasnaoui. Mixed convection heat transfer correlations in shallow rectangular cavities with single and double-lid driven boundaries. *Int J Heat Mass Transf*, 132:394–406, 2019.
- [11] K.M. Gangawane, H.F. Oztop, and M.E. Ali. Mixed convection in a lid-driven cavity containing triangular block with constant heat flux: effect of location of block. *Int J Mech Sci*, 152:492–511, 2019.
- [12] E. Salimipour. A numerical study on the fluid flow and heat transfer from a horizontal circular cylinder under mixed convection. *Int J Heat Mass Transf*, 131:365–374, 2019.
- [13] N. Gupta and A.K. Nayak. Activity of buoyancy convection and entropy generation in a parallelogrammic shaped mixed displacement ventilated system. *Int J Therm Sci*, 137:86–100, 2019.
- [14] N.H. Abu-Hamdeh, H.F. Oztop, and K.A. Alnefaie. A computational study on mixed convection in a porous media filled and partially heated lid-driven cavity with an open side. *Alex Eng J*, 59(3):1735–1750, 2020.
- [15] N. Muhammad, S. Nadeem, and A. Issakhov. Finite volume method for mixed convection flow of Ag–ethylene glycol nanofluid flow in a cavity having thin central heater. *Phys A: Stat Mech Appl*, 537:122738–122738, 2020.

- [16] M.M. Rahman, H.F. Öztop, A. Ahsan, and J. Orfi. Natural convection effects on heat and mass transfer in a curvilinear triangular cavity. *Int J Heat Mass Transf*, 55(21-22):6250–6259, 2012.
- [17] M.N. Hasan, S.C. Saha, and Y.T. Gu. Unsteady natural convection within a differentially heated enclosure of sinusoidal corrugated side walls. *Int J Heat Mass Transf*, 55(21-22):5696–5708, 2012.
- [18] X.B. Chen, P. Yu, Y. Sui, S.H. Winoto, and H.T. Low. Natural convection in a cavity filled with porous layers on the top and bottom walls. *Transp Porous Media*, 78(2):259–276, 2009.
- [19] M.S. Astanina, M.A. Sheremet, and J.C. Umavathi. Unsteady natural convection with temperature-dependent viscosity in a square cavity filled with a porous medium. *Transp Porous Media*, 110(1):113–126, 2015.
- [20] A. Misirlioglu, A. Cihat Baytas, and I. Pop. Free convection in a wavy cavity filled with a porous medium. *Int J Heat Mass Transf*, 48(9):1840–1850, 2005.
- [21] S.U.S. Choi. Enhancing thermal conductivity of fluids with nano-particles. *ASME, FED*, 231:99–105, 1995.
- [22] J. Buongiorno. Convective transport in nanofluids. *J Heat Mass Transf*, 128(3):240–250, 2006.
- [23] A. J. Chamkha and F. Selimefendigil. MHD free convection and entropy generation in a corrugated cavity filled with a porous medium saturated with nanofluids. *Entropy*, 20(11):846, 2018.
- [24] M. Usman, M. Hamid, T. Zubair, R. U. Haq, and W. Wang. Cu-Al<sub>2</sub>O<sub>3</sub>/water hybrid nanofluid through a permeable surface in the presence of nonlinear ra-



- diation and variable thermal conductivity via lsm. *Int J Heat Mass Transf*, 126:1347–1356, 2018.
- [25] R. U. Haq and S. Aman. Water functionalized CuO nanoparticles filled in a partially heated trapezoidal cavity with inner heated obstacle: Fem approach. *Int J Heat Mass Transf*, 128:401–417, 2019.
- [26] Y. Jiang and X. Zhou. Analysis of flow and heat transfer characteristics of nanofluids surface tension driven convection in a rectangular cavity. *Int J Mech Sci*, 153:154–163, 2019.
- [27] T. A. Alkanhal, M. Sheikholeslami, M. Usman, R.U Haq, A. Shafee, A. S. Al-Ahmadi, and I. Tlili. Thermal management of MHD nanofluid within the porous medium enclosed in a wavy shaped cavity with square obstacle in the presence of radiation heat source. *Int J Heat Mass Transf*, 139:87–94, 2019.
- [28] F. Selimefendigil and H.F. Öztop. Magnetohydrodynamics forced convection of nanofluid in multi-layered u-shaped vented cavity with a porous region considering wall corrugation effects. *Int Commun Heat Mass Transf*, 113:104551, 2020.
- [29] T.K. Nguyen, F.A. Soomro, J.A. Ali, R.U. Haq, M. Sheikholeslami, and A. Shafee. Heat transfer of ethylene glycol-Fe<sub>3</sub>O<sub>4</sub> nanofluid enclosed by curved porous cavity including electric field. *Phys A: Stat Mech Appl*, 550:123945, 2020.
- [30] S.K. Pandit and A. Chattopadhyay. Higher order compact computations of transient natural convection in a deep cavity with porous medium. *Int J Heat Mass Transf*, 75:624–636, 2014.
- [31] S. Mondal and P. Sibanda. Effects of buoyancy ratio on unsteady double-diffusive natural convection in a cavity filled with porous medium with non-uniform boundary conditions. *Int J Heat Mass Transf*, 85:401–413, 2015.

- [32] M.A. Sheremet, H.F. Oztop, I. Pop, and K. Al-Salem. MHD free convection in a wavy open porous tall cavity filled with nanofluids under an effect of corner heater. *Int J Heat Mass Transf*, 103:955–964, 2016.
- [33] S. Hussain, K. Mehmood, M. Sagheer, and A. Farooq. Entropy generation analysis of mixed convective flow in an inclined channel with cavity with Al<sub>2</sub>O<sub>3</sub>-water nanofluid in porous medium. *Int Commun Heat Mass Transf*, 89:198–210, 2017.
- [34] X.B. Chen, P. Yu, S.H. Winoto, and H.T. Low. Free convection in a porous wavy cavity based on the Darcy-Brinkman-Forchheimer extended model. *Numer Heat Transf A*, 52(4):377–397, 2007.
- [35] G.C. Bourantas, E.D. Skouras, V.C. Loukopoulos, and V.N. Burganos. Heat transfer and natural convection of nanofluids in porous media. *Eur J Mech B Fluids*, 43:45–56, 2014.
- [36] P. Sompong and S. Witayangkurn. Numerical study of natural convection in a heated enclosure with two wavy vertical walls using finite element method. *J Appl Math*, 2014:545–553, 2014.
- [37] H.T. Cheong, S. Sivasankaran, and Z. Siri. Effect of wall inclination on natural convection in a porous trapezoidal cavity. In *AIP Conf Proc*, volume 1605, pages 343–348. American Institute of Physics, 2014.
- [38] A. Mahmoudi, I. Mejri, M.A. Abbassi, and A. Omri. Lattice boltzmann simulation of MHD natural convection in a nanofluid-filled cavity with linear temperature distribution. *Powder Technol*, 256:257–271, 2014.
- [39] I.V. Miroshnichenko, M.A. Sheremet, H.F. Oztop, and K. Al-Salem. MHD natural convection in a partially open trapezoidal cavity filled with a nanofluid. *Int J Mech Sci*, 119:294–302, 2016.

- [40] S. Parvin and A. Akter. Effect of magnetic field on natural convection flow in a prism shaped cavity filled with nanofluid. *Procedia Eng*, 194:421–427, 2017.
- [41] A. Sahi, D. Sadaoui, N. Sadoun, and A. Djerrada. Effects of magnetic field on natural convection heat transfer in a t-shaped cavity. *Mech Ind*, 18(4):407, 2017.
- [42] R.U. Haq, F.A. Soomro, T. Mekkaoui, and Q.M. Al-Mdallal. MHD natural convection flow enclosure in a corrugated cavity filled with a porous medium. *Int J Heat Mass Transf*, 121:1168–1178, 2018.
- [43] A.C. Eringen. Simple microfluids. *Int J Eng Sci*, 2(2):205–217, 1964.
- [44] A.C. Eringen. Theory of micropolar fluids. *J math mech*, pages 1–18, 1966.
- [45] A.C. Eringen. Theory of thermomicrofluids. *J Math Anal Appl*, 38(2):480–496, 1972.
- [46] T. Ariman, M.A. Turk, and N.D. Sylvester. Microcontinuum fluid mechanics—a review. *Int J Eng Sci*, 11(8):905–930, 1973.
- [47] T. Ariman, M.A. Turk, and N.D. Sylvester. Applications of microcontinuum fluid mechanics. *Int J Eng Sci*, 12(4):273–293, 1974.
- [48] G. Lukaszewicz. *Micropolar fluids: theory and applications*. Springer Science & Business Media, 1999.
- [49] A.C. Eringen. *Microcontinuum field theories: II. Fluent media*, volume 2. Springer Science & Business Media, 2001.
- [50] M. Saleem, S. Asghar, and M.A. Hossain. Natural convection flow of micropolar fluid in a rectangular cavity heated from below with cold sidewalls. *Math comput model*, 54(1-2):508–518, 2011.

- [51] M.A. Sheremet, I. Pop, and A. Ishak. Time-dependent natural convection of micropolar fluid in a wavy triangular cavity. *Int J Heat Mass Transf*, 105:610–622, 2017.
- [52] M. Nazeer, N. Ali, and T. Javed. Effects of moving wall on the flow of micropolar fluid inside a right angle triangular cavity. *Int J Numer Methods Fluids*, 28(10):2404–2422, 2018.
- [53] A. Abidi, Z. Raizah, and J. Madiouli. Magnetic field effect on the double diffusive natural convection in three-dimensional cavity filled with micropolar nanofluid. *Appl Sci*, 8(12):2342, 2018.
- [54] L. Samaei, H.M. Deylami, N. Amanifard, and H. Moayedi. Numerical evaluation of using micropolar fluid model for EHD-induced natural convection heat transfer through a rectangular enclosure. *J Electrostat*, 101:103372, 2019.
- [55] S.R. Yan, M. Izadi, M.A. Sheremet, I. Pop, H. F Oztop, and M. Afrand. Inclined lorentz force impact on convective-radiative heat exchange of micropolar nanofluid inside a porous enclosure with tilted elliptical heater. *Int Commun Heat Mass Transf*, 117:104762, 2020.
- [56] J.C. Maxwell. *A treatise on electricity and magnetism*, volume 1. Clarendon press, 1873.
- [57] J. Koo and C. Kleinstreuer. A new thermal conductivity model for nanofluids. *J Nanopart Res*, 6:577–588, 2004.
- [58] J. Li. *Computational analysis of nanofluid flow in microchannels with applications to micro-heat sinks and bio-MEMS*. PhD dissertation, North Carolina State University, 2008.

- [59] J. Koo and C. Kleinstreuer. Laminar nanofluid flow in microheat-sinks. *Int J Heat Mass Transf*, 48(13):2652–2661, 2005.
- [60] H.C. Brinkman. The viscosity of concentrated suspensions and solutions. *J Chem Phys*, 20(4):571–571, 1952.
- [61] L.P. Zhou, B.X. Wang, X.F. Peng, X.Z. Du, and Y.P. Yang. On the specific heat capacity of CuO nanofluid. *Adv Mech Eng*, 2:172085, 2010.
- [62] B.C. Pak and Y.I. Cho. Hydrodynamic and heat transfer study of dispersed fluids with submicron metallic oxide particles. *Exp Heat Transf*, 11(2):151–170, 1998.
- [63] Y. Xuan and W. Roetzel. Conceptions for heat transfer correlation of nanofluids. *Int J Heat Mass Transf*, 43(19):3701–3707, 2000.
- [64] G.G. Stokes. *On the Effect of the Internal Friction of Fluids on the Motion of Pendulums*, volume 3 of *Cambridge Library Collection - Mathematics*, page 1–10. Cambridge University Press, 2009.
- [65] J.N. Reddy. On penalty function methods in the finite-element analysis of flow problems. *Int J Numer Methods Fluids*, 2(2):151–171, 1982.
- [66] B.R. Dyne and J.C. Heinrich. Physically correct penalty-like formulations for accurate pressure calculation in finite element algorithms of the navier-stokes equations. *Int J Numer Methods Eng*, 36(22):3883–3902, 1993.
- [67] J.C. Heinrich and C.A. Vionnet. The penalty method for the navier-stokes equations. *Arch Comput Methods Eng*, 2(2):51–65, 1995.
- [68] B Calcagni, F Marsili, and M Paroncini. Natural convective heat transfer in square enclosures heated from below. *Appl Therm Eng*, 25(16):2522–2531, 2005.

- [69] S.M. Aminossadati and B. Ghasemi. Natural convection of water-CuO nanofluid in a cavity with two pairs of heat source-sink. *Int Commun Heat Mass Transf*, 38(5):672–678, 2011.
- [70] P.S. Reddy and P. Sreedevi. Buongiorno’s model nanofluid natural convection inside a square cavity with thermal radiation. *Chin J Phys*, 72:327–344, 2021.
- [71] M. Shahi, A.H. Mahmoudi, and F. Talebi. Numerical study of mixed convective cooling in a square cavity ventilated and partially heated from the below utilizing nanofluid. *Int Commun Heat Mass Transf*, 37(2):201–213, 2010.
- [72] M.M. Rahman, M.A. Alim, M.A.H. Mamun, M.K. Chowdhury, and A.K.M.S. Islam. Numerical study of opposing mixed convection in a vented enclosure. *ARPJ Eng Appl Sci*, 2(2):25–36, 2007.
- [73] S. Ahmad, A.M. Rohni, and I. Pop. Blasius and sakiadis problems in nanofluids. *Acta Mech*, 218(3-4):195–204, 2011.
- [74] M. H. Esfe, A. A. A. Arani, W. M. Yan, H. Ehteram, A. Aghaie, and M. Afrand. Natural convection in a trapezoidal enclosure filled with carbon nanotube–EG–water nanofluid. *Int J Heat Mass Transf*, 92:76–82, 2016.
- [75] R.U. Haq, F.A. Soomro, H.F. Öztop, and T. Mekkaoui. Thermal management of water-based carbon nanotubes enclosed in a partially heated triangular cavity with heated cylindrical obstacle. *Int J Heat Mass Transf*, 131:724–736, 2019.
- [76] Y.S. Shi, D. Liu, Y. Wang, F.Y. Zhao, and Y.X. Li. Forced flow structure and mixed convection in a ventilated porous enclosure with a local contaminant source. *Int J Heat Mass Transf*, 131:973–983, 2019.

- [77] H.A. Dhahad, G.F. Al-Sumaily, W.H. Alawee, and M.C. Thompson. Aiding and opposing re-circulating mixed convection flows in a square vented enclosure. *Therm Sci Eng Prog*, page 100577, 2020.
- [78] O. Aydin and I. Pop. Natural convection from a discrete heater in enclosures filled with a micropolar fluid. *Int J Eng. Sci*, 43(19-20):1409–1418, 2005.
- [79] R. Roslan, H. Saleh, and I. Hashim. Natural convection in a differentially heated square enclosure with a solid polygon. *Sci World J*, 2014:617492, 2014.
- [80] A. Baïri, E. Zarco-Pernia, and J.M. García de María. A review on natural convection in enclosures for engineering applications. the particular case of the parallelogrammic diode cavity. *Appl Therm Eng*, 63(1):304–322, 2014.
- [81] M.A. Cotter and M.E. Charles. Transient cooling of petroleum by natural convection in cylindrical storage tanks—i. development and testing of a numerical simulator. *Int J Heat Mass Transf*, 36(8):2165–2174, 1993.
- [82] H. Abdillah, G. Saputra, and S. Permana. Study of natural convection passive cooling system for nuclear reactors. In *J Phys Conf Ser*, volume 877, page 012047. IOP Publishing, 2017.
- [83] E. Yu and Y.K. Joshi. Natural convection air cooling of electronic components in partially open compact horizontal enclosures. *IEEE Trans Compon Packag Manuf Technol*, 23(1):14–22, 2000.
- [84] S.H. Tirmizi and W.N. Gill. Effect of natural convection on growth velocity and morphology of dendritic ice crystals. *J Cryst Growth*, 85(3):488–502, 1987.
- [85] C. Muresan, C. Ménézo, R. Bennacer, and R. Vaillon. Numerical simulation of a vertical solar collector integrated in a building frame: radiation and turbulent natural convection coupling. *Heat Transf Eng*, 27(2):29–42, 2006.

- [86] B. Bena and R.J. Fuller. Natural convection solar dryer with biomass back-up heater. *Sol Energy*, 72(1):75–83, 2002.
- [87] A.A. Ghani, M.M. Farid, X.D. Chen, and P. Richards. Numerical simulation of natural convection heating of canned food by computational fluid dynamics. *J Food Eng*, 41(1):55–64, 1999.
- [88] M.H. Esfe, A.A.A. Arani, W. Yan, H. Ehteram, A. Aghaie, and M. Afrand. Natural convection in a trapezoidal enclosure filled with carbon nanotube–EG–water nanofluid. *Int J Heat Mass Transf*, 92:76–82, 2016.
- [89] R.U. Haq, F.A. Soomro, and Z. Hammouch. Heat transfer analysis of CuO-water enclosed in a partially heated rhombus with heated square obstacle. *Int J Heat Mass Transf*, 118:773–784, 2018.



Turnitin Originality Report

Flows of Nanofluids inside Cavities: Finite Element Method

by Naeem Ullah .



From CL QAU (DRSML)

- Processed on 15-Jun-2022 12:09 PKT
- ID: 1857185026
- Word Count: 22401

*Naeem*

Similarity Index

14%

Similarity by Source

Internet Sources:

7%

Publications:

11%

Student Papers:

3%

*Soradem*  
*15/06/2022*

PROFESSOR  
Department of Mathematics  
Quaid-i-Azam University  
Islamabad

*Soradem*  
Focal Person (Turnitin)  
Quaid-i-Azam University  
Islamabad

**sources:**

1 1% match (Internet from 14-Feb-2022)  
<https://www.emerald.com/insight/content/doi/10.1108/HFF-08-2020-0504/full/html>

2 1% match (Internet from 13-Apr-2022)  
<https://iopscience.iop.org/article/10.1088/1402-4896/abfba7>

3 < 1% match (student papers from 11-Dec-2021)  
[Submitted to Universiti Kebangsaan Malaysia on 2021-12-11](#)

4 < 1% match (student papers from 05-Dec-2021)  
[Submitted to Universiti Kebangsaan Malaysia on 2021-12-05](#)

5 < 1% match (student papers from 27-Nov-2013)  
[Submitted to Universiti Kebangsaan Malaysia on 2013-11-27](#)

6 < 1% match (student papers from 07-Aug-2018)  
[Submitted to Higher Education Commission Pakistan on 2018-08-07](#)

7 < 1% match (student papers from 05-Feb-2021)  
[Submitted to Higher Education Commission Pakistan on 2021-02-05](#)

8 < 1% match (student papers from 25-Jul-2017)  
[Submitted to Higher Education Commission Pakistan on 2017-07-25](#)

< 1% match (student papers from 02-Jan-2015)